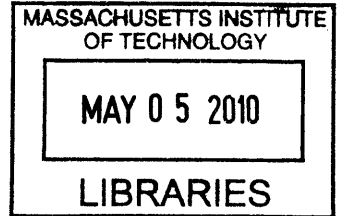# Origami-Inspired Nanofabrication Utilizing Physical and Magnetic Properties of In Situ Grown Carbon Nanotubes

by

Hyun Jin In

B.S., University of California, Berkeley (1999)
S.M., Massachusetts Institute of Technology (2005)

Submitted to the Department of Mechanical Engineering
in partial fulfillment of the requirements for the degree of

Doctor of Philosophy in Mechanical Engineering

at the

MASSACHUSETTS INSTITUTE OF TECHNOLOGY

February 2010

The author hereby grants to Massachusetts Institute of Technology
permission to reproduce and
to distribute copies of this thesis document in whole or in part.

Signature of Author ....
Department of Mechanical Engineering
January 8, 2010

Certified by ....
George Barbastathis
Associate Professor of Mechanical Engineering
Thesis Supervisor

Accepted by ....
David E. Hardt
Chairman, Department Committee on Graduate Students

Origami-Inspired Nanofabrication Utilizing Physical and Magnetic Properties of In Situ Grown Carbon Nanotubes

by

Hyun Jin In

Submitted to the Department of Mechanical Engineering
on January 8, 2010, in partial fulfillment of the
requirements for the degree of
Doctor of Philosophy in Mechanical Engineering

Abstract

Carbon nanotubes (CNTs), in particular the vertically-aligned variety grown through a plasma enhanced chemical vapor deposition (PECVD)-based process, are highly versatile nanostructures that can be used in a variety of nanomanufacturing applications. However, process and material compatibility issues have prevented the nanotubes from becoming more fully integrated into various micro- and nanomanufacturing applications. In this thesis, the integration of *in situ* CNT growth with a 3-D nanomanufacturing platform, namely the Nanostructured Origami^{TM} process, will be shown. Due to the high temperatures involved in CNT growth, a new origami membrane material, titanium nitride (TiN), is introduced. This new origami membrane serves as an excellent diffusion barrier layer throughout the CNT growth process while promoting consistent nanotube growth and maintaining electrical conductivity to the CNTs. Various further modifications are made to the origami process, for example in metallization techniques, to accommodate the addition of CNTs to origami devices. Based on the presented CNT-origami process, a functioning microscale supercapacitor is also fabricated and tested. The integration of high surface area CNT electrodes with a unique 3-D device geometry results in a fab-friendly, high-performance supercapacitor that can easily be integrated as an onboard power source in self-powered microsystem applications. Finally, the magnetic properties of our *in situ* grown CNTs, derived from their naturally occurring, tip-encapsulated catalyst particles, will be characterized. Furthermore, these properties will be used to magnetically actuate, align, and latch individual as well as large arrays of CNTs and the entire membranes on which they are grown. The magnetic behaviors of CNTs and their underlying membranes will be investigated through computer simulation and experimental verification.

Thesis Supervisor: George Barbastathis
Title: Associate Professor of Mechanical Engineering

Acknowledgments

My time at MIT has been nothing short of extraordinary. It was certainly a long, and at time arduous, journey, but it's one that I wouldn't trade for any other. Both academically and personally, I have grown in ways never before imagined, and I will forever cherish the many lessons learned at MIT. Of course, none of this would have been possible without the help from some incredible people.

First and foremost, I want to express my deepest gratitude to my advisor Professor George Barbastathis. His deep insight on a plethora of topics, not to mention keen observation and mathematical prowess, was critical in shaping and guiding my research. He has not only shown me how to become a great researcher but also how to have fun in the process. I would also like to extend my deep thanks and appreciation to the members of my thesis committee – Professors Sang-Gook Kim, Caroline Ross, and Yang Shao-Horn – whose expertise and guidance have been truly invaluable.

I also want to thank my friends and colleagues in the ever-growing 3D Optical Systems Group. They are the most intelligent and friendly bunch that I have ever encountered. As of January 2010, my thanks go out to Adi, Chih-Hao, Hanhong, Jason, Johnny, Justin, Laura, Lei, Martin, Nader, Nick, Pepe, Satoshi, Se Baek, Se Young, Tony, and Yuan (plus everyone in Singapore!). I am also deeply indebted to my friends and colleagues at KGSAME and Mokyang Church.

I must also acknowledge the incredible help I received from the staff at MIT's Microsystems Technology Laboratories (MTL). I want to especially thank Bob Bicchieri and Kurt Broderick for kindly and repeatedly lending me heaps of their expertise and assistance.

Finally, I want to thank my amazing family - my parents, brother, grandparents, aunt, and parents-in-law - for their love, support, and prayers. And of course, words cannot begin to express my love and gratitude for my wife, Hye Yeon, who is undeniably the most beautiful and remarkable woman I have ever set my eyes upon. Soli Deo Gloria!

Contents

8

List of Figures

10

List of Tables

Chapter 1

Introduction

In recent years, tremendous advancements have been made in the area of micro- and nanoscale fabrication technology. Not surprisingly, much of these efforts have been undertaken at a feverish pace thanks largely in part to the semiconductor industry and Dr. Moore's enduring law [1]. Intel's latest product offering, for example, crams over 1.9 trillion transistors onto a single chip using their 32 nm complementary metal-oxide-semiconductor (CMOS) technology [2].

In addition to the semiconductor industry, an army of nanotechnology visionaries, scientists, and engineers have created an impressive portfolio of "bottom-up" and "top-down" techniques for fabricating virtually anything at the nanoscale with atomic precision. The innumerable types of currently available nanostructures and nanofabrication methods, ranging anywhere from atomic force microscope nanolithography [3] to zinc oxide nanowire arrays [4], have subsequently enabled the creation of groundbreaking applications in the fields of biomedicine, chemical/biological sensing, computation, energy, and optoelectronics, just to name a few.

One major drawback of current nanofabrication techniques, however, is that they are still largely constrained to planar, or two-dimensional (2-D), geometries. While planar fabrication is sufficient for most applications and enables highly reliable and low cost production by leveraging tools and techniques perfected by the semiconductor industry, there is a growing number of application areas that require or can benefit immensely from a three-dimensional (3-D) device architecture. Ultra high density memory devices [5], 3-D integrated circuits (ICs) [6], 3-D photonic crystals [7], 3-D scaffolds for tissue

engineering [8], and 3-D energy storage devices [9] are just a few of the many growing application areas that utilize micro- and nanostructured features within an overall 3-D device architecture. While reasons for employing a 3-D geometry are varied, two of the most common reasons reported in literature are: (1) small areal footprint and (2) short transport lengths (for electrons, ions, photons, etc.).

1.1   3-D Nanomanufacturing

As the name suggests, "3-D nanomanufacturing" refers to a set of production-capable tools and techniques for fabricating and assembling nanoscale components in a 3-D configuration. Previously in my master's thesis [10], various types of 3-D nanofabrication techniques, for both "bottom-up" and "top-down" schemes, were described in detail. While many of the delineated techniques were quite innovative and successful in creating unique, truly 3-D nanostructures, the concept of 3-D nanomanufacturing further carries with it the possibility of massively parallel and reliable batch fabrication at production levels, a point missing from most current 3-D nanofabrication approaches. While production level manufacturability is not a requirement in typical research settings, the inherently exorbitant costs associated with micro- and nanoscale fabrication necessitate it from a practical standpoint if widespread application of the particular innovation is ever intended.

To satisfy this growing niche of 3-D nanomanufacturing, the Nanostructured Origami™ process, shown in Figure 1-1, was proposed and demonstrated [11–13]. The origami process, inspired by the traditional art of paper folding, is a two-step fabrication approach that combines well-established microfabrication tools with state-of-the-art nanofabrication techniques in creating 3-D devices with nanostructured surfaces.

In the first step of the process, existing planar fabrication tools and techniques are utilized to create micro- and nanopatterned 2-D membranes. The membrane can be thought of as the analog of "paper" used in conventional origami and, in addition to being patterned directly, can provide a base on which to grow or deposit nanostructured materials such as nanotube and nanowires. Thus far, our group has demonstrated the integration of various nanoscale structures such as: (1) sub-micrometer gratings and

magnets patterned through e-beam lithography [12, 14]; (2) high surface area amorphous carbon deposited through micromanipulators [13]; and (3) carbon nanotubes grown *in situ* on the membrane, as will be discussed in further detail in Chapter 2. During this stage, the membrane is also patterned with features that will allow it to fold, such as creases, hinges, and various actuation mechanisms. Selecting the right material for the membrane is extremely important and must take into consideration a huge assortment of parameters such as stiffness, electrical conductivity, residual stress, etch resistance, material and processing compatibility, coefficient of thermal expansion, melting temperature, and chemical stability, among others. Thus far, origami devices have been made using membranes made of silicon [15], silicon nitride [12, 14], and SU-8 [11, 13, 16], a type of robust and chemically resistant photo-imageable epoxy used regularly in MEMS-type applications. Recent work involving the use of titanium nitride (TiN) membranes [17] will be discussed in detail in the following chapter.
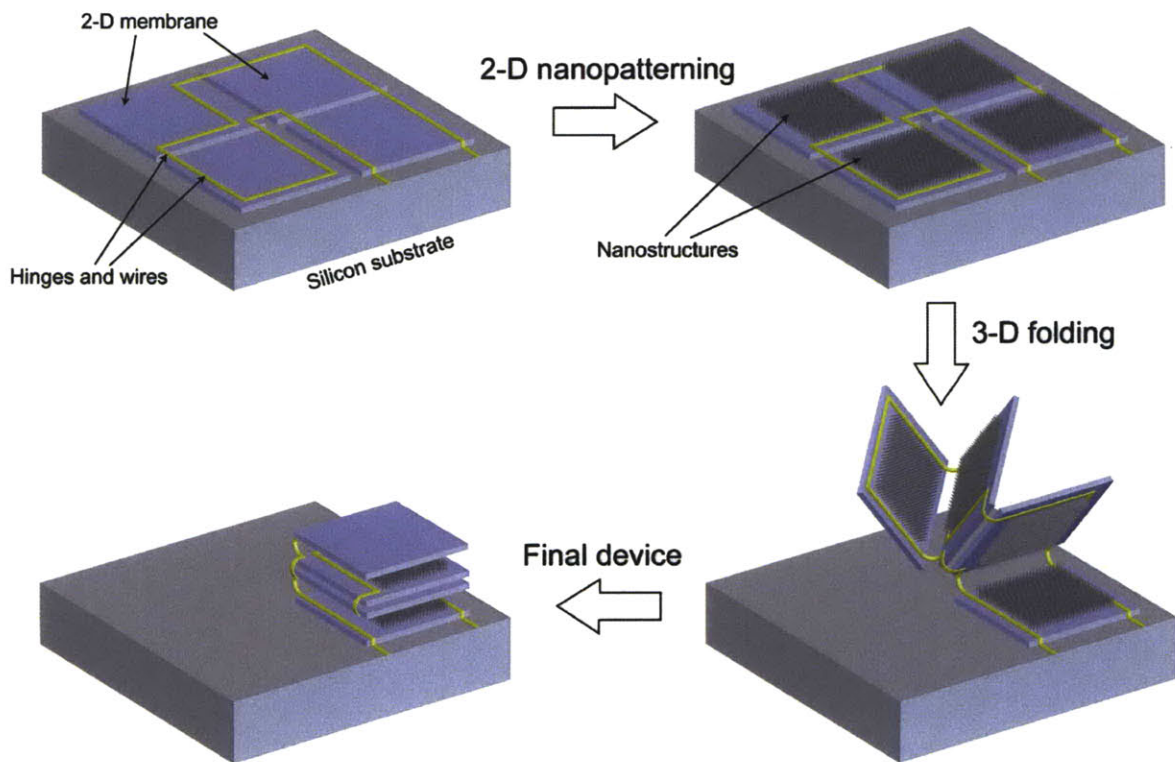
Figure 1-1: Schematic overview of the Nanostructured Origami™ process.

The second step of the origami process consists of automatically folding the patterned membranes into the desired 3-D configuration. Such autonomous, parallel folding of the patterned membranes, an important feature of the origami process that enables batch fabrication, has been accomplished previously through the use of Lorentz force [10, 15, 16], residual stress [12], ion implantation [18], and magnetic torque arising from slender nanomagnets patterned through electron-beam (e-beam) lithography [14]. Additionally, actuation through the use of ferromagnetic materials embedded inside carbon nanotubes [19] will be discussed in Chapter 4.

1.2   Carbon nanotubes

Carbon nanotubes (CNTs), the rolled up sheets of graphene first discovered by Iijima in 1991 [20], have been the at the center of an intense global research effort focused on understanding their properties, growth mechanisms, and possible applications. Without question, CNTs, with their highly unique electronic, mechanical, optical, and chemical properties, have been one of the most actively studied materials in recent history, and tremendous advancements have indeed been made particularly in the area of efficient, high-yield growth methods. Even after almost twenty years since their discovery, there is yet no end in sight for CNT-related research. However, there is still, after nearly twenty years, much controversy surrounding its exact growth mechanism, and the transition towards commercial applications has been extremely limited thus far.

1.2.1   Growth theory and techniques

As mentioned previously, exact carbon nanotube growth mechanisms are still subject to much speculation. For example, the precise role of catalysts necessary for CNT growth remains highly controversial [21]. Nevertheless, researchers have become highly skilled at growing and purifying both single-walled [22] and multi-walled carbon nanotubes [23].

Currently used approaches for growing single-walled CNTs (SWCNTs) and multi-walled CNTs (MWCNTs) can be largely categorized into arc-discharge, laser ablation, and chemical vapor deposition (CVD) methods. Both arc-discharge and laser ablation methods, explained in much greater detail in [21, 24, 25], involve the evaporation and

condensation of solid carbon sources at extremely high temperatures approaching the melting temperature of graphite (3000 ~ 4000°C). For the arc-discharge method, the carbon atoms are evaporated through the ignition of a plasma between opposing carbon anode and cathode, whereas in the laser ablation method, an intense laser pulse is used to vaporize a carbon target. In both case, the resulting CNTs must be carefully collected and purified. The arc-discharge method, while it has lower yield than the laser-ablation method, is used most often in industrial applications to create high-quality, defect-free CNTs because the laser ablation technique is not amenable to being scaled up to production volumes [23].

Nanotube growth based on CVD has been used most often in recent years because it allows for the direct growth of CNTs on patterned surfaces [26] thereby eliminating the arduous task of collecting and purifying the nanotubes. Although the precise CNT growth mechanism and kinetics is still under intense investigation [27-29], the general growth process is as follows: (1) a hydrocarbon, such as acetylene, is adsorbed onto the surface of a catalytic particle; (2) carbon is released upon decomposition of the gas and dissolves and diffuses into the catalyst; and (3) the carbon precipitates out of the catalytic particle in tubular, crystalline form upon supersaturation of the catalyst. As the carbon network grows out of the catalytic particle, the particle itself can remain anchored to the substrate (base-growth mode) or detach completely from the substrate (tip-growth mode), as seen in Figure 1-2.
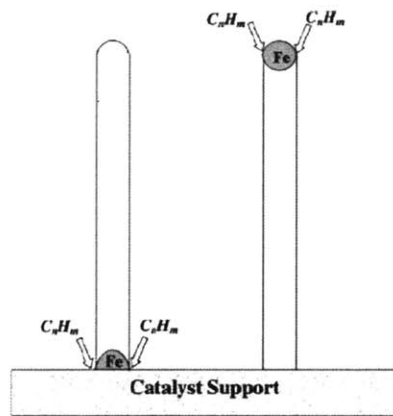
Figure 1-2: Two different growth modes for CNTs during chemical vapor deposition: base growth (left) and tip growth (right) [21].

Most recently, much research has focused on a particular type of CVD-type nanotube growth process based on the use of a DC [30-32], microwave [33], or RF plasma [34]. The CNT growth mechanism and process in such plasma enhanced chemical vapor deposition (PECVD) methods remain similar to those of more traditional CVD methods; however, there are some noteworthy differences between the two methods.

The primary difference between the two methods is that CNTs grown via the PECVD method exhibit extreme vertical alignment and straightness. Such behavior of PECVD-grown CNTs has been demonstrated by dozens of groups and is believed to be a result of the CNTs' preference to align with the applied field or to the electrical self-bias field created by the plasma environment during growth [35], although the precise mechanism of this phenomenon is not known. Vertically aligned CNTs can be grown via the CVD method as well where a physical constraint (e.g. the porous growth template) or the van der Waals interaction between neighboring CNTs can keep the nanotubes relatively straight during growth [33, 36]. However, as seen in Figure 1-3, PECVD-grown CNTs exhibit unparalleled straightness and vertical alignment. In fact, the CNTs align themselves so well to the field created by the plasma environment that the CNTs can be grown into a zigzag morphology by simply altering the field direction during growth [35]. For many nanomanufacturing applications, for example in creating field emission devices, the ability to grow very straight CNTs with controllable orientations can be advantageous.

Another potential benefit of PECVD-grown CNTs is the much lower temperature required for nanotube growth. CVD-based growth methods can require temperatures in excess of 1000°C, whereas growth temperatures as low as 120°C has been reported for PECVD-based methods [38]. It is believed that the lower growth temperature is a result of the plasma ionizing the hydrocarbon gas while locally heating the catalyst surface to promote more efficient adsorption and diffusion of the carbon atoms [38]. However, one caveat of the lower growth temperature appears to be an increase in the number of defects in the CNT structure as well as the increased tendency for the nanotubes to grow in a less crystalline carbon nanofiber (CNF) morphology [38, 39]. In addition, most of the nanotubes grown via the PECVD-based method are MWCNTs, and the reliable growth of SWCNTs has not yet been reported. For many nanomanufacturing applica-

tions where the still highly favorable physical and mechanical properties of less than perfect MWCNTs should be sufficient, the lower growth temperature and the resulting improvements in compatibility with existing materials and devices enabled by PECVD-based CNT growth will be highly desirable.
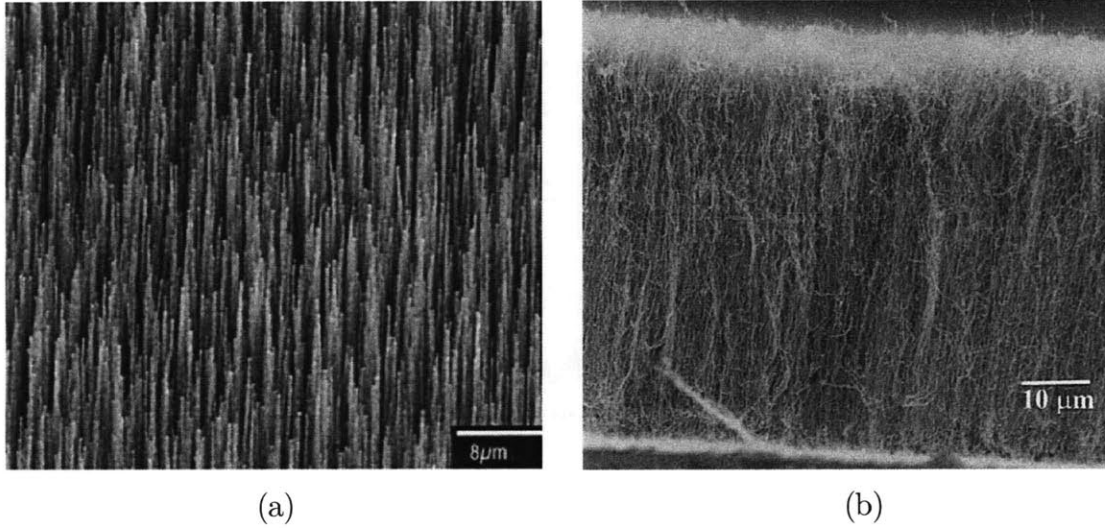
Figure 1-3: Vertically aligned carbon nanotubes grown via (a) PECVD [30] and (b) CVD-based [37] methods.

One last distinction of the PECVD-grown CNTs is that they tend to almost always grow in tip-growth mode shown earlier in Fig 1-2 [30, 32], while CNTs grown through CVD methods grow predominantly in base-growth mode. While the exact reason for this occurrence is unclear, it is indicative of a weak interaction between the catalyst and the substrate [40]. While CNTs grown in base-growth mode exhibit higher yield and purity [40], Chapter 4 will discuss the importance of catalyst particles found at the tips of CNTs grown in tip-growth mode.

1.2.2 Device integration methods

As mentioned before, commercial applications of CNT-enabled devices have significantly lagged behind the great strides made in fundamental CNT-related research. One main reason for this deficiency lies in the inherent difficulty of efficiently and precisely inte-

grating a massive quantity of nanotubes with other micro-meso-macro-scale structures and devices. For many applications, the location (for one or both ends of the tube), orientation (in three dimensions), and shape (e.g. size or curvature) of the CNTs must be precisely controlled during the integration process. Perhaps most importantly, in order to satisfy the tenets of nanomanufacturing and remain viable for production, all this must be accomplished in a time-saving, cost-effective, and massively parallel fashion.

Currently proposed and used methods for CNT integration can be largely divided into three categories: (1) solution-based; (2) pick-and-place; and (3) direct growth. Most of these methods are applicable not only to CNTs but other types of nanowire and nanofibers as well. In solution-based methods, CNTs are typically dispersed in solvent, such as ethanol, and passed over the desired areas of CNT integration. As the solution dries, the CNTs are directed towards designated areas on the device and aligned due to fluidic forces [41], magnetic forces [42, 43], or dielectrophoretic forces [44, 45], among others. Generally, such methods are limited to in-plane alignment of the nanotubes, and further steps, such as metal evaporation and lithography, must be taken to address the inherently high contact resistance between the CNTs and their corresponding contacts [45]. However, the parallel nature of this integration method lends itself well to high-volume production.

Pick-and-place methods involve the use of micro- and nanoscale probes and manipulators in literally picking up individual nanotubes from one substrate and placing them at the desired locations on another [46, 47]. While such methods are highly reliable and accurate, they are exceedingly slow and inefficient. Furthermore, actions must be taken to permanently affix the displaced nanotubes while reducing contact resistance. Accordingly, the pick-and-place method is ideal for research settings where only a handful of CNTs need to be integrated.

Direct growth methods for CNT integration involve the use of existing micro- and nanofabrication tools to directly pattern the catalyst sites prior to either CVD or PECVD-based CNT growth. This method is well-suited for nanomanufacturing applications since precise, wafer-scale positioning and growth of large quantities of CNTs can be integrated with the rest of the device fabrication process. As seen in Figure 1-4, single strands of CNTs can be controllably grown on the device by using e-beam

22

lithography to pattern the catalysts [48, 49], while larger CNT forests can be grown at desired locations by using standard optical lithography [50] to pattern larger catalyst patches. In both cases, CNT length, orientation, and quality can be controlled through the growth parameters. For the e-beam lithography approach, the precise location and diameter of each nanotube can further be defined. The e-beam approach, however, requires each growth site to be individually patterned making it unsuitable for applications involving large arrays of CNTs.
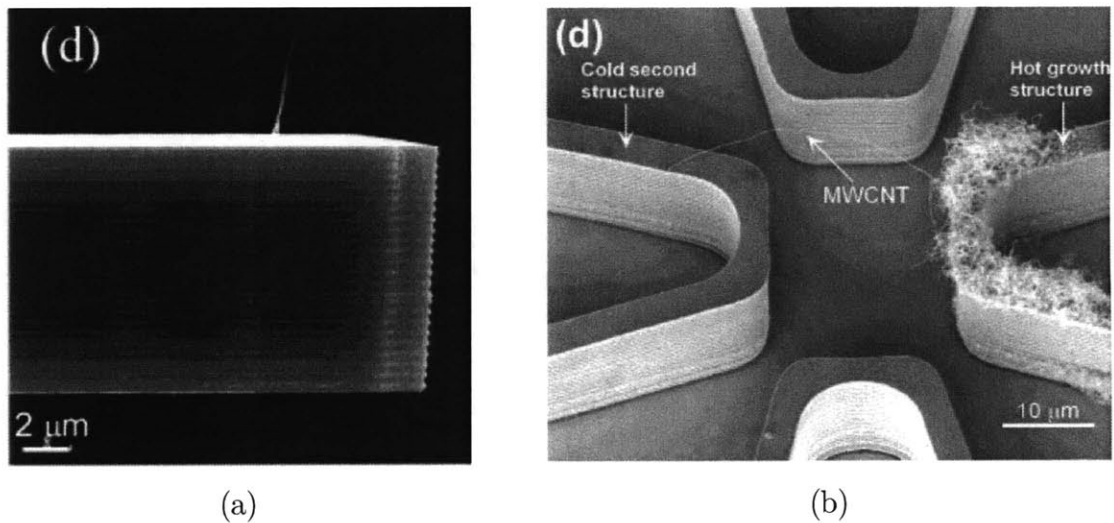
Figure 1-4: Examples of (a) single [48] and (b) multiple strands [50] of CNTs grown directly on functioning microstructures.

Lastly, a transplanting-based assembly method [51, 52], outlined in Figure 1-5, is another interesting CNT integration technique that possess elements of all three types of methods mentioned above. In this approach, single strands [51] or bundles [52] of CNTs are partially encapsulated in micropatterend polymer carrier blocks and transplanted to their final locations using pick-and-place or self-assembly-based methods. Similar to the transplanting assembly method for CNT integration, future nanomanufacturing processes must possess speed, precision, and batch fabrication capabilities.
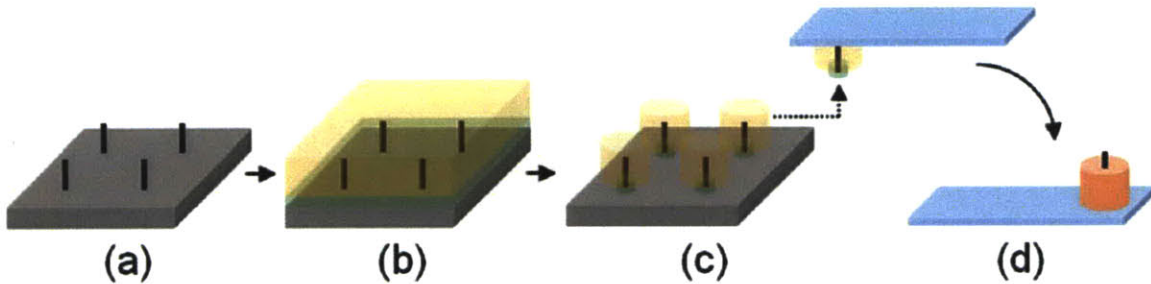
Figure 1-5: Overview of the transplanting assembly method for creating CNT-tipped AFM probes [51].

1.3 Outline of thesis

The general objective of this thesis is to demonstrate the feasibility as well as the advantages of a fabrication technique that combines origami-based 3-D fabrication methods with existing CNT growth techniques. Most importantly, all this will be accomplished while adhering to tenets of the Nanostructured Origami™ process, namely the use of non-exotic fabrication equipment and techniques in a manner compatible with massively-parallel batch fabrication schemes.

In keeping with the theme of nanomanufacturing, this thesis will exclusively deal with PECVD-grown, vertically-aligned CNTs. As mentioned, the PECVD-grown CNTs can be grown at relatively low temperatures, and their density, geometry, shape, and precise locations can be pre-defined through various lithographic techniques. Such features of PECVD-grown CNTs will facilitate efficient integration with the origami process while maximizing potential nanomanufacturing applications. While CNTs possess many highly unique and interesting characteristics that can be taken advantage of by origami devices, their physical and magnetic properties will primarily be explored and utilized.

Chapter 2 will be devoted to the various fabrication challenges that can arise in the process of integrating high-temperature CNT growth with origami-based devices. Specifically, a new CNT-compatible origami membrane material will be introduced and integrated into the overall origami fabrication scheme. Additionally, a new type of

metallization method, designed to accommodate vertically-aligned CNTs, will be demonstrated. Various fabrication tips and tricks involved in the integration of *in situ* grown CNTs will further be discussed.

Chapter 3 will discuss the fabrication and electrochemical testing of an origami-based, 3-D supercapacitor with CNT-based electrodes. The CNT electrodes are grown directly on the origami supercapacitor based on techniques mentioned in Chapter 2. Additional fabrication complications arising from this particular application of the CNT-origami process will be mentioned, and the various advantages of creating this particular type of supercapacitor will be discussed.

Chapter 4 will introduce a new origami membrane manipulation scheme involving the use of magnetic catalyst particles naturally encapsulated inside the tip regions of PECVD-grown CNTs. The magnetic behaviors of these tips, and consequently the entire nanotube and supporting membrane, will be investigated through theory, simulation, and experiment. Magnetic rotation of CNT-covered membranes will be explored in depth while initial results involving magnetic CNT latching will also be shown.

Chapter 5 will summarize the various new findings and contributions of this thesis as well as suggest related future works that will further expand upon the scope of this research.

Chapter 2

Origami fabrication of carbon nanotube devices

As mentioned previously in Chapter 1, the Nanostructured Origami™ process is a 3-D nanomanufacturing approach based on the concept of membrane folding. The origami process itself is quite versatile and can readily be applied to a wide variety of processes and materials with minimal variation while accommodating many different types of state-of-the-art nanostructures. The integration of carbon nanotubes, however, requires some noteworthy changes to the original origami method due mainly to the high processing temperatures associated with growing CNTs. In this chapter, particular challenges and process modifications associated with the origami integration of CNTs will be discussed.

2.1   Origami membrane

The membrane, or the "paper," of the origami process is a highly critical element that serves several vital functions. One of its main functions is to serve as a releasable and foldable substrate for the various nanostructures. For the case of integration with *in situ* grown CNTs, the membrane must serve as a reliable surface on which the nanotubes can grow while withstanding the high temperatures of the CNT growth process.

2.1.1 Membrane selection

Although carbon nanotube growth on silicon or silicon nitride, two of the materials used in the past for origami membranes, is well-documented and has been successfully repeated in our laboratory, the low electrical conductivity of those materials make them unsuitable for many CNT-integrated device applications in which direct electrical connections must be made through the membrane and into the nanotubes. Other origami membrane materials used in the past, such as gold, are very conductive but cannot be used as a base for directly growing CNTs as will be discussed in later sections. Since providing electrical connections to CNTs is critical for many device applications, researchers often overcome this problem by first growing the CNTs on a non-conducting substrate, such as silicon or quartz, and then transferring the entire array to a conducting surface [53] or going through highly complex post-CNT processing steps to individually connect each nanotube via metal lines [54]. These types of approaches, however, are not well-suited for 3-D nanomanufacturing applications and were not considered for integrating CNTs with origami fabrication.

Consequently, a new origami membrane material, suitable for direct growth of CNTs, was needed. The new membrane had to satisfy the following requirements:

(1) It must not be damaged by high temperatures encountered during the PECVD-based CNT growth process (typically >600°C).

(2) It must not impede catalyst nucleation and CNT growth.

(3) It must exhibit sufficient electrical conductivity.

(4) It must withstand XeF_2 etching for the sacrificial release step.

(5) It must be available within MIT's fabrication facilities.

The last requirement, availability within MIT's fabrication facilities, was essential since one of the main premises of the Nanostructured Origami™ process is the exclusive use of widely available and compatible materials and processes. Availability within Microsystems Technology Laboratories (MTL), the main fabrication facility at MIT, would definitely attest to this fact. Candidate materials for the CNT-origami membrane are summarized below in Table 2-1.

28

Table 2-1: Summary of candidate materials for CNT integration with some of the key parameters required for origami fabrication.

Membrane Material	High-Temperature Processing	Documented CNT Growth	Electrically Conductive	Resistant to XeF$_2$ Etch	Available at MIT
Silicon [48]	Yes	Yes	No	No	Yes
Polysilicon [50]	Yes	Yes	No	No	Yes
Silicon Dioxide [54]	Yes	Yes	No	Yes	Yes
Silicon Nitride	Yes	Yes	No	Yes	Yes
Gold [13]	No	No	Yes	Yes	Yes
Inconel [55]	Yes	Yes	Yes	No	No
Tungsten [56]	Yes	Yes	Yes	No	Yes
Molybdenum [57,58]	Yes	Yes	Yes	No	Yes
Titanium Nitride [17,59]	Yes	Yes	Yes	Yes	Yes

Based on Table 2-1, titanium nitride (TiN), used commonly in semiconductor applications as a diffusion barrier layer, seems to be the only suitable material for CNT-origami integration. Therefore, TiN was chosen as the new membrane material, and its several advantages as well as disadvantages will be discussed in the following sections. It should be noted, however, that certain metals that have very high melting points, such as tungsten (W) and molybdenum (Mo), would have also served as excellent membrane materials save for their etching in XeF$_2$ (they also show little etch resistance to most etchants that attack silicon). In future origami devices that employ different release methods or sacrificial layers, metals such as W and Mo, which actually possess higher electrical conductivities compared to TiN, may be considered.

2.1.2   Stress annealing

Applied Materials Endura 5500 deposition tool was used to deposit TiN layers with thicknesses ranging from 100 nm to 2 μm on a <100> silicon substrate. Figure 2-1 shows sample images of a patterned TiN layer that has been partially released from the substrate. As can be seen, TiN layers, as they are deposited in the MTL, inherently possess some residual compressive stress that can cause the released device to warp and

29

crack; for origami membranes, it is imperative that they be stress-free so as to remain flat after release. Typically, thinner TiN layers resulted in greater residual stress, but a very thin 100 nm TiN layer was predominantly used to promote greater flexibility of the origami membranes during subsequent folding. In order to minimize compressive stress, an annealing step, similar to the one outlined in [62], was initially performed by heating the samples under nitrogen flow. The annealing conditions and results are summarized in Table 2-2.
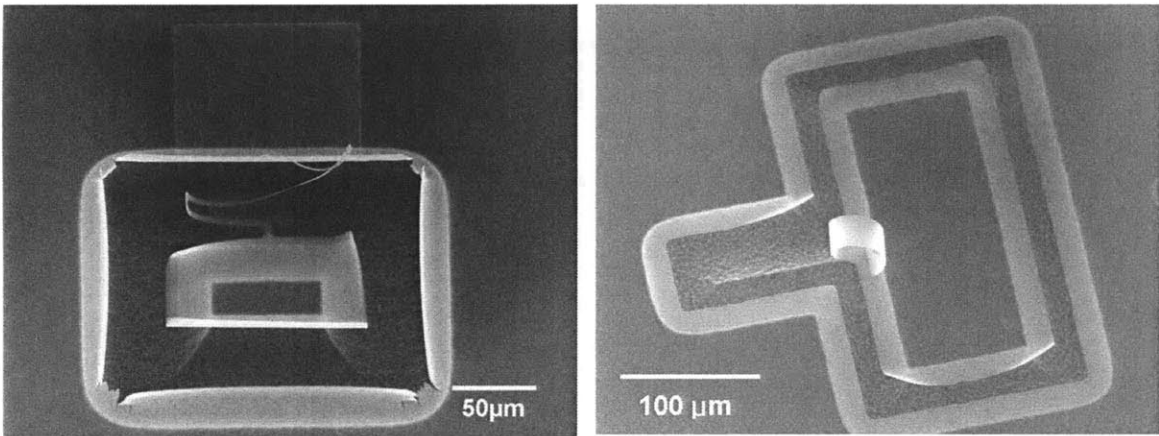
Figure 2-1: Severely warped and distorted devices consisting of an unannealed TiN layer after partial XeF_2 release.

Table 2-2: Compressive stress levels in a 100 nm thick TiN layer before and after annealing.

Stress after TiN Deposition	Stress after 4 hours @ 500°C	Stress after 20 hours @ 500°C	% Reduction in Stress
1168 MPa	469 MPa	n/a	-59.8%
1167 MPa	388 MPa	n/a	-66.8%
793 MPa	n/a	102 MPa	-87.1%
693 MPa	n/a	113 MPa	-83.7%

As shown in Table 2-2, various annealing steps were shown to be highly effective in reducing the residual stress of TiN. As expected, longer annealing times produced greater stress reductions, although further reductions in stress were not observed beyond 20 hours of annealing.

Figure 2-2(a) shows an annealed (thus stress-free) and patterned TiN layer with some gold (Au) and CNT structures above it (whose depositions methods will be discussed in subsequent sections). However, after about 10 minutes of exposure to XeF_2 etching at room temperature, almost all of the TiN layer had disappeared as clearly seen in Figure 2-2(b). This was highly unexpected since TiN used by Seneviratne et al. [62] was deposited using identical equipment at MIT's MTL yet exhibited etch resistance to XeF_2. Additionally, Chan et al. reported that XeF_2 did not etch TiN [63], while Wu et al. later reported that TiN was resistant to XeF_2 etching at temperatures below 100°C [64]. Although room temperature etching of TiN using XeF_2 has not been reported in literature, we hypothesized that the TiN layer had oxidized during the annealing process, which takes place in essentially an open-air chamber, and that oxidized TiN is somehow more susceptible to XeF_2 etching. Significant oxidation of TiN at temperatures above 500°C has been reported previously [65]. It is also possible that titanium silicides, easily formed during temperature treatments of titanium rich TiN [62], is more easily attacked by XeF_2.

In order to eliminate the potential problem with oxidation, the TiN samples were instead annealed in vacuum inside the CNT growth chamber as part of the CNT growth process, which already included a short pre-growth annealing step (see Section 2.2.1). Simply extending this high-temperature heating step was effective in removing most of the stress from the TiN layer. As seen in Figure 2-3, devices that had been annealed in this manner were largely unaffected by the subsequent XeF_2 release step and were free from warps and cracks caused by stress in the TiN layer. In later samples, even the extended annealing step was abandoned as the heat treatment occurring naturally from the CNT growth process, without further modifications, was sufficient in removing most of the residual stress. Section 2.4.1 will discuss the TiN oxidation issue in greater detail. On an interesting note, the cantilever shown in Figure 2-3 had been designed with small chromium strip at the base for the purpose of stress-induced folding [12]. However, cantilever folding did not occur as the annealing process had unintentionally removed all of the stress from the chromium layer as well.

31

(a)   (b)
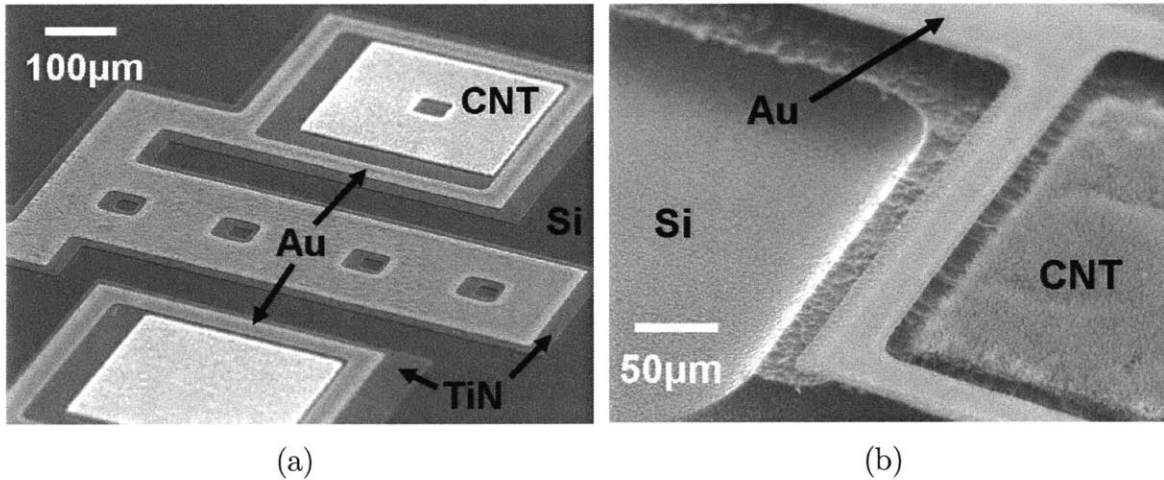
Figure 2-2: (a) an unreleased origami device consisting of TiN, Au, and in situ grown CNTs on a silicon substrate; (b) same device after 10 minutes of etching in XeF$_2$. All of the TiN layer has been etched away along with the silicon.
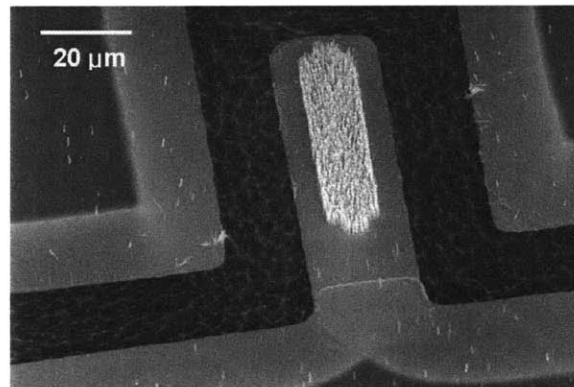
Figure 2-3: A released TiN cantilever covered with *in situ* grown CNTs. The device was annealed naturally during the CNT growth process.

2.1.3 Electrical resistivity

As mentioned before, electrical conductivity is one of the most important reasons for choosing TiN as an origami membrane material. Although nowhere near as conductive as gold, the benchmark of conductive materials, whose resistivity is approximately 2.2 $\mu\Omega$-cm [66], titanium nitride, with its lowest reported resistivity value of 20 $\mu\Omega$-cm [67], is sufficiently conductive for most device applications. However, the reported values of resistivity for TiN ranges anywhere from 20 $\mu\Omega$-cm to 25 mΩ-cm [59, 62, 67]. Creemer

32

et al. reported that TiN resistivity is actually highly dependent on stress and was able to increase the resistivity of TiN from 57 $\mu\Omega$-cm to 3.6 mΩ-cm by simply relieving the stress in the material [68]. In our own devices, the resistivity, as measured through a four-point probe, was 61 $\mu\Omega$-cm prior to CNT growth and 113 $\mu\Omega$-cm afterwards, indicating stress reduction in the TiN layer upon CNT growth as expected.

2.2 *In situ* growth of carbon nanotubes

Although a great deal of research has focused on understanding the mechanism and kinetics of PECVD-based growth of CNTs, there is still much uncertainty associated with the actual growth process. As a result, successful PECVD growth of CNTs, even on commercially available machines, usually involves a long trial and error period to correctly adjust the dozens of variable growth parameters. Even worse is the fact that a correctly adjusted CNT growth system does not always yield consistent results. Various findings regarding the PECVD growth of vertically aligned CNTs at MIT's MTL facilities will be discussed in the following sections.

2.2.1 Growth process and results

Carbon nanotubes were initially grown in the MTL using a PECVD-based CNT growth chamber built in-house by Professor Sang-Gook Kim's research group (Micro & Nano Systems Laboratory). Although the machine allowed complete manual control over a multitude of growth parameters and consistently grew fantastic CNTs, it was not optimized at the time for uniform growth over large areas. Since we wanted to pursue wafer-scale processing, the more recently acquired and commercially available Black Magic CNT deposition system produced by Nanoinstruments, Ltd. (see Figure 2-4) was used to produce all the CNT results shown below. The main advantages of the Black Magic system include fully-automated operation and 6-inch wafer processing capabilities. For most growth processes, the "Two_Step_AC" recipe was used with a 30 second "catalyst annealing time" and 1200 second "CNT growth time."

Figure 2-4: The commercially available Black Magic CNT deposition system produced by Nanoinstruments, Ltd. located inside the MTL.

For either machine, the PECVD-based growth of CNTs takes place in two stages. In the first stage, the sample's temperature is ramped up, in vacuum, to the final growth temperature of between 600°C and 700°C. During this time, the surface of the catalyst layer, typically a 20-30 nm thick layer of nickel (Ni) or cobalt (Co), forms round nucleation sites from which the CNTs will later grow. Figure 2-5 shows the surface of a Ni catalyst which has started to form small, round islands with diameters on the order of the eventual CNT diameter. This diameter is largely a function of the initial catalyst thickness. Near the end of this heating stage, ammonia gas is flown into the chamber to further etch away the catalyst surface [30]. Carefully controlling the time and amount of ammonia flow at this stage can further create variations in CNT diameter and density. Additionally, the catalyst layer can be nanopatterned prior to the CNT growth through e-beam lithography as shown in Figure 2-6. In this case, only a single strand of CNT with a diameter approximately equal to that of the pre-patterned catalyst will grow from each site; however, the slow and serial nature of the e-beam lithography process precludes this method from being used in creating larger arrays of CNTs.
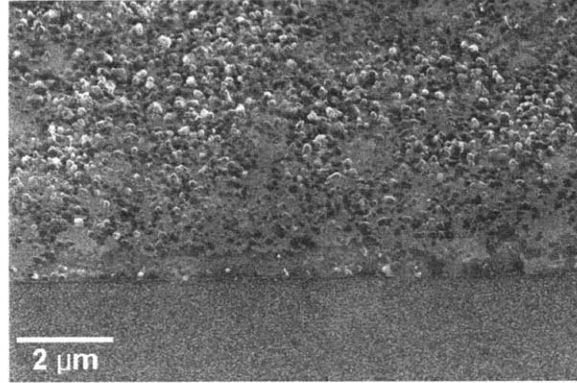
Figure 2-5: An unpatterned Ni layer following pre-growth annealing. The initially smooth catalyst film has nucleated into spherical CNT growth sites.
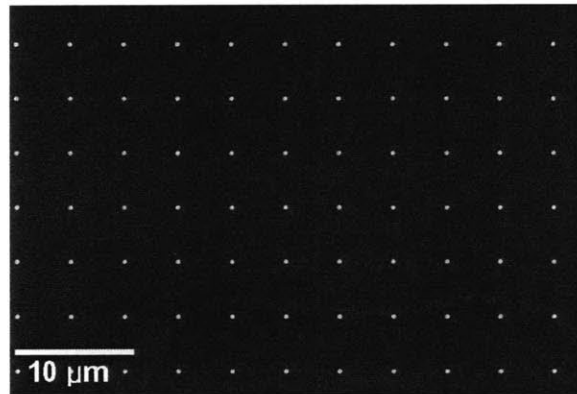
Figure 2-6: A Ni catalyst layer that has been patterned via e-beam lithography prior to CNT growth. Each dot is approximately 200 nm in diameter. A single CNT strand will subsequently grow from each site.

During the second stage of growth, the gaseous hydrocarbon, in our case acetylene, is added to the ammonia flow to provide the necessary carbon. A 4:1 flow ratio of ammonia to acetylene was typically maintained as is the convention. It is widely thought that ammonia acts to etch away the buildup of excess carbon on the top surface of the catalyst tip to allow continued adsorption of the gas species and therefore catalytic growth. At this point, the DC plasma is also switched on for reasons mentioned in Chapter 1. Under typical conditions, CNTs grew at a rate of approximately 250 nm / minute to a maximum length of approximately 10 μm. The typical CNT diameter and density were 150 nm and 9 CNTs/μm^2, respectively. Figure 2-7 shows SEM images of

such CNTs grown from a patterned Ni catalyst layer deposited through lift-off on a patterned TiN layer. Figure 2-7(c) clearly shows that CNT patches can be precisely shaped by micro-patterning the catalyst layer. All SEM images shown, unless otherwise noted, were taken at a tilt angle of approximately 30° with respect to the vertical, meaning that all images appear compressed by a factor of around two in the vertical direction. The CNTs in Figure 2-7(b), for example, are around 4 µm in length despite appearing to be about the same size as the horizontal scale bar of 2 µm. Figure 2-8 shows a top-down view of the same sample after all the CNTs have been physically flattened using a razor blade. Due to the difficulty of obtaining a side view of the CNT array in an SEM, the razor-flattening technique was often used to determine the true size and shape of the CNTs grown.

Figure 2-9 shows the result of CNT growth using the e-beam pre-patterned catalyst layer shown Figure 2-6. For single-strand growth, the previously mentioned heating and ammonia etching steps prior to plasma-enhanced growth must be reduced to ensure that the nano-patterned catalysts are not completely etched away. The missing nano-tubes in the period array shown in Figure 2-9 are likely a result of such overetch.
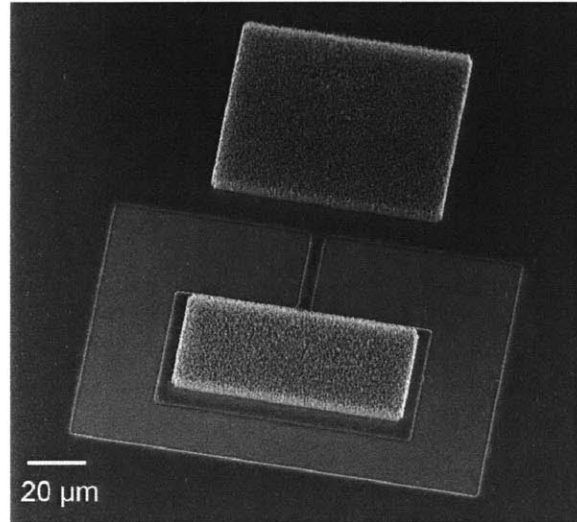
(a)
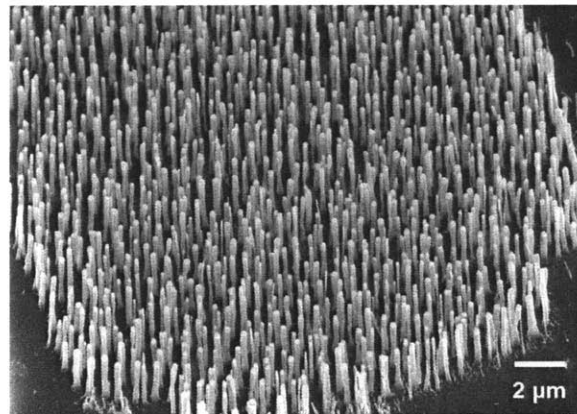
(b)
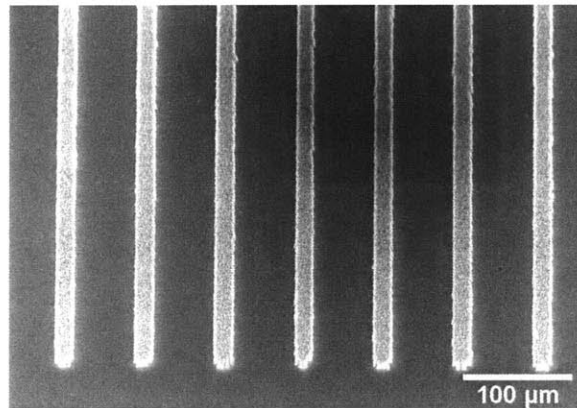
(c)

Figure 2-7: SEM images of CNTs grown directly on TiN using a Ni catalyst layer. The desired shape of the CNT forest (a-c) can be controlled through appropriate lift-off patterning of the catalyst layer prior to growth.
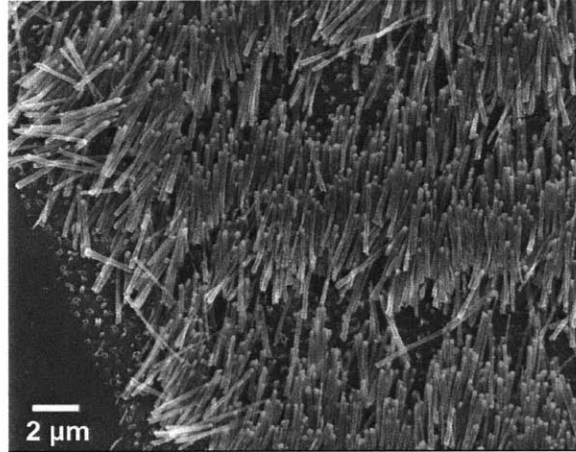
Figure 2-8: Top-down SEM image of a razor-flattened CNT array, showing the exact side profile of the nanotubes and the embedded catalyst.
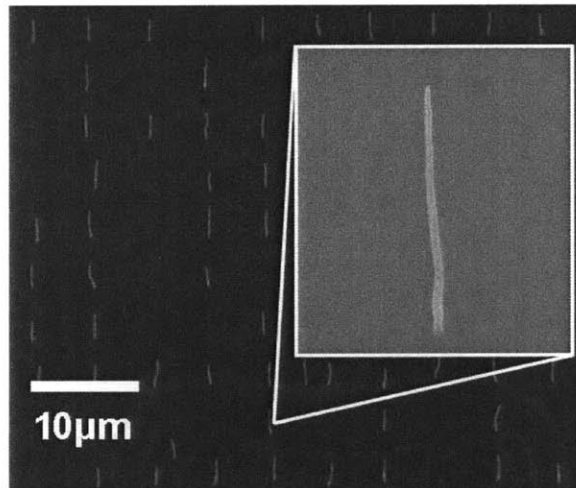
Figure 2-9: Single strands of CNTs grown from catalyst sites pre-patterned through e-beam lithography.

As mentioned before, the PECVD growth of CNTs is not a perfect science, and even with a fully-automated CNT growth equipment, much CNT variation exists across batches. One of the main reasons for this, for both the home-built and commercial machines, is that there is constant carbon buildup inside the growth chamber. Excess carbon buildup greatly affects the quality of the plasma, and if severe, can lead to arcing between the anode and the sample. Figure 2-10 shows a sample that has been com-

pletely destroyed by the arcing of the plasma. To minimize plasma variation, the chamber should ideally be cleaned before each run, although due to practical reasons, it is only done once per every ten runs or so in the MTL. As a result, there is a marked degradation in plasma and CNT quality as excess carbon builds up inside the chamber. One of the reasons that the home-built CNT machine more consistently produced higher quality CNTs might be due to the fact that it was rigorously cleaned before each run.
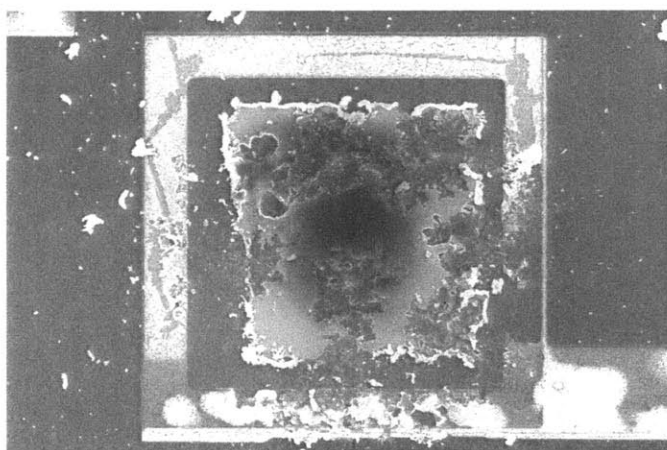
Figure 2-10: CNT and Au sample severely destroyed by unstable plasma conditions during the growth process.

Besides variations in the plasma due to carbon buildup, slight variations in gas flow was found to greatly affect the resulting CNTs. Although a 4:1 flow ratio of ammonia to acetylene was typically used, minor variations had to be made, through trial and error, to account for different catalyst material, catalyst thickness, plasma condition, and etc. The plasma condition, which affects gas ionization, is believed to be the main factor contributing to the necessity of slight gas flow adjustments. Figure 2-11 shows CNTs that were grown in a slightly carbon-deficient environment (around 4.1:1 flow ratio). Upon closer inspection, the CNT bodies show a noticeable lack of structural integrity. For such cases, the carbon content of the gases is increased by increasing acetylene flow, decreasing ammonia flow, or both. Figure 2-12 shows the opposite case in with the

CNTs were grown in a slightly carbon-rich environment (around 3.8:1 flow ratio). The conical shape is a result of lateral growth due to the precipitation of excess carbon [69]. The mechanism is shown graphically in Figure 2-13. In such a case, the acetylene content must be decreased, the ammonia content increased, or both. Although the CNT samples shown in Figures 2-11 and 2-12 were intentionally grown in carbon deficient or rich environments, there were many instances when similar CNT growth was inexplicably exhibited for previously-proven gas ratios. During such times, the gas flow should be adjusted accordingly, gas tank levels checked, and/or the growth chamber cleaned.
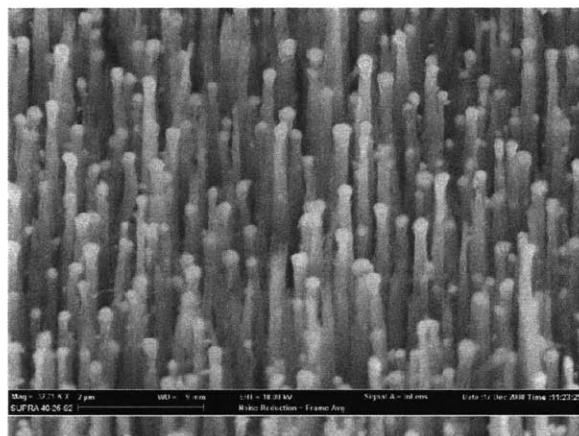
Figure 2-11: CNTs grown in a carbon-deficient environment.
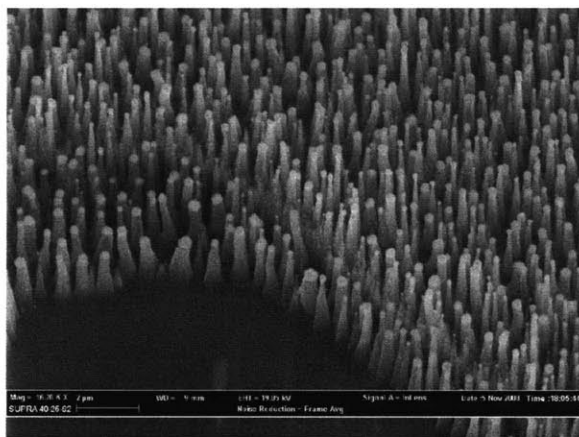
Figure 2-12: CNTs grown in a carbon-rich environment.

On a final note, a Ni catalyst layer was predominantly used throughout our study for CNT growth as is also the overwhelming case in literature. However, CNTs grown from Co possess certain additional benefits, as will be shown in Chapter 4, and were grown as shown in Figure 2-14. Figure 2-14(a) shows the typical growth result. It appears that the catalyst nucleation process for Co is different from that of Ni, and as a result, the controlled and consistent nanotube growth observed with Ni catalysts could not be replicated with Co catalysts. Additionally, the Co CNTs tended to be less vertically aligned compared to their Ni counterparts. The exact reason for this is yet unknown as is the precise mechanism behind plasma-aligned CNTs. Still, well-aligned and relatively uniform growth of Co CNTs should be possible with further optimizations in the catalyst deposition and CNT growth steps as it was observed *one* time for a single mystery batch of Co CNTs shown in Figure 2-14(b). Unfortunately, such results could not be repeated in subsequent processes using similar samples and recipes.
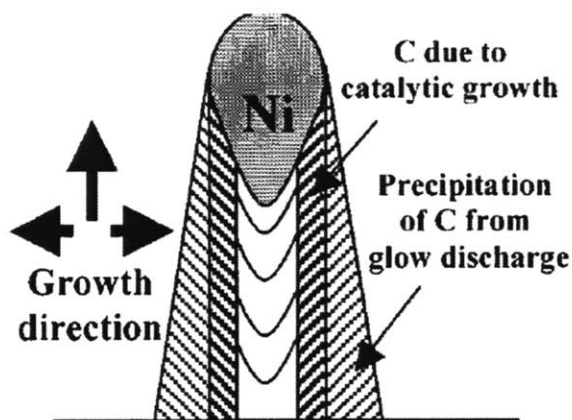
Figure 2-13: Growth mechanism schematic of a CNF [69].
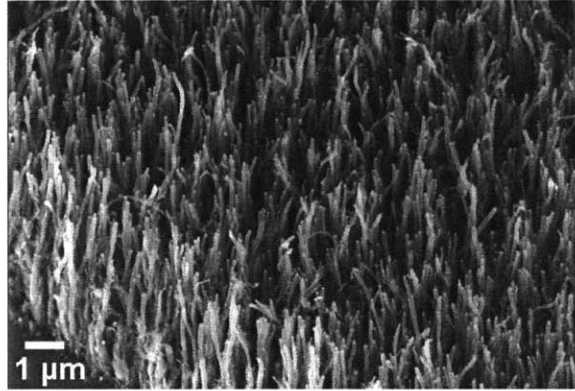
(a)
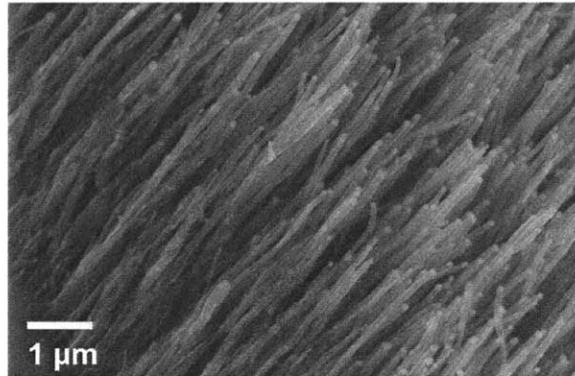
(b)

Figure 2-14: (a) typical Co CNT growth and (b) one time-achieved Co CNT growth.

2.2.2 Effect of membrane on CNT growth

It was previously mentioned that the origami membrane should not inhibit catalytic growth of CNTs on its surface. One of the reasons that TiN was selected as the membrane material was that it has the added benefit of improving catalytic efficiency during CNT growth by eliminating the formation of silicides [70] and preventing the diffusion of catalyst materials into the substrate [71]. When CNTs are grown on a Si substrate using a PECVD-based method, the catalyst material invariably forms silicides under the high temperature growth conditions. Titanium nitride, an excellent diffusion barrier material, prevents this from happening. Silicide formation and catalyst diffusion can significantly affect the catalytic efficiency of the catalyst material and impact CNT growth in ways that are not entirely clear at this time. Figure 2-15 demonstrates the difference between CNT growth on TiN and Si. In Figure 2-15(a), a typical 30-second

heating and ammonia etching step preceded the plasma-enhanced growth step. The SEM image clearly shows that CNTs grown on top of TiN are much longer and more uniform compared to CNTs grown on Si. In fact, the thick and oddly shaped growth on top of Si indicate that sufficient nucleation of catalytic growth sites had not occurred. On the other hand, CNTs resulting from an unusually long 4-minute pre-growth heating and etching step are shown in Figure 2-15(b). Here, it is seen that CNTs grown on Si look much more pronounced that those on TiN. The thin, hair-like shape of CNTs grown on TiN is indicative of an overly etched catalyst nucleation site. From these images, it can be seen that catalyst layer deposited on top of TiN quickly and consistently nucleates into CNT growth site while catalyst deposited on top of Si requires further heat treatment and ammonia etching to transform into suitable CNT growth sites.
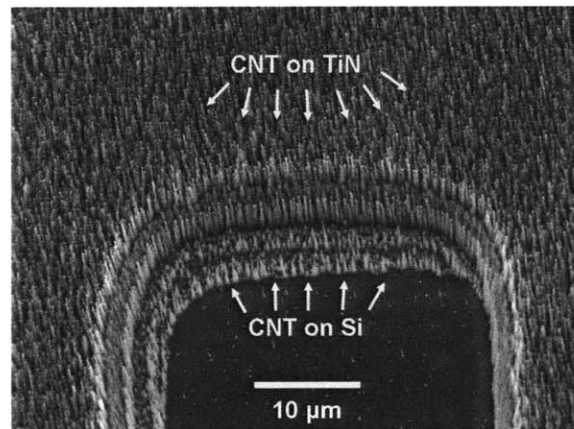
(a)
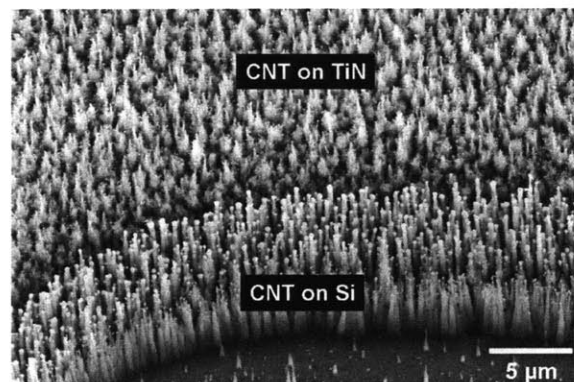
(b)

Figure 2-15: SEM images showing the difference between CNTs grown on TiN and Si. (a) short ammonia pre-etching time and (b) long ammonia pre-etching time.

2.2.3 Nanotubes vs. Nanofibers

Thus far, we have not differentiated between (CNTs) and carbon nanofibers (CNFs). However, it is widely thought that true CNTs, namely the nanoscale tubes consisting of perfectly rolled up sheets of graphene, cannot be grown via PECVD methods. This is mostly attributed to the low growth temperatures associated with PECVD-based growth [39]. Rather, many researchers refer to the PECVD-based, deterministic growth of carbon nanostructures as CNFs as such structures lack single crystal grains in the direction of the aligned fibers [39, 69].Others, nevertheless, still refer to them as CNTs since they have a hollow core [30, 32]. The typical structure, as shown in Figure 2-16, consists of graphene walls that are not perfectly parallel with each other as they are in true CNTs. Wen *et al.* [32] hypothesizes that this behavior might be a function of the catalyst particle's size and shape; large catalyst particles with a pointed shape as shown Figure 2-16(a) result in structures with slanted sidewalls while smaller, tubular particles as shown in Figure 2-16(b) result in perfectly parallel sidewalls. The CNTs grown in our facilities resemble that of Figure 2-16(a) with the characteristic hollow core and slanted graphene sidewalls as shown in the TEM images in Figures 2-17 and 2-18. While the non-crystalline CNFs cannot replace CNTs in applications that rely on their semiconducting or optoelectronic properties, the CNFs' still excellent mechanical and electrical properties make them suitable substitutes for CNTs in most other application fields.

(a)   (b)
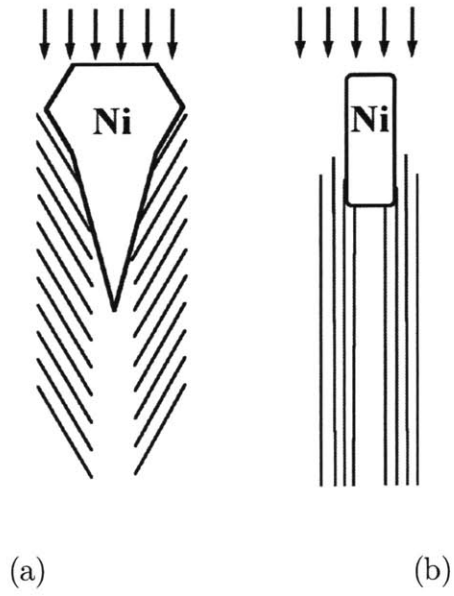
Figure 2-16: CNT growth modes for large, faceted catalyst tips (a), and small, cylindrical catalyst tips [32].
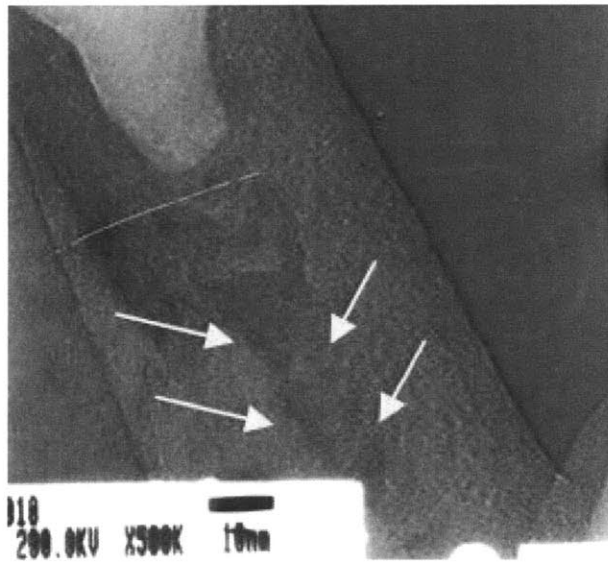
Figure 2-17: TEM image showing (indicated by arrows) the hollow core of our PECVD-grown CNTs.
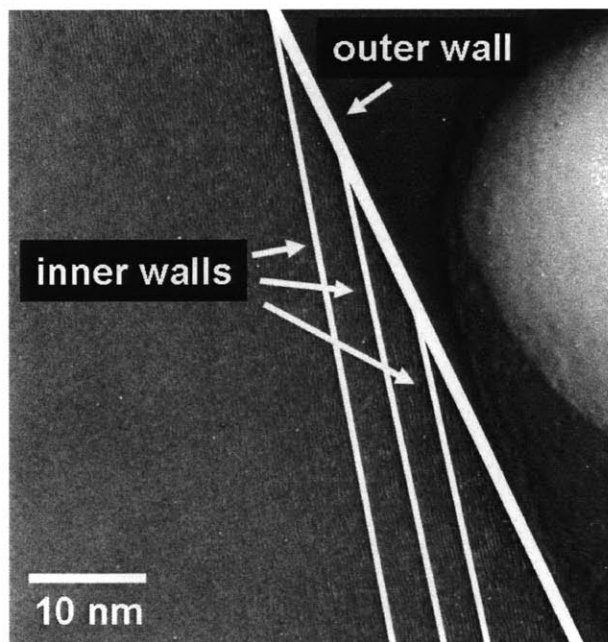
Figure 2-18: TEM image showing (indicated by lines and arrows) the slightly slanted graphene walls of our PECVD-grown CNTs.

2.3   Metallization methods

Past origami devices have relied on a patterned gold layer for metallization. This metal layer served the critical dual purpose of providing electrical connections to the various parts of the device while acting as a ductile hinge that connected the different folding parts of the origami device [11, 13, 16]. However, the gold layer, which was typically deposited right on top of the silicon substrate, is not amenable to high-temperature processing associated with CNT integration. Figure 2-19 shows an example of what can happen to a gold-on-silicon structure after undergoing a high-temperature CNT growth cycle. The images show deep cavities and various other distortions that have appeared on the gold surface due to the diffusion of Au and the formation of Au-Si alloys. In fact, Cheng *et al.* have utilized this silicon-to-gold eutectic bonding effect to create lasting bonds for MEMS packaging applications [72]. Similar results were also observed for other commonly used metals such as aluminum (Al) and chromium (Cr).

(a)   (b)
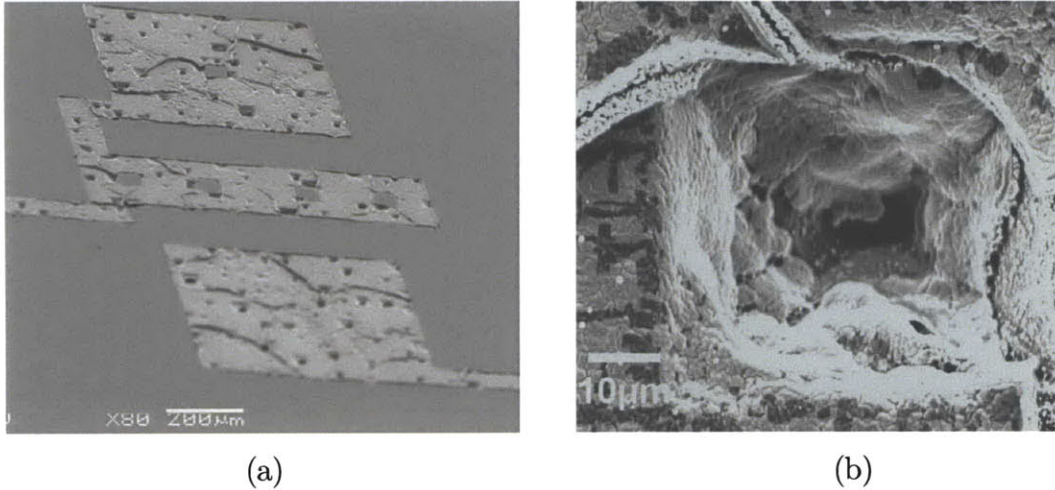
Figure 2-19: (a) Gold-on-silicon structure after undergoing a high-temperature CNT growth cycle. (b) zoom-in image.

2.3.1 Pre-CNT metallization

In order to prevent the unwanted diffusion of gold into silicon as well as other undesirable deformations of the metal layer, the TiN layer, already used as a base for CNT growth, was placed below the gold as well to act as a diffusion barrier layer. The general processing steps are outlined in Figure 2-20.
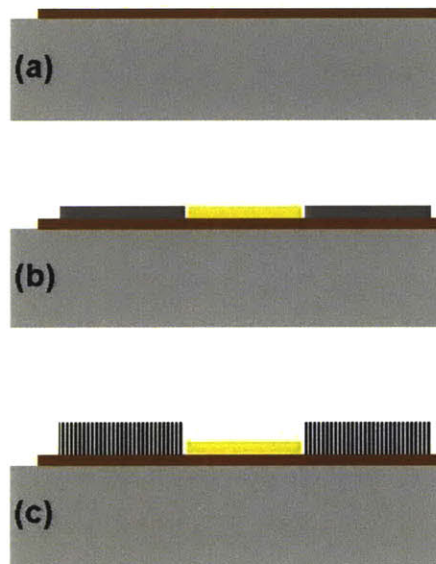
Figure 2-20: Overview of pre-CNT metallization technique: (a) TiN layer is deposited/patterned; (b) catalyst layer as well as other metal layers are deposited/patterned through separate lift-off processes; (c) CNTs are grown on the catalyst sites.

47

As can be seen in Figure 2-21, the TiN layer did indeed prevent the gold from diffusing into silicon. However, it can also be seen that the gold layer has been severely distorted and has actually peeled off in certain areas. This is likely explained by a combination of: (1) high local temperatures approaching the melting point of gold; (2) changes to the thin (20 nm) Cr adhesion layer sandwiched between Au and TiN; and (3) coefficient of thermal expansion mismatch between Au and TiN. Subsequent measurements also indicated that the electrical resistivity of the gold layer had risen significantly. Although it was not tested, the mechanical behavior of the Au hinges most likely changed considerably as well. The pre-CNT metallization technique is not entirely without merit, however. By increasing the Cr adhesion layer thickness, increasing heating ramp-up and ramp-down times, and lowering the growth temperature, gold layer distortion can be kept to a minimum as seen in Figure 2-22. However, slight discoloration and surface roughening of the gold layer as well as an increase in resistivity is still observed.
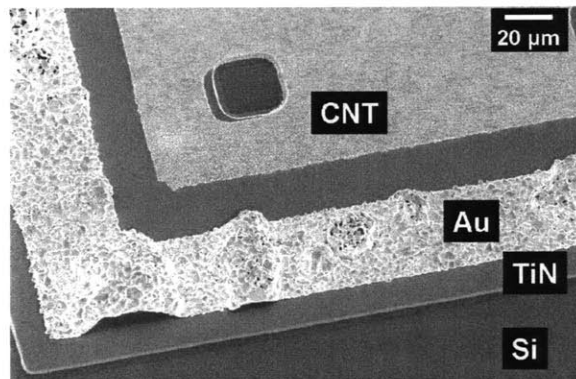
Figure 2-21: Severe distortion and peeling-off of Au on TiN following CNT growth.
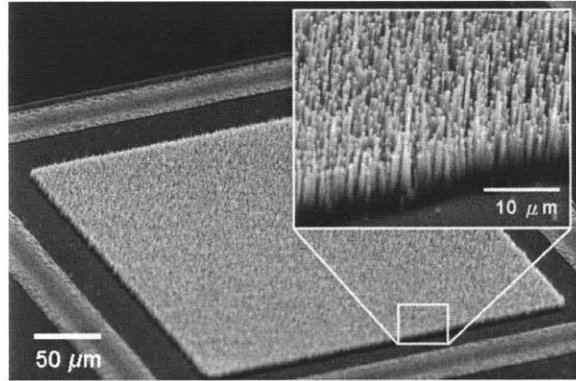
Figure 2-22: Minimally distorted and well-adhered Au on TiN following CNT growth. Resulting CNTs are shown in the inset.

2.3.2 Post-CNT metallization

The post-CNT metallization method altogether bypasses having to place metals into the high temperature CNT growth chamber. In this approach, all of the metal deposition and patterning steps are performed subsequent to CNT growth using a revolutionary triple-coating lift-off patterning technique. The general process for this lift-off process is outlined in Figure 2-23, and the exact recipe is given in Appendix A.1.

In short, an image reversal photoresist is used to cover the entire wafer, including the CNTs. During this process, it is crucial for the tips of all CNTs to be completely covered by the photoresist. In the MTL with AZ 5214 photoresist, this typically occurred when the photoresist thickness reached approximately 75% of CNT length. At this point, the photoresist is opened up, using optical lithography, in areas where we want metal deposition to occur. After the subsequent metal deposition step, the wafer is placed in an acetone bath where all of the photoresist, along with the unwanted metal, is removed.
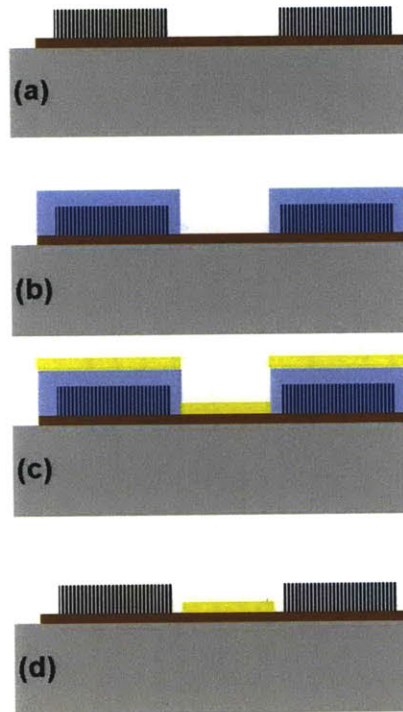
Figure 2-23: Overview of post-CNT metallization technique: (a) CNTs are grown on TiN; (b) Entire device, including CNTs, is covered by photoresist and selectively exposed; (c) Desired metal layer is deposited over the entire device; (d) Acetone soak removes all photoresist and the metal layer on top of them leaving only the desired metal features.

One initial concern for this technique was whether or not the CNTs would be able to withstand the photoresist deposition and removal process without incurring structural damage or sticking to each other due to capillary forces. Consequently, a simple test was performed by soaking a photoresist-covered CNT array in acetone. To accelerate the photoresist removal process, the acetone bath was further subjected to up to five minutes of ultrasonic sonication. After the soak, the samples were simply rinsed with isopropyl alcohol (IPA) and dried with a nitrogen gun. A test sample with partial photoresist removal is shown in Figure 2-24. The dark region indicates areas where some photoresist is still remaining while the bright region indicates areas in which all of the photoresist has been removed. The CNT array does not seem to have been affected in any way following the test.
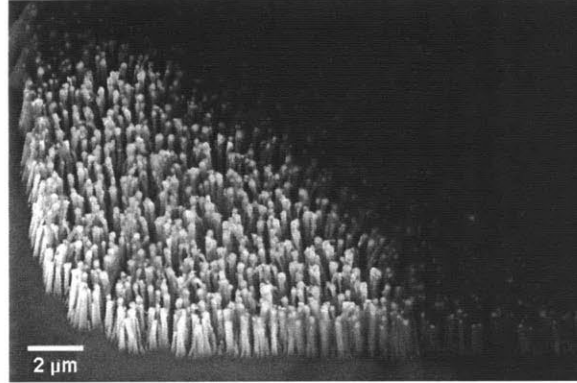
Figure 2-24: SEM image of partially washed off photoresist on CNT. The photoresist-free and thus more conductive region CNT appears brighter in the SEM and looks damage-free.

A final device, consisting of patterned gold and CNT layers on top of a TiN layer, that was fabricated using the post-CNT metallization technique is shown in Figure 2-25. Unlike the distorted gold layer seen earlier following pre-CNT metallization, the gold layer here appears quite smooth and undamaged. The CNT array seems to be intact as well. This technique is compatible with all materials that can be evaporated or sputtered safely on top of a photoresist and is an excellent method for providing patterned metal layers to CNT-origami devices, as long as the CNTs can be completely covered by photoresist. Figure 2-26 shows an example of a failed lift-off attempt in which the photoresist had not entirely covered the CNT and the gold has thus irreversibly been deposited on top of the CNTs.
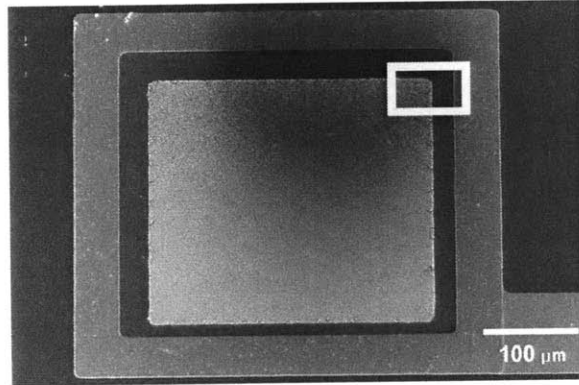
(a)
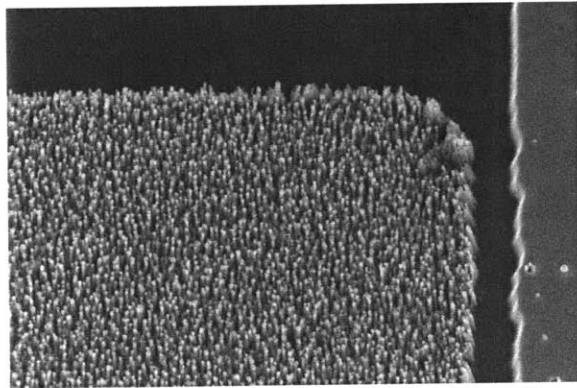
(b)

Figure 2-25: CNT and Au structures on TiN following post-CNT metallization. Closeup of (a) is shown in (b).
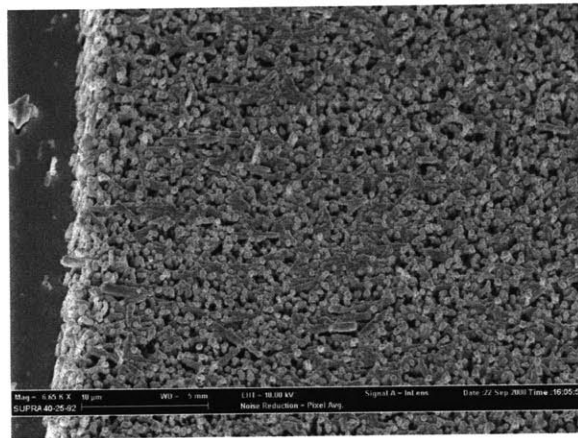
Figure 2-26: Failed sample following post-CNT metallization.

2.4 XeF$_2$ etching: The art of the release

Xenon difluoride (XeF$_2$)-based isotropic dry etching of silicon, as mentioned in previous sections, is commonly used to release the membrane layer of origami devices and exclusively so for origami devices integrated with CNTs. The use of XeF$_2$ etching, a completely dry and room temperature process, is highly advantageous because it does not require an additional sacrificial layer, exhibits very high etch selectivity towards silicon, and eliminates various problems associated with wet etch-based release procedures, such as stiction and physical damage during rinsing. A more detailed description of the etching mechanism, equipment, and procedure for XeF$_2$ etching can be found in my master's thesis [10] and will not be repeated here.

This section will instead focus on the particular challenges associated with successfully releasing CNT-origami devices built on TiN membranes. A successful release process essentially boils down to being able to etch away all of the silicon lying underneath the release area before any of the other non-silicon structures on the device are adversely affected by the etching process. As with all selective etches, materials will rarely exhibit infinite etch resistance to the volatile etchant, in this case XeF$_2$; eventually some unintentional structural damage will occur. For the case of TiN membranes, its lower than expected resistance to XeF$_2$ etching resulted in several crucial changes that were made to the overall design as well as the release process as outlined below.

2.4.1 Reducing oxidation

Earlier in Section 2.1.2, it was mentioned that TiN, which had been annealed and inadvertently oxidized at high temperatures in an open air environment, was highly susceptible to XeF$_2$. To overcome this problem, TiN oxidation was minimized by performing the stress annealing step *in vacuo* as part of the CNT growth process. As shown previously in Figure 2-3, there was a marked reduction in TiN damage during release following this procedure. However, TiN susceptibility during release was not entirely eliminated as it continued to etch, albeit at a much slower pace, in XeF$_2$. While this was not a problem for smaller devices that released quickly from the substrate or for devices made from thicker TiN membranes, it became problematic for devices like

the one shown in Figures 2-27 that was made from a TiN layer only 100 nm thick and required a much longer lateral etch of the underlying silicon compared to the device shown in Figure 2-3 (i.e. required longer etch times). Figure 2-27(b) shows that after a moderate period of XeF_2 etching, all of the TiN has been completely etched away.

Since unannealed TiN showed excellent etch resistance to XeF_2, it was apparent that the high-temperature annealing/CNT growth steps were somehow responsible for decreasing TiN's etch resistance. While there are many theories regarding the exact mechanism behind increased TiN susceptibility to XeF_2 after CNT growth, post-CNT room temperature oxidation of the TiN layer was determined to be one of the main causes. While room temperature oxidation of TiN typically does not extend beyond a thin surface layer measuring only a few nanometers, Logothetidis *et al.* reported that TiN that is not perfectly stoichiometric will oxidize at room temperature as the weakly bonded nitrogen in the material leads to deep diffusion of oxygen through the grain boundaries [73]. We further believe that this process is more prevalent in TiN that has been "activated" through high temperature processing. Figure 2-28 plots the volume fraction of oxidized TiN as a function of time, as measured by Logothetidis *et al.* using a Bruggeman effective medium approximation (EMA) method, and shows that it increases exponentially upon air exposure. While the exact stoichiometry of our TiN layer as well as the precise extent of its oxidation are not known, it was quite clear from experimentation that the TiN layer in samples released with XeF_2 immediately follow- ing CNT growth showed much less damage compared to samples released a few days following CNT growth. In fact, the badly damaged sample shown in Figure 2-27(b) was subjected to XeF_2 etching about a week after the CNTs had been grown on it. Figure 2- 29 shows an almost identical device that went through the XeF_2 etching process imme- diately after being removed from the CNT growth chamber; the TiN membrane is fully released and does not exhibit significant signs of damage.

Through numerous experiments, it was shown that simply minimizing the air exposure time between the CNT growth step and the XeF_2 etching step proved suffi- cient in reducing TiN damage during release. However, due to various practical reasons, the release step could not always be performed directly after CNT growth. In those

instances, it was discovered that simply keeping the samples in a common hand-pumped vacuum canister was sufficient in achieving similar results.
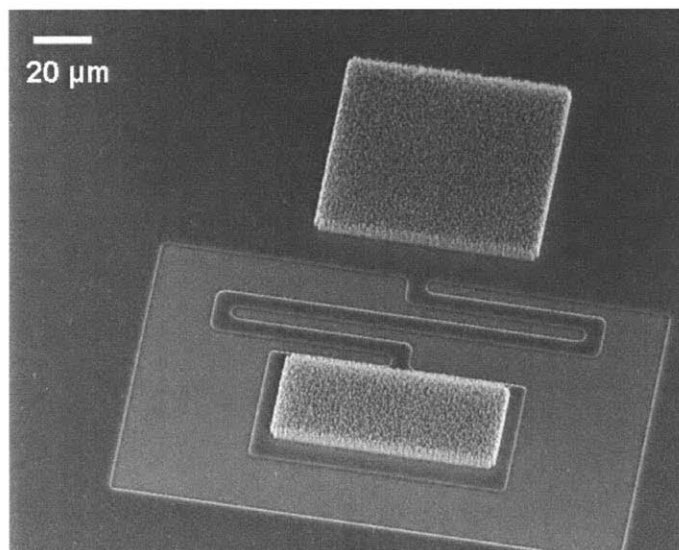
(a)
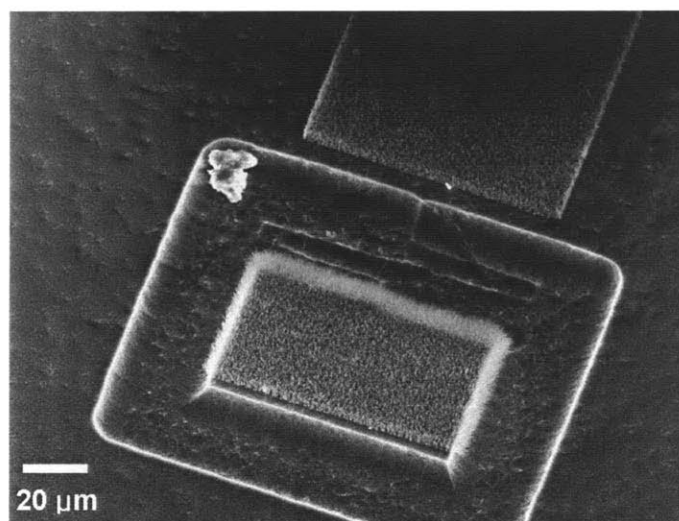
(b)

Figure 2-27: CNT-on-TiN structures (a) before and (b) after XeF$_2$ etching. The release step took place several days after the CNT growth step. Almost all of the TiN layer has been completely etched away in (b).
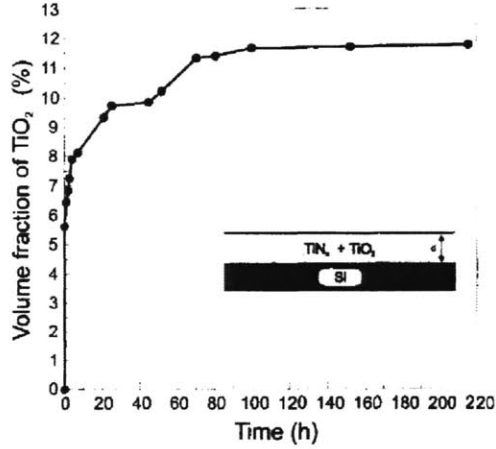
Figure 2-28: Plot of volume fraction of TiN oxidation at room temperature as a function of time left in air [73].
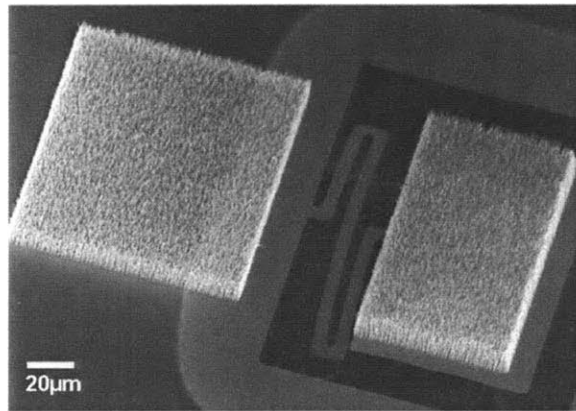
Figure 2-29: A fully released CNT-TiN structure showing almost no signs of TiN damage from the XeF$_2$. The sample was placed into the XeF$_2$ chamber for release immediately following the CNT growth step.

2.4.2 Minimizing TiN exposure

Minimizing the actual amount of TiN that is exposed to XeF$_2$ gases during the release process is another highly dependable method for reducing TiN damage. For most CNT-origami devices, such as the supercapacitor that will be presented in Chapter 3, much of the TiN layer's top surface is covered by other materials that serve various functional and structural support roles. In the abovementioned supercapacitor device, for example,

the entire top surface of the TiN membrane is covered by a thick polymer layer (SU-8) for structural support and chemical protection except for a small opening in the layer that exposes the underlying CNT forest and the TiN membrane on which it is grown. In this configuration, only the small exposed area of TiN, as seen in Figure 2-30(a), is attacked by XeF_2. Since most of the XeF_2 etching occurs on the top surface, where much more etchant gases are available, merely covering the top surface of the TiN layer will stop most of the damage.

In addition to parts of the TiN layer in Figure 2-30(a) that is covered by the thick layer of SU-8, it can also be seen that parts of the TiN layer covered by the vertically aligned arrays of CNTs have also been protected from XeF_2 damage. For reasons that will be explained further in the proceeding section, CNT forests have also been found to be highly effective in protecting the underlying TiN layer from XeF_2 gases. In fact, closer inspection of the severely damaged device shown in Figure 2-27(b) shows that the patches of CNT forest, and thus the underlying TiN layer, are still intact. This fact is also shown in Figure 2-30(a) where TiN damage is limited to areas that are not covered by CNTs. Figure 2-30(b) shows how a simple design change, in which the SU-8 opening is reduced to completely cover the exposed TiN layer, can effectively stop unwanted TiN damage by XeF_2.

(a)   (b)
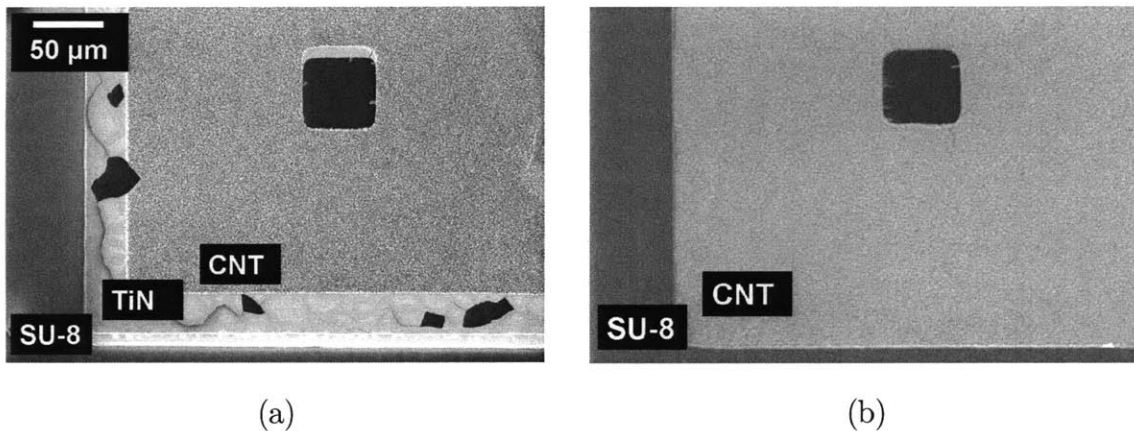
Figure 2-30: Post-release SEM images of SU-8-covered CNT-TiN layers. Device in (a) shows the small area of exposed TiN that has been damaged by XeF_2 while the one in (b) shows no visible damage due to lack of exposed TiN areas.

2.4.3 Etch holes

Besides reducing TiN oxidation and exposure, another way to minimize unwanted damage during the release step is to increase the number of etch holes and thereby reduce the overall etching time. Figure 2-31 shows a TiN device designed for rapid release with equally distributed 5um etch holes.
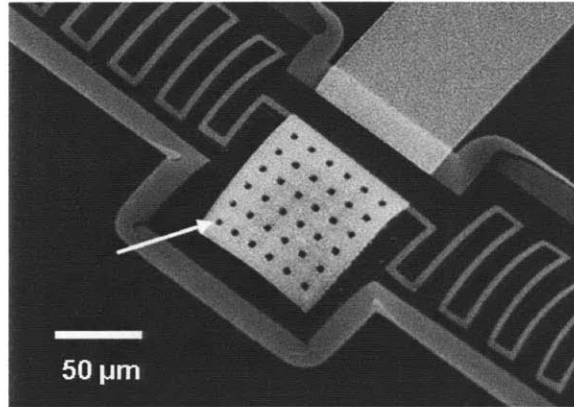
Figure 2-31: Released TiN device with equally spaced 5 µm etch holes.

The device shown in Figure 2-31 released successfully within 2 minutes of XeF_2 etching, which was less than one quarter of the time required to release similar devices without etch holes. Consequently, very little TiN damage was observed. However, in earlier samples, no silicon etching was observed through the etch holes. It was as though the etch holes were not there at all. Based on the following equation [74]

$$\lambda = \frac{RT}{\sqrt{2}\pi d^2 N_A P},$$
(2.1)

where R is the universal gas constant, T is the etching temperature, d is the diameter of XeF_2 molecules, N_A is Avogadro's constant, and P is the etching pressure, the mean free path, λ, of XeF_2 during the release process, which takes places at ~2000 mTorr, is found to be approximately 15 µm. This value of λ indicates that the possibility of the XeF_2 molecules hitting the small area silicon exposed by the 5 µm etch holes is very small.

Consequently, very little of the silicon exposed by the etch holes was initially etched during release. Simply raising the etching pressure to ~4000 mTorr, and thus reducing λ to around 7.5 µm, was sufficient in completely eliminating this problem. For all subsequent release processes using small etch holes, the starting etch pressure was raised to at least 3000 mmTorr. A weak vapor pressure of the XeF_2 solid source, however, will make it difficult to achieve the required etching pressure.

2.4.4   Etching time

In order to prevent excess TiN damage, it is important to terminate XeF_2 etching as soon as the desired membrane has been released. However, it is difficult to precisely predict the silicon etch rates during the release process as it is dependent on a multitude of factors, with its complex dependence on opening geometry being one of the most difficult to predict. Figure 2-32 indicates, for example, how the etch depth of silicon depends on the diameter of a circular opening. For this and other reasons, samples being released must be continually monitored to determine the endpoint. Fortunately, discoloration of membranes, as seen in Figure 2-33, that are clearly visible under both optical and SEM observation makes easy to determine when complete membrane release has occurred.
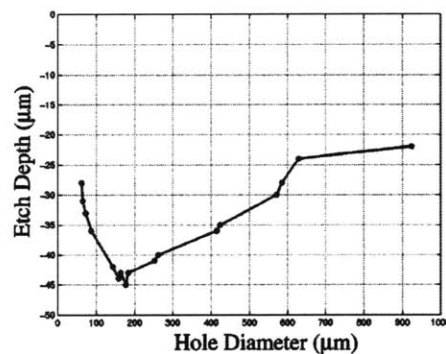
Figure 2-32: Experimental results showing etch depth of silicon as a function of opening hole diameter [74].

59

(a)	(b)
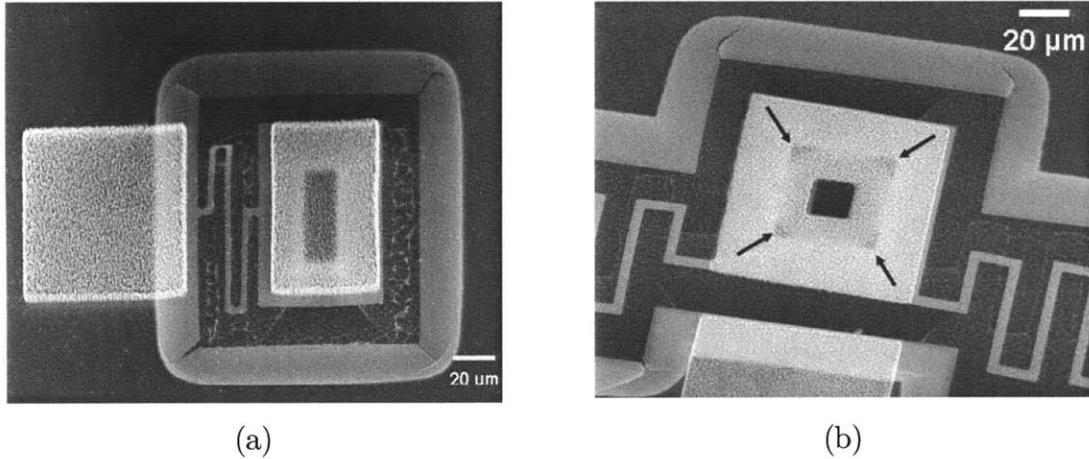
Figure 2-33: Partially released TiN devices where the darker regions (indicated by arrows in (b)) indicates unreleased areas. Device shown in (a) does not have any additional etch holes while the one shown in (b) has one rectangular etch hole in the center.

2.4 Summary of fabrication process

The origami-based fabrication process for the integration of *in situ* grown CNTs, based on preceding discussions, is summarized below in Figure 2-34. This represents only a general overview of the process and certain device-specific variations, as will be outlined in following chapters, may be necessary. Of course, the various fabrication guidelines reported throughout this chapter must be followed while creating these types of origami devices.
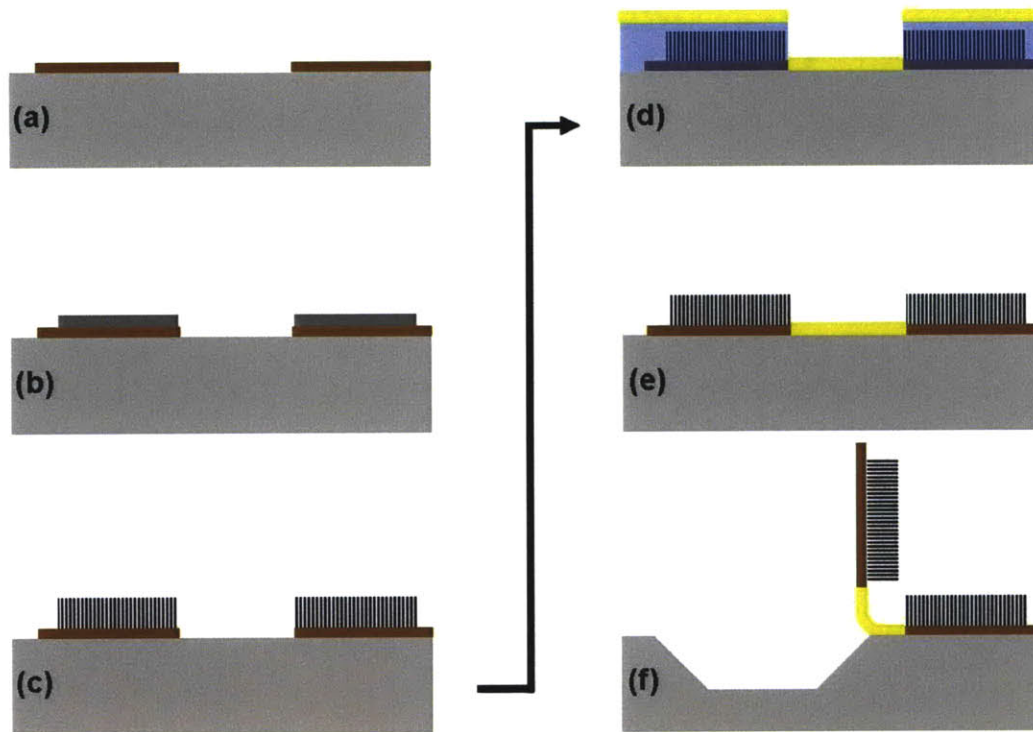
Figure 2-34: Overview of the CNT-integrated origami process: (a) deposit/pattern TiN membrane layer; (b) deposit/pattern CNT growth catalyst; (c) grow CNTs; (d-e) use post-CNT metallization technique to deposit/pattern various metal elements for wiring, hinges, etc.; (f) release desired membrane through XeF_2 etching of the underlying silicon.

Chapter 3

Microfabricated supercapacitor with carbon nanotube electrodes

An electrochemical capacitor, which is now more commonly referred to as a supercapacitor, is a type of capacitor in which the energy is stored within an electrochemical double layer at the electrode/electrolyte interface [75]. Such devices derive their high capacitance mainly from the large surface area of the extremely porous electrode material. Various forms of carbon, including carbon nanotubes (CNTs), make excellent supercapacitor electrodes largely because of their high conductivity and specific surface area [76, 77], and they are commonly used in macroscale devices for many research and commercial applications.

In previous work by the author [10, 13], microfabricated electrochemical capacitors were made by integrating the Nanostructured Origami™ process with a manual carbon-electrode (consisting of a Super P carbon black paste) deposition step. The use of the origami process, which enabled the integration of nanoscale features and 3-D architecture, proved ideal for electrochemical capacitor microfabrication, and the nanostructured electrodes resulted in a 50× increase in capacitance compared to devices without such electrodes [13].

In this chapter, the origami-based fabrication and testing of a microfabricated supercapacitor with nanostructured electrodes consisting of *in situ* grown, vertically-aligned MWCNTs, as seen in Figure 3-1, is presented. The device consists of a single

CNT electrode flap that flips over to create the top/bottom electrode architecture. The process reported herein remains compatible with many MEMS-based processes, thus ensuring integration with pre-existing micro/nano-systems for possible use as an on-chip power source, and because the CNTs are grown *in situ*, no additional electrode deposition or transfer process is necessary. As is the case with macroscale supercapacitors based on CNT electrodes, the densely packed arrays of vertically-aligned MWCNTs in the CNT-origami supercapacitor are expected to provide excellent electrical conductivity, high surface area, and superior electrolyte accessibility due to the presence of larger pores and conductive paths [53, 78]. Figure 3-2 illustrates how creating electrodes out of vertically aligned carbon nanotubes can result in, compared to other high surface area nanomaterials, increased surface area utilization, increased electrical conductivity throughout the electrode matrix, and increased ion mobility. While macroscale electrochemical capacitors based on CNT electrodes have been demonstrated previously [79], the direct growth of the CNTs on the current collector, as opposed to the post-growth transfer of CNTs, will help minimize contact resistance between the CNTs and the substrate while eliminating CNT-to-CNT resistance within the electrode network.
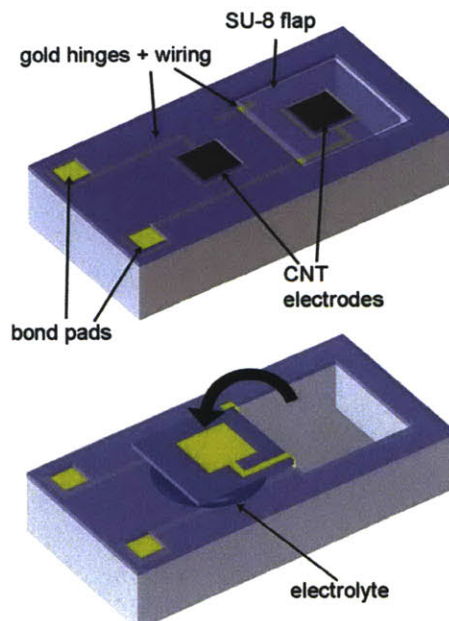
Figure 3-1: Schematic of the CNT-origami supercapacitor before and after the folding process.
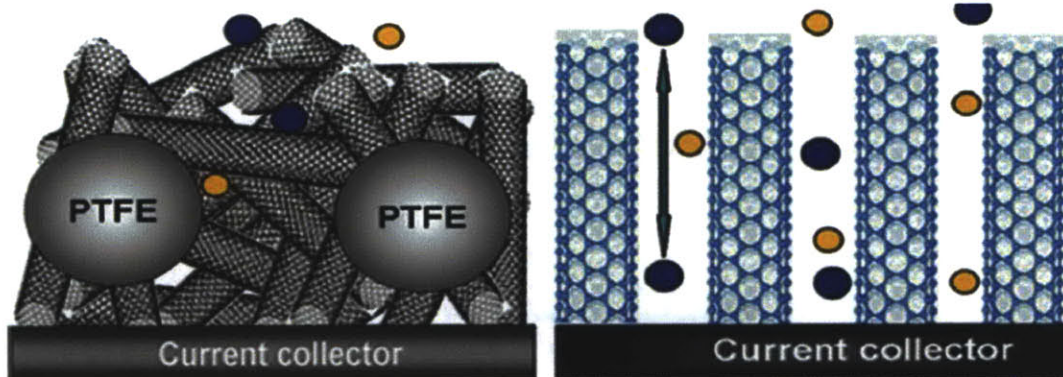
Figure 3-2: Schematic illustrating how the use of vertically aligned CNT electrodes can result in higher surface area utilization, increased electrical conductivity through the electrode, and faster ion mobility [78].

3.1 Fabrication process and results

The fabrication process for the CNT-origami supercapacitor is based closely on the TiN-based process reported in Chapter 2. However, creating a working supercapacitor requires some processing modifications mainly due to the addition of a liquid electrolyte. Fabrication details and results as well as additional processing considerations are described below. The complete processing recipe can be found in Appendix A.2.

3.1.1 Process flow

As mentioned previously, the direct growth of CNTs requires exposure to temperatures as high as 700°C; such high temperatures will damage the current collectors if they are made out of gold, as is customary [10, 13]. Therefore, our CNT-origami process begins by first depositing and patterning two, 150 nm thick TiN current collectors that will later form the opposing electrodes of the supercapacitor (Figure 3-3(a)). At this stage, a thin layer (~20 nm) of nickel (Ni) is deposited on top of the TiN sections to serve as catalysts for CNT growth (Figure 3-3(b)). The TiN layer should provide sufficient electrical connectivity to the nanotubes while serving as an excellent diffusion barrier layer and also enhancing nanotube growth as mentioned in Chapter 2. A densely packed array of vertically-aligned MWCNTs is then grown out of the catalyst layer

following up to 30 minutes of growth in a 4:1 flow of ammonia and acetylene gases under a 150W DC plasma (Figure 3-3(c)). Under the most ideal growth conditions, 30 minutes of growth yielded CNTs that were approximately 10 μm in length. Greater lengths could not be achieved, most likely due to the accumulation of excess carbon on the surface of the catalyst particle. To the best of our knowledge, this is the longest reported length for PECVD-grown CNTs. While 10 μm was the maximum length achieved, the CNTs were typically between 6 and 7 μm in length. Minor variations to the catalyst thickness and other growth parameters yielded nanotubes of different diameters, densities, and lengths. A typical CNT array used in our experiments had a density of ~9 CNTs/μm^2 with individual CNT diameter of approximately 150 nm. A 20 nm thick layer of silicon nitride (SiN) that covers the entire substrate (not shown in the drawing) provides electrical isolation between the device and the silicon substrate. In addition to the use of TiN, direct growth of CNTs on Inconel [55], a type of metallic alloy, as well as a Mo/Al/Fe metal stack [57] have been recently demonstrated by other groups for supercapacitor applications. However, thin film deposition of Inconel is not available in our fabrication facilities, and both materials are incompatible with our release process.

The remainder of the origami fabrication process takes place after the CNTs have been grown. In Figure 3-3(d), a 600 nm thick gold layer is deposited using the previously mentioned post-CNT metallization technique to create the necessary hinge and wiring elements. As shown in the inset in Figure 3-4, the CNTs remained unchanged through the metallization steps. In Figure 3-3(e), a SU-8 layer is deposited and photolithographically patterned around the electrodes to provide overall structural support during and after the folding process. The SU-8 layer is typically ~10 μm thick but the thickness can be adjusted to account for different CNT heights. In the final step of the fabrication process (Figure 3-3(f)), the folding segment is released from the substrate through a XeF$_2$ isotropic dry etching of the underlying silicon. The folding process, outlined in Figure 3-5, is accomplished by applying a small drop (~1 μL) of electrolyte (1M H$_2$SO$_4$) to the device using a micropipette, at which point the loose flap instantly pops up to 90° due to capillary forces [80]. At this point, the same micropipette can be used to draw some of the electrolyte back in, which sucks down the flap thereby causing

it to fold all the way to 180°. Once flipped over, the SU-8 frame keeps the two CNT-electrodes from touching each other while containing the electrolyte within the cell. Additionally, capillary forces keep the folded flap from popping back up. During the humid summer months, the electrolytes remained inside the cell without drying out for several weeks at a time. All supercapacitor devices, individually located on a 1 cm × 1 cm die, is wire-bonded to a ceramic chip holder prior to electrochemical testing.
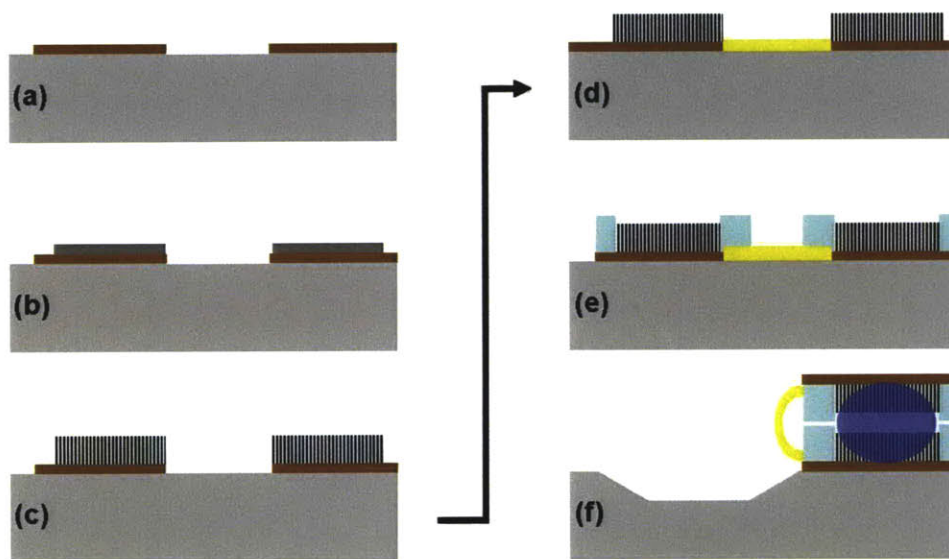
Figure 3-3: Process flow for the CNT-origami electrochemical capacitor. (a) Deposit/pattern TiN layer. (b) Deposit/pattern catalyst layer. (c) Grow CNTs. (d) Deposit/pattern Au layer through lift-off. (e) Deposit/pattern SU-8 layer. (f) Release membrane, deposit electrolyte, and fold over flap.
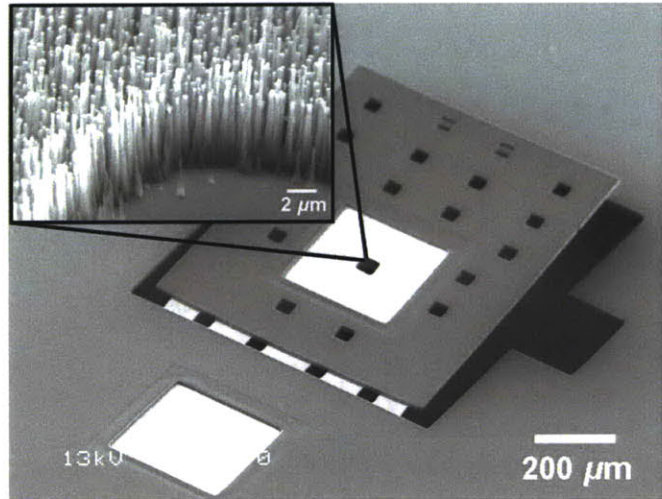
Figure 3-4: SEM image of a CNT-origami supercapacitor prior to folding. The inset shows the CNT-covered electrode surface.
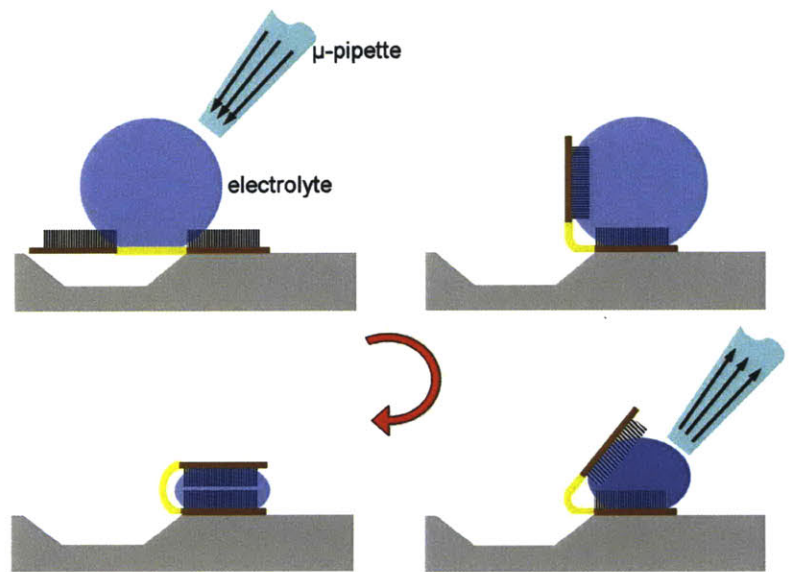
Figure 3-5: Schematic overview of the capillary force-based folding procedure.

3.1.2 Etching of CNTs

In order to fully release a supercapacitor device like the one shown in Figure 3-5, up to 30 minutes of etching in XeF_2 was initially required. Although much longer etching times were performed on previous generation supercapacitor devices without any difficulty and unwanted etching (i.e. significant etching of any material other than

68

silicon), the addition of TiN and CNTs in the current device posed a concern. As mentioned in Chapter 2, however, the thick CNT layer shielded the TiN layer from most of the XeF_2 gases. Also, initial XeF_2 tests performed on CNTs grown with the home-built machine showed no appreciable nanotube damage whatsoever. Additionally, etching of CNTs in XeF_2 has not been reported in literature.

However, long XeF_2 etching of completed supercapacitor devices with CNTs grown with the commercial machine, as seen in Figure 3-6, showed that there was clear nanotube damage that started to show after around 15 minutes of etching and continued to progress until most of the nanotubes were significantly damaged after around 23 minutes. It was quite evident that CNTs grown on the commercial machine, which were clearly of lower quality and had more visible surface defects (imperfections) compared to those grown on the home-built machine, were significantly more susceptible to XeF_2 etching. This is not surprising since XeF_2 was shown to easily etch away the excess amorphous carbon buildup on the nanotubes; a similar etching mechanism was likely in effect in the etching of the quasi-crystalline nanotubes. Although some of the variable growth parameters on the commercial machine were adjusted to improve CNT quality and thus decrease XeF_2 susceptibility, unwanted CNT etching could not be completely eliminated. In the end, the issue was resolved by decreasing the total etch time required for full device release. By reducing the number of samples put into the XeF_2 chamber at one time and increasing the number of etch holes in the device, etch times could be reduced down to less than 15 minutes.

On an interesting note, partial etching of CNTs may actually be beneficial in supercapacitor applications. Lu et al. [53] reported on the intentional plasma etching of CNTs in order to introduce further defects and open up their end tips. They showed that supercapacitors made from such plasma-etched CNTs had higher capacitances due to the increased surface area of their electrodes. Partially-etched CNTs shown in Figure 3-6(b) appear to have lost much of their catalyst tips and exhibit rougher sidewalls; total electrode surface area of future CNT-origami supercapacitors may be increased further through the partial etching of CNTs.

(a)

(b)

(c)

(d)
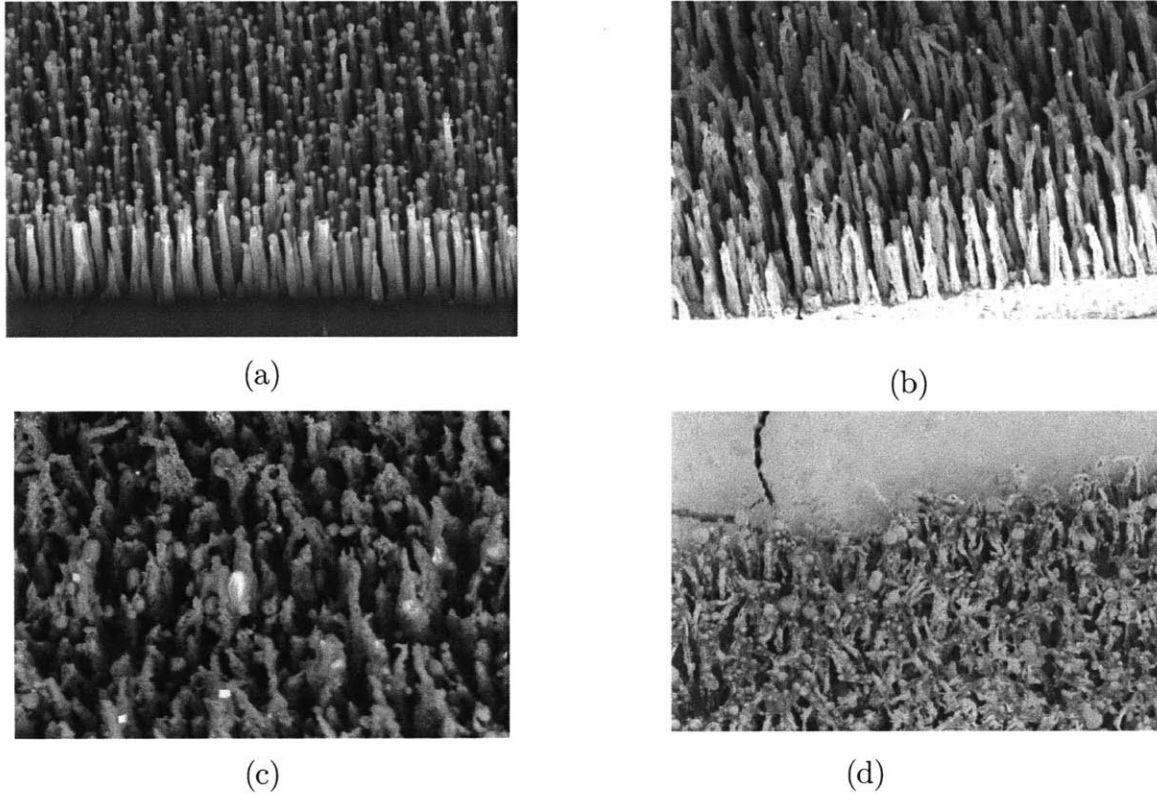
Figure 3-6: SEM images of initial supercapacitor CNTs grown on the commercial machine after (a) 12 minutes, (b) 15 minutes, (c) 18 minutes, and (d) 23 minutes of XeF_2 etching.

3.1.3 Wettability of CNTs

Since the CNT-origami supercapacitors use an aqueous electrolyte and CNTs are widely known to be inherently hydrophobic due to their perfectly crystalline sidewalls, it was not initially known whether or not the electrolyte would sufficiently wet the CNT electrodes. In fact, micropatterend areas of vertically aligned CNTs, like the ones found on the CNT-origami supercapacitor, were reported of possessing even greater hydrophobicity than the individual nanotubes [81]. However, simple wetting tests, like the one shown in Figure 3-7, showed that the electrolyte droplet quickly seeped through our nanotube forest and appeared to wet the surface quite well. Similar results, which are clearly the result of surface tension effects arising from the CNT forest's geometry, were

demonstrated by many other groups [82, 83]. Additionally, the open edge sites associated with our particular type of nanotubes (see Section 2.2.3) likely contributed to the significantly reduced hydrophobicity, if not hydrophilicity, of the individual nanotubes [84]. Even if our CNT electrodes had been hydrophobic, there are many available surface treatments for reducing hydrophobicity [85] not to mention the fact that the electric field applied as a result of our capacitor configuration would likely induce wetting of the electrode areas [86].

(a)   (b)
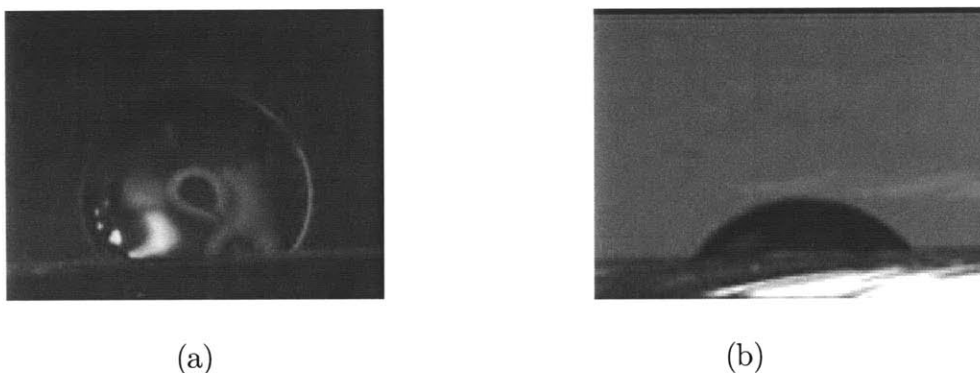
Figure 3-7: Side view of a H_2SO_4 electrolyte droplet (a) immediately and (b) a few seconds after being placed on the CNT forest. Eventually, the droplet would spread out even further and completely seep into the CNT forest.

3.1.4 Multi-layer devices

The one-flap CNT-origami supercapacitor mentioned thus far creates one active electrochemical cell with a set of electrodes. However, the origami approach allows us to continually stack our device in the third dimension to achieve increased performance without sacrificing additional areal footprint. Figure 3-8 shows a partially-folded 5-flap device that results in two active cells (the blank segments act as buffer layers between the various electrode pairs). However, the folding process for such a device is extremely difficult due to the lack of a reliable latching mechanism between the layers. Furthermore, the reduced areal footprint after stacking is negated by the fact that a deep, large silicon trench occupies the pre-fold real estate. Ongoing and future research in the areas of face-to-face latching, multiple segment/direction actuation, and substrate-saving release techniques will allow the creation of similar and even larger devices.

71
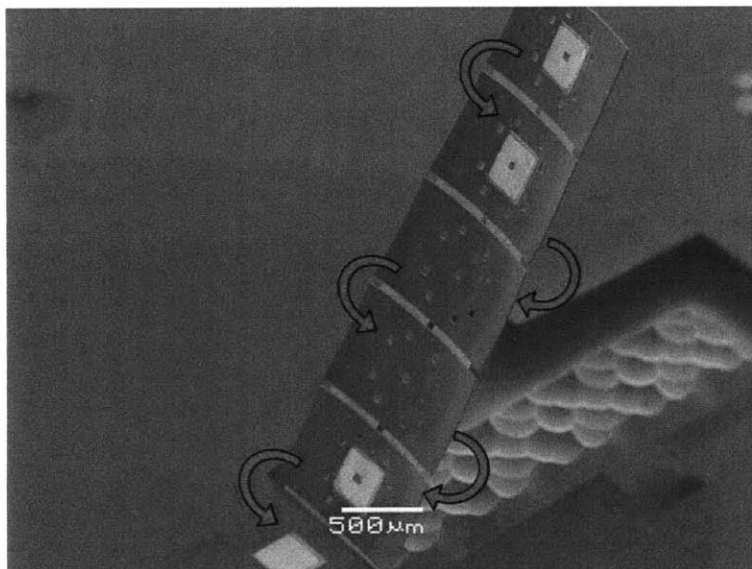
Figure 3-8: SEM image of an unfolded, multi-layer supercapacitor device with the arrows indicating the membrane folding directions.

3.2 Electrochemical testing

After several electrochemical capacitors with MWCNT electrodes were successfully fabricated, their performance was characterized through cyclic voltammetry (CV), galvanostatic charge/discharge, and electrical impedance spectroscopy (EIS). The two-electrode devices that were tested had a single electrode footprint of around 6.25×10^{-4} cm^2, which was designed to be approximately equal to that of the previously tested Super P carbon devices [10]. The two CNT electrodes with the as-measured CNT geometry and density (*diameter = 150 nm; length = 6 µm; density = 9 CNTs/µm²*) had a combined real surface area of approximately 0.015 cm^2.

3.2.1 Results and discussion

In order to accurately compare the performance of the CNT-origami supercapacitors to the previously obtained performance of the Super P carbon supercapacitors, the various

electrochemical testing parameters were kept identical to those used previously in [10]. The CV curve was generated at a voltage scan rate of 50 mV/s, and the galvanostatic charge/discharge was done under a constant current of 0.5 μA. The EIS was performed over a frequency range of 5 MHz to 100 mHz using a signal amplitude of 10 mV.

Results of the CV and galvanostatic charge/discharge tests are shown in Figures 3-9 and 3-10. Based on the equation

$$C = \frac{I}{dV/dt} , \qquad (3.1)$$

a total system capacitance of approximately 0.4 μF was obtained, which, given the slightly reduced electrode footprint of the new device due to addition of etch holes, is comparable to the value of 1.0 μF reported previously for the electrochemical capacitor based on Super P carbon black electrodes [10]. The theoretical charge storage capacity, the value referred to most often for estimating the theoretical maximum capacitance, is highly dependent on the precise electrolyte and electrode material and could not be obtained for our particular electrolyte/electrode material combination. However, Lu *et al.* [53] reported of obtaining a charge storage capacity of approximately 110 μF/cm^2 for a single-electrode supercapacitor consisting of aligned CNTs. Applying their storage capacity value to our supercapacitor results in a theoretical two-electrode capacitance of 0.4125 μF, which is very close to our measured capacitance of 0.4 μF.
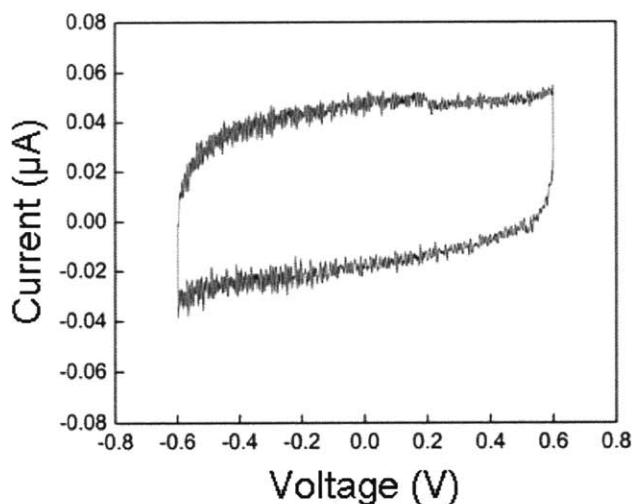
Figure 3-9: Cyclic voltammogram results for the CNT-origami supercapacitor measured at a scan rate of 50 mV/s.
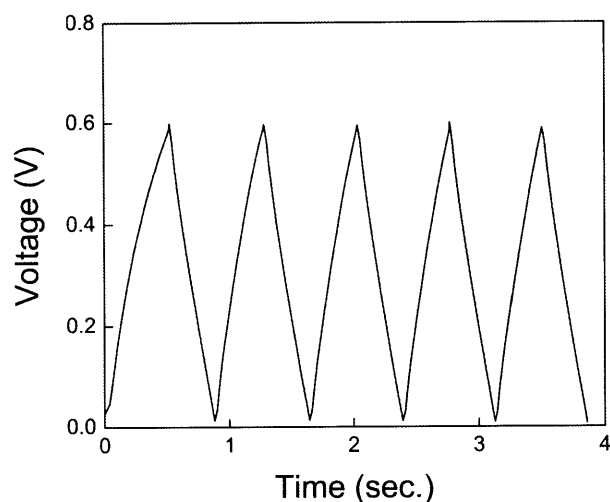
Figure 3-10: Galvanostatic charge/discharge profile for the CNT-origami supercapacitor recorded at ±0.5 μA.

Figure 3-11 shows the results of EIS measurements, which also indicates a total capacitance of approximately 0.4 μF as shown through earlier tests. The overall shape of the Nyquist plot shown in Figure 3-11 *(a)*, which consists of a small semi-circle followed by a 45η Warburg impedance region at higher frequencies and a steep, almost vertical region at lower frequencies, is consistent with those found in literature for similar, albeit much larger, devices [87-89]. The Nyquist plot indicates an almost purely capacitive behavior at low frequencies and shows the frequency dependence of the ion diffusion and transport process at high frequencies. Furthermore, the relatively constant slope in the *log |Z| vs log Frequency* plot shown in Figure 3-11(b) points to reasonably consistent performance throughout the frequency spectrum. The equivalent series resistance (ESR), as determined from the Z'-intercept on the Nyquist plot, was approximately 20 Ω. The significance of this ESR value will be discussed in the following section.

74
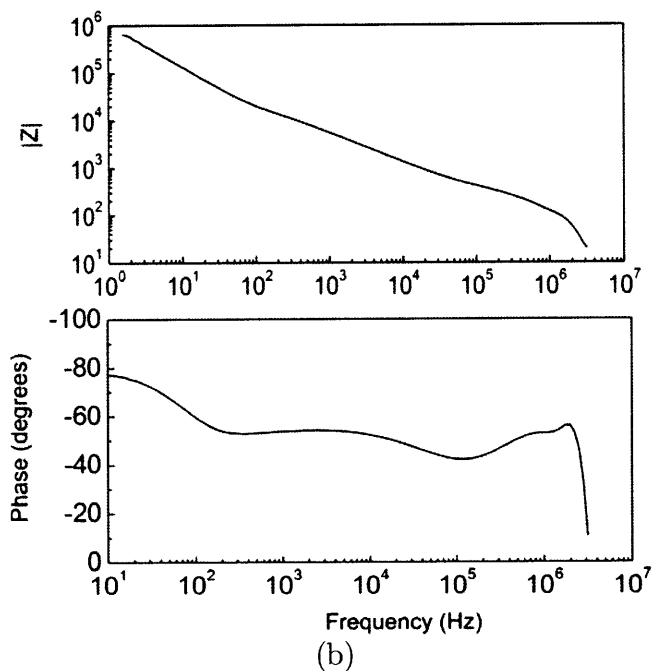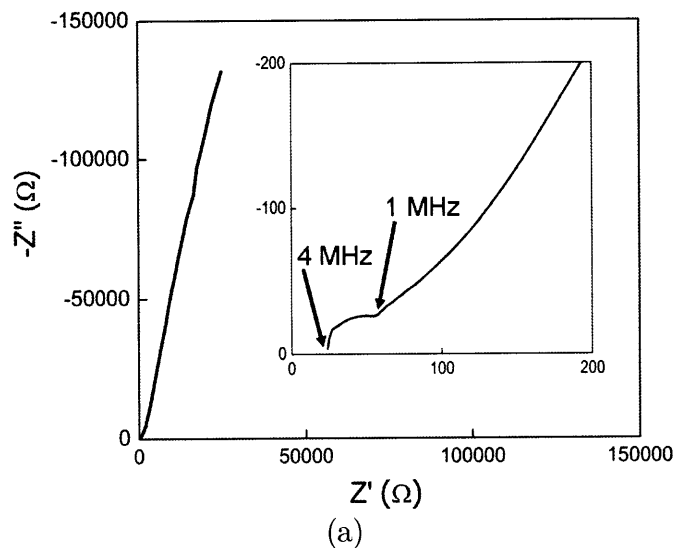
Figure 3-11: (a) Nyquist and (b) Bode plots of the EIS results shown for frequencies between 4 MHz and 4Hz.

3.2.2 Comparison to carbon and other CNT electrodes

As mentioned in Section 3.2.1, the CNT-origami supercapacitors exhibited a measured capacitance of 0.4 μF compared to 1.0 μF of the Super P carbon device. In order to get a better sense of how these two values compare, several commonly used measurements

for specific capacitances, for both devices, are summarized in Table 3-1.

The two types of supercapacitors show comparable values with subtle differences. The CNT-based supercapacitor shows a slightly higher capacitance per surface area of electrode material since most of the CNT-electrode surface should be accessible for the ions; in the Super P device, some parts of the electrode surface is inaccessible due to the presence of small nanopores (similar to the case shown in Figure 3-2). For capacitance per volume and per mass of electrode material, however, the CNT-based supercapacitor exhibits slightly lower values. This is most likely because only the outer most surfaces of the CNTs, which were quite thick with a less than optimal surface-area-to-volume ratio, contribute to charge storage. Modifying the CNT geometry, namely making it thinner, should increase this value. Capacitance per mass is used predominantly as a measuring standard in many supercapacitor applications because electrode materials can be quite costly and comprise bulk of the manufacturing costs; however, it is not as important in our devices since the electrode materials are directly grown on the supercapacitor and do not represent a huge cost. Capacitance per areal footprint, or in other words on-chip area, might be a better measure of value and efficiency for the CNT-origami superca-pacitors. The measured capacitance per on-chip area for our device compares favorably to other published values as indicated in Table 3-2. This value is even more impressive since the CNTs used in our study were only around ~7 μm in length.

Table 3-1: Performance metrics for Super P carbon and CNT-based electrochemical capacitors. All values shown are for the entire two-electrode system (*Mass density of MWCNTs was taken to be 0.6 - 2 g/cm^3 [90, 91]).

Specific Capacitance	Super P Carbon	CNT-origami
μF/cm^2 (on-chip area)	816	640
μF/cm^2 (theoretical surface area)	13	27
μF/cm^3 (theoretical volume)	8.2×10^{-1}	4.0×10^{-1}
F/g (theoretical mass)	4	2~7*

Table 3-2: Specific capacitances (in $\mu F/cm^2$) for various supercapacitor devices with electrodes based on MWCNTs.

CNT-based Supercapacitor	Specific Capacitance	CNT length
CNT-origami	640 $\mu F/cm^2$	~7 μm
Interdigitated CNT [57]	428 $\mu F/cm^2$	~80 μm
Electrophoretic deposition [92]	93 $\mu F/cm^2$	~7 μm

Table 3-3 compares the capacitance per mass (F/g) of our devices to some of the most promising works found in literature with the highest reported performances for CNT-based supercapacitors. Although it appears that our performance based on this specific metric seems significantly small compared to other published values, it should be noted that the total capacitance of an electrochemical double layer capacitor, like in our device, is given by the equation

$$\frac{1}{C_{dl,total}} = \frac{1}{C_{dl,1}} + \frac{1}{C_{dl,2}}$$

(3.2)

since there are effectively two capacitors connected in series through the electrolyte. Therefore, a real-world, two-cell setup like the one found in our device exhibits half the capacitance of the individual electrodes. However, most published performance figures for supercapacitors are for a three-cell testing setup with a single working electrode, which actually exhibits twice the capacitance of a two-cell setup while only possessing half the electrode material; specific capacitances values obtained in this way are thus typically four times greater than those of our two-cell device. Additionally, all of the devices shown in Table 3-3 are based on SWCNTs with diameters well over a order of magnitude smaller than our MWCNTs. Because thinner CNTs have a much more favorable surface-area-to-volume ratio, the capacitance per mass value naturally suffers. However, these values suggest that the CNT-origami supercapacitor, with better optimized CNT geometries, will be able to obtain significantly higher performance. Lastly, it should be mentioned that only the CNT-origami supercapacitor is designed for and fully compatible with other microfabrication platforms.

Table 3-3: Specific capacitances (in F/g) for various CNT-based supercapacitors.

CNT-based Supercapacitor	Specific Capacitance
CNT-origami	2~7 F/g
Densely packed CNT [93]	20 F/g
Sprayed on CNT film [94]	90~120 F/g
Layer-by-layer assembly [95]	159 ± 10 F/g

Another comparison of the CNT and Super P supercapacitors can made with regards to their frequency-dependent behaviors. Figures 3-12 and 3-13 show previously obtained EIS results for the Super P carbon electrodes and plain gold electrodes, respectively. As expected, the plots in Figure 3-13 show an almost purely capacitive behavior at all frequencies since the gold electrode is smooth and flat with no porous structure for the ions to migrate through. The trade-off, of course, is the greatly reduced total capacitance. The plots in Figure 3-12 are also as expected and typical of supercapacitors with highly porous electrode materials. Comparing the *log* $|Z|$ *vs log Frequency* plot of the Super P and gold devices to that of the CNT device shown in Figure 3-11(a) reveals that the CNT-origami supercapacitors behave very similarly to an ideal capacitor for frequencies below 1MHz. Although this benefit is not hugely important in energy storage schemes, it could be important in certain high-frequency applications.

Finally, the ESR of the CNT-origami supercapacitor was around 20 Ω as determined by the Z'-intercept on the Nyquist plot whereas it was approximately 17 Ω for the previously tested Super P carbon device. Typically, lower ESR values are desirable since that translates into higher power densities. The total impedance of our supercapacitor system can be approximately described by the equation

$$Z = R + \frac{-j}{\omega C} \tag{3.3}$$

where R is the total internal resistance of the system, ω is the angular frequency, and C is the total capacitance. At very high frequencies, the capacitance term disappears, and the supercapacitor basically behaves as a resistor with resistance indicated by the ESR. While the CNT device, compared to the Super P device, was expected to exhibit lower

electrolyte and electrode resistance due to its perfectly aligned and completely connected electrode network, we also expected increased internal resistance from the use of a TiN current collector, whose electrical resistivity is approximately 60 times higher compared to the previous device's gold current collector. We believe that the two factors offset each other resulting in approximately equal final ESR values. The ESR values are well within reasonable limits, especially considering that we have a completely self-contained and fully wire-bonded package with micropatterend wiring.
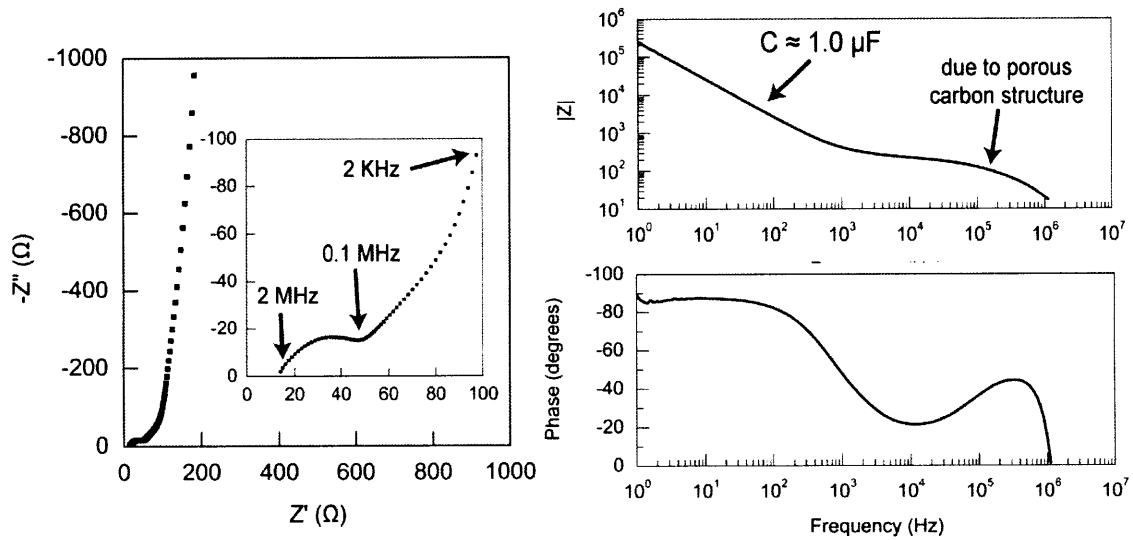
Figure 3-12: EIS results for a supercapacitor with Super P carbon electrodes [13].
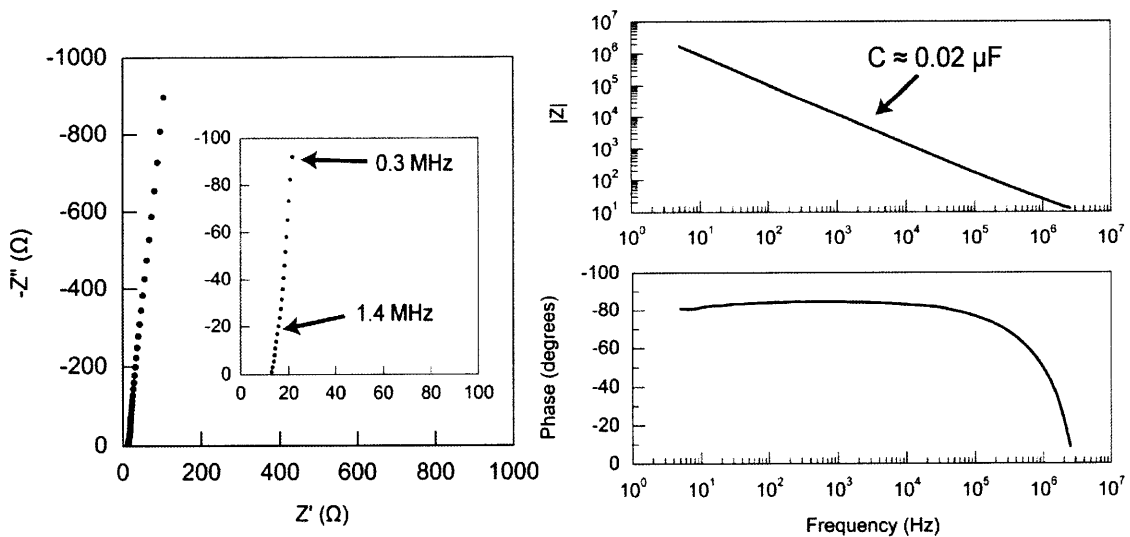
Figure 3-13: EIS results for a supercapacitor with plain gold electrodes [13].

3.3   Summary of CNT supercapacitor

In summarizing, we have shown that a microscale electrochemical capacitor with vertically-aligned MWCNT electrodes can be made based on the origami process. Unlike the previous generation origami supercapacitor that included a manual, time-intensive electrode deposition step, the CNT-origami supercapacitor was created entirely using commercially available fabrication equipment. It was further shown that the CNT-origami supercapacitors exhibit electrochemical performance that is comparable to those of full-sized devices while exhibiting more favorable high-frequency behaviors compared to non-CNT origami devices.

The CNT-origami supercapacitor will be able to serve as an integrated, on-chip power source for various micro/nano-systems applications. We expect further performance improvements will result from optimizations of CNT geometry and density.

Chapter 4

Membrane manipulation using magnetic carbon nanotubes

In addition to their unique electrical, mechanical, and optical properties, carbon nanotubes additionally possess highly interesting magnetic properties. Such magnetic properties of CNTs have been studied extensively and utilized in nanotube alignment [96, 97] and self-assembly [43, 98], magnetic force microscopy [99, 100], recording [101, 102], gas sensing [101, 103], and even gene delivery [104] applications. Furthermore, the inherent magnetic properties of CNTs can be enhanced significantly by coating [98, 99] or filling the nanotubes with ferromagnetic materials such as Ni [102,103], Co [103, 104], and Fe [108, 109]. Filling of nanotubes with ferromagnetic materials is especially attractive because the vertically elongated shape of the encapsulated particles leads to a large perpendicular coercivity [109] while the carbon coating protects the particles from oxidation [32, 110] and mechanical abrasion [110]. While several methods [105, 108, 111, 112] have been developed for intentionally encapsulating metals inside CNTs, nanotubes grown via the PECVD method exhibit tip-growth behavior (see Figure 1-2) and thus naturally contain teardrop-shaped, carbon-encapsulated catalyst particles at the tips without the need for additional processing steps [32, 104, 109]. Furthermore, it turns out that such encapsulated particles are ferromagnetic since Ni, Co, and Fe are almost always used as CNT growth catalysts, as in our case, due to their highest demonstrated level of catalytic activity [113]. There is some interesting recent work involving the use

of non-ferromagnetic materials for CNT growth, but such growth is still extremely rare and difficult to achieve [114-116].

For the origami devices, the natural occurrence of tip-embedded nanomagnets in the CNTs is another facet of CNT-integration that can be taken advantage of for increased functionality. This chapter will elucidate the properties of such encapsulated nanomagnets and explore their usefulness in origami applications.

4.1 Magnetic properties of CNTs

The magnetic properties of our PECVD-grown CNTs, or more specifically that of the nanoparticles encapsulated inside them, warrant further investigation. While magnetic properties of bulk Ni and Co, the two materials used for CNT growth in our case, are well known, the properties of the embedded nanoscale particles, especially after undergoing CNT growth, is unclear. While the magnetic properties of ferromagnetic materials intentionally encapsulated within nanotube walls have been have been investigated, the magnetic properties of naturally occurring catalyst particles inside CNT tips have never been, to the best of our knowledge, been characterized in detail.

An example of a CNT grown in our facilities is shown in Figure 4-1(a). The upside-down teardrop shape of the embedded Ni catalyst is plainly visible. Additionally, Figure 4-1(b) clearly shows the thin layer of carbon coating around the Ni particle that keeps it from oxidizing and losing its magnetic properties. The results of energy dispersive x-ray (EDX) analysis performed on old (> 1 month) CNT tips, shown in Figure 4-2, also indicate the absence of oxygen, further suggesting that the otherwise expected Ni oxidation has not taken place due to the thin carbon coating around the nanoparticle. Oxidation and other material changes of the ferromagnetic catalyst tips should also be revealed in subsequent magnetic characterizations.
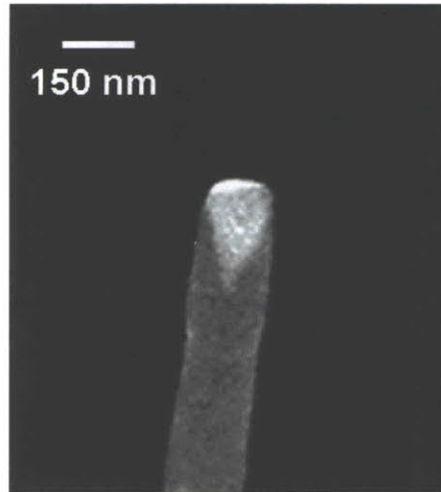
(a)
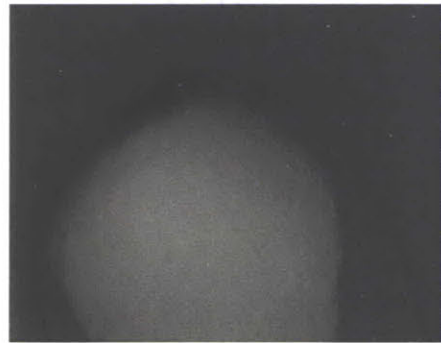
(b)

Figure 4-1: Closeup SEM and TEM images, respectively, of a PECVD-grown CNT showing (a) the teardrop-shaped Ni catalyst particle embedded in the tip and (b) the carbon coating surrounding the catalyst.
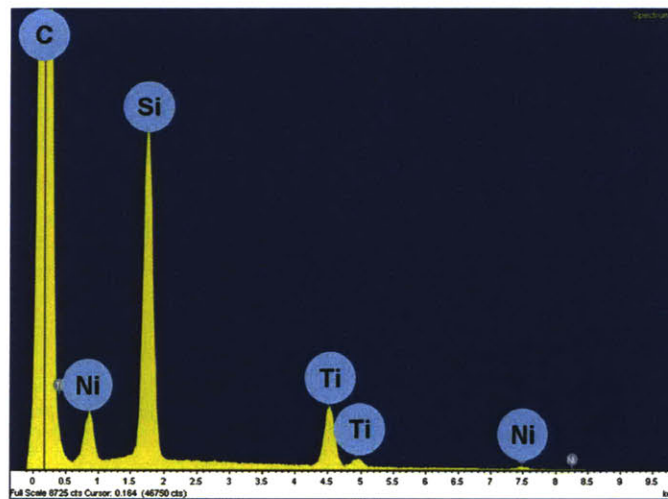
Figure 4-2: Results of EDX analysis of the CNT's tip region.

4.1.1 Magnetic measurements

A vibrating sample magnetometer (VSM) was used to measure the saturation magnetizations and coercivities of the Ni and Co nanoparticles embedded in the CNTs. Since individual nanotubes cannot be measured with this technique, a well-characterized forest of CNTs was used in the analysis.

On average, the Ni-filled CNTs tested were approximately 5 μm in length and 160 nm in diameter ($\sigma \approx 14$ nm). The teardrop-shaped Ni particle encapsulated at the tip of each CNT, shown in Figure 4-1(a), was approximately 160 nm wide and 220 nm long. The approximate CNT density was 5 nanotubes per μm^2. The various nanotube measurements were taken by analyzing top-down, side, and isometric views of the CNTs under an SEM. A sample top-down image is shown in Figure 4-3; the diameters and densities of the CNTs can be clearly seen. Due to their highly consistent growth and excellent CNT uniformity, as explained further in Section 2.2.1, Ni-filled CNTs were used predominantly throughout the study although Co-filled CNTs were also grown and studied. Figure 4-4 shows the typical Ni and Co-filled CNT that were used for the magnetic tests.
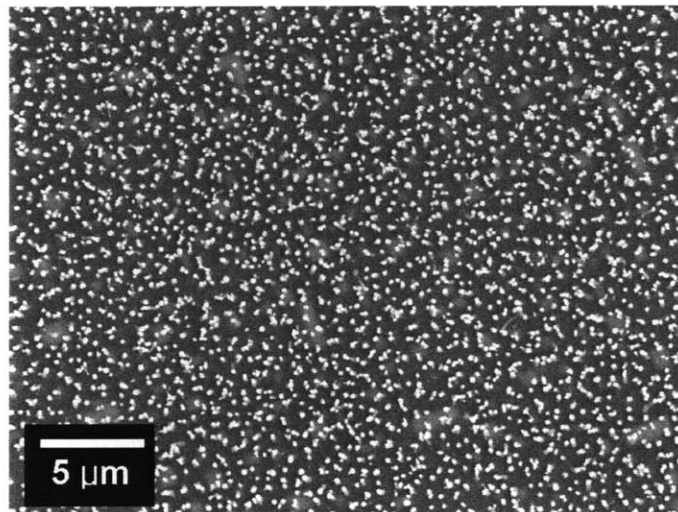
Figure 4-3: Top-down view of a CNT forest. Each bright spot corresponds to one nanotube.
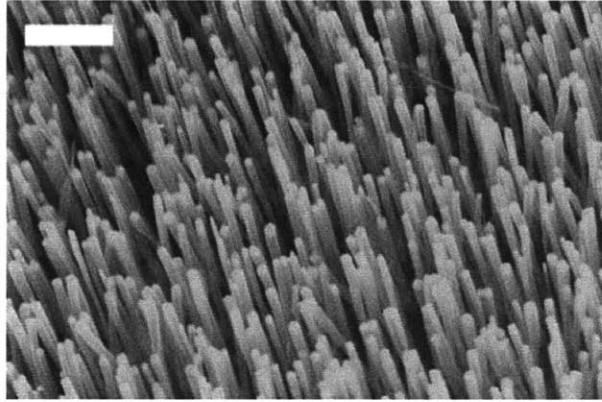
(a)
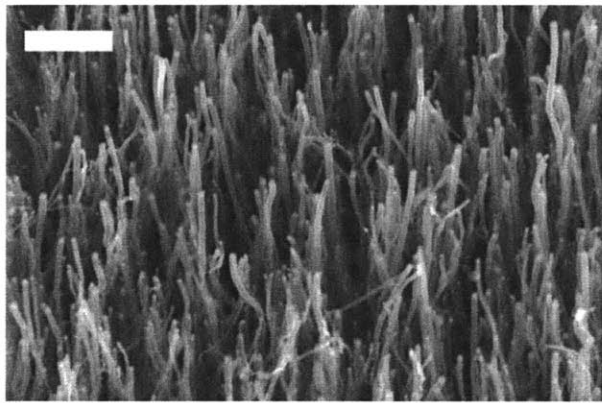
(b)

Figure 4-4: Typical (a) Ni-filled and (b) Co-filled CNTs used for magnetic testing (bar = 2 μm)

Figure 4-5 shows the resulting magnetic hysteresis loops of 5mm Ł 5mm arrays of vertically aligned CNTs grown from Ni and Co catalysts as obtained from VSM analysis. Based on the nanoparticle dimensions and nanotube density mentioned above, the encapsulated Ni nanoparticles were found to have a saturation magnetization, M_{s_Ni}, of approximately 0.477×10^6 A m^{-1}, which is very close to the theoretical value of 0.48 Ł 10^6 A m^{-1}. Similarly, saturation magnetization of the Co nanoparticles, M_{s_Co}, was found to be around 1.21×10^6 A m^{-1}, which is slightly smaller than the theoretical value of 1.42 $\times 10^6$ A m^{-1}. The discrepancy, however, can be accounted for by the difficulty in accurately approximating the total nanoparticle volume of the rather nonuniform Co CNTs (see Figure 4-4). The hysteresis loops also show the in-plane/perpendicular coercivities of Ni and Co nanoparticles to be around 100 Oe/180 Oe for Ni and 300 Oe/600 Oe for

Co, respectively, where the perpendicular direction is in-line with the nanotube axis. The measured coercivity values are in excellent agreement with those found in literature for similar configurations [101, 105, 109]. While magnetocrystalline anisotropy could also have an effect if the particles turned out to be single crystalline, consistently higher coercivities in the axial direction of the nanotubes for both Ni and Co nanoparticles suggest that the displayed perpendicular magnetic anisotropy is caused solely by the anisotropic shape of the encapsulated nanoparticles.
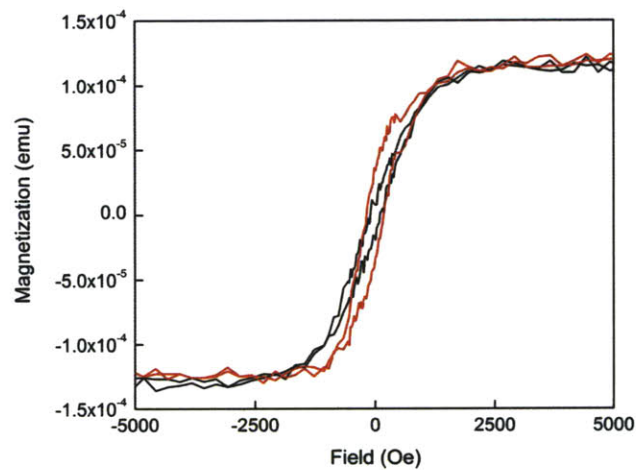
(a)
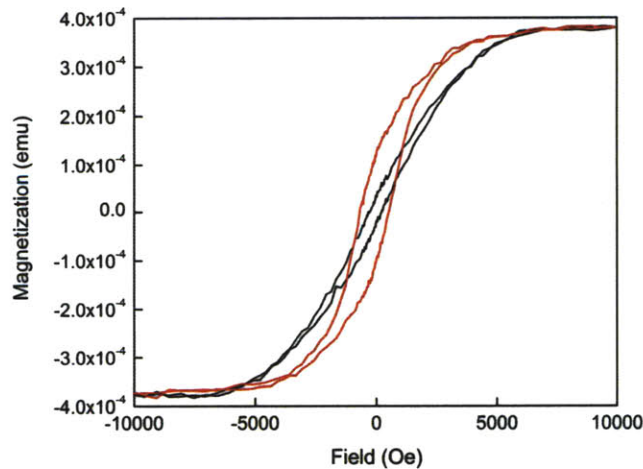
(b)

Figure 4-5: Magnetic hysteresis loops for (a) Ni and (b) Co as obtained through VSM analysis. Red lines correspond to perpendicular (to the substrate) magnetization while the black lines correspond to magnetization in the in-plane direction.

4.1.2 Origami applications

The ferromagnetic properties of CNT-encapsulated catalyst particles can be utilized by origami devices in one of two ways. First, the origami fabrication method can be used to create CNT-integrated devices intended for applications that require magnetic CNTs, for example, magnetic force microscopy [99, 100]. The other approach, and the one that will be investigated further in this chapter, is to use the newly acquired magnetic properties of the CNTs to aid in the overall origami fabrication and assembly scheme. A combination of the two methods, in which magnetic CNTs serve to both aid in the origami process as well as add magnetic functionality to the final device, is another possible option for future exploration.

The work by Nichol *et al.* involving the use of nanopatterned magnets on the surface of origami membranes [14, 117], outlined in Figure 4-6, reveals how magnetic CNTs may be used to assist in origami fabrication. Figures 3-6(b) shows how a rotating external magnetic field magnetizes the nanomagnets and creates magnetic torque that in turn causes the entire membrane segment to actuate and fold. Figure 4-6(c) shows how the magnetic attraction force between corresponding nanomagnets can cause the two opposing membranes to attach to each other once they are sufficiently close. In similar fashion, origami membranes covered with vertically-aligned, nanomagnet-embedded CNTs should also exhibit rotation and latching action as shown in Figure 4-7. The remainder of this chapter will be devoted to these two anticipated behaviors.
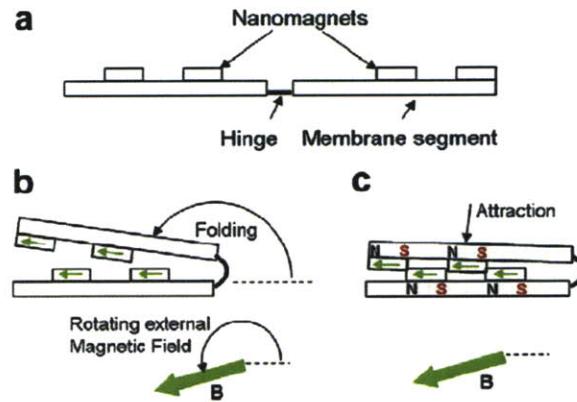
Figure 4-6: Magnetic actuation and attachment method based on the use of (a) patterned nanomagnets on a folding membrane segment. (b) A rotating external magnetic field magnetizes the nanomagnets and cause them, and in turn the membrane, to rotate. (c) Once the opposing nanomagnets are sufficiently close to each other, magnetic attraction forces cause the two membranes to attach to each other [117].
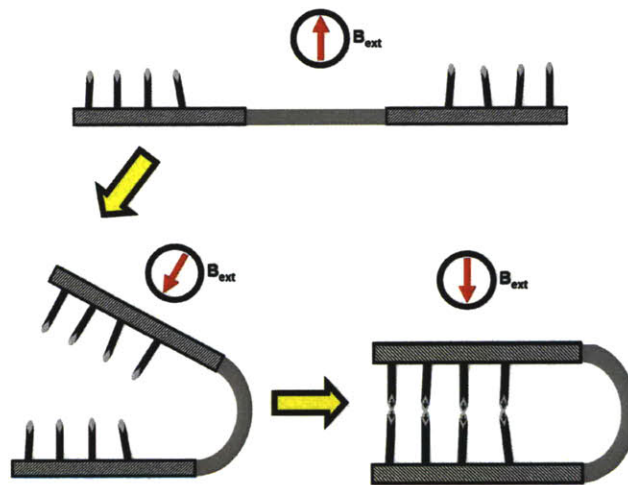
Figure 4-7: Membrane rotation and latching concept using arrays of vertically-aligned CNTs with nanomagnet tips.

4.2   Membrane rotation

Controlled rotation or folding of origami membranes is crucial for assembly purposes as well as in dynamic applications where the membranes must actuate back and forth between predetermined positions. For origami assembly, which we are most interested

in, the membrane must controllably rotate up to 180° from the initial horizontal state (downward rotation of up to -180° would also be possible if enough substrate material has been removed to allow the membrane segment to rotate in that direction). Compared to alternative methods of origami actuation, the CNT-based rotation is particularly attractive because it uses CNTs that are already present on the membrane and thus requires no further addition of actuation mechanisms on the device itself.

4.2.1   Design and fabrication

Following the general fabrication scheme described in Chapter 2, a simple test device was made to verify and quantify the magnetic rotation abilities of our CNT arrays. The device consisted of a rectangular CNT-covered TiN stage connected on either side by long, flexible torsional hinges. To simplify the fabrication process, the stage and hinge structures were patterned on a single TiN layer and thus had the same thickness. The fabrication process is outlined in Figure 4-8. Once the TiN stage and hinges have been released from the silicon substrate, the entire assembly is free to rotate out of plane. The detailed recipe for this process can be found in Appendix A.3.

Several variations of the test device, some of which are shown in Figure 4-9, were successfully fabricated and released. The design variations included etch hole size/density, hinge type (serpentine vs. bar), hinge length, and stage size (i.e. number of CNTs). The design shown in Figure 4-9(d) was ultimately chosen because it released very rapidly due to its many etch holes (~2 minutes of XeF_2 etching), exhibited greater magnetic torque due to its larger stage size, and remained tight and freely suspended after release. The other designs, many of which offered even greater torsional flexibility, tended to sag and stick to the bottom surface making it difficult to later rotate out of plane.

The device shown in Figure 4-9(d) consists of a TiN stage that measures 100 μm × 200 μm and two torsional hinges each of which measures 5 μm × 450 μm. Both structures are 100 nm thick, and the Young's modulus of TiN is taken to be around 600 GPa [62]. The torsional hinges were designed to provide minimal and uniform torsional stiffness throughout the intended range of motion and at the given dimensions provide a combined torsional stiffness S of around 3.06×10^{-14} N·m [118]. The maximum principal

strain of the hinge structures were estimated to be around 0.00016% based on finite element analysis using ABAQUS. With such a small strain value, the hinges are assumed to behave linearly throughout its intended range of motion (0° -180°).
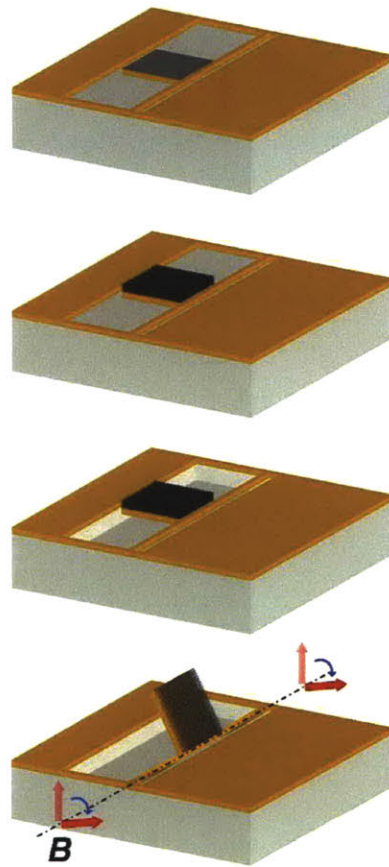
Figure 4-8: Fabrication process for the magnetic testing device. A TiN is layer is patterned to create the rotating stage and supporting torsional hinges, CNTs are grown on the stage, and entire structure is released through XeF₂ etching.

(a)

(b)

(c)

(d)

bar = 100μm
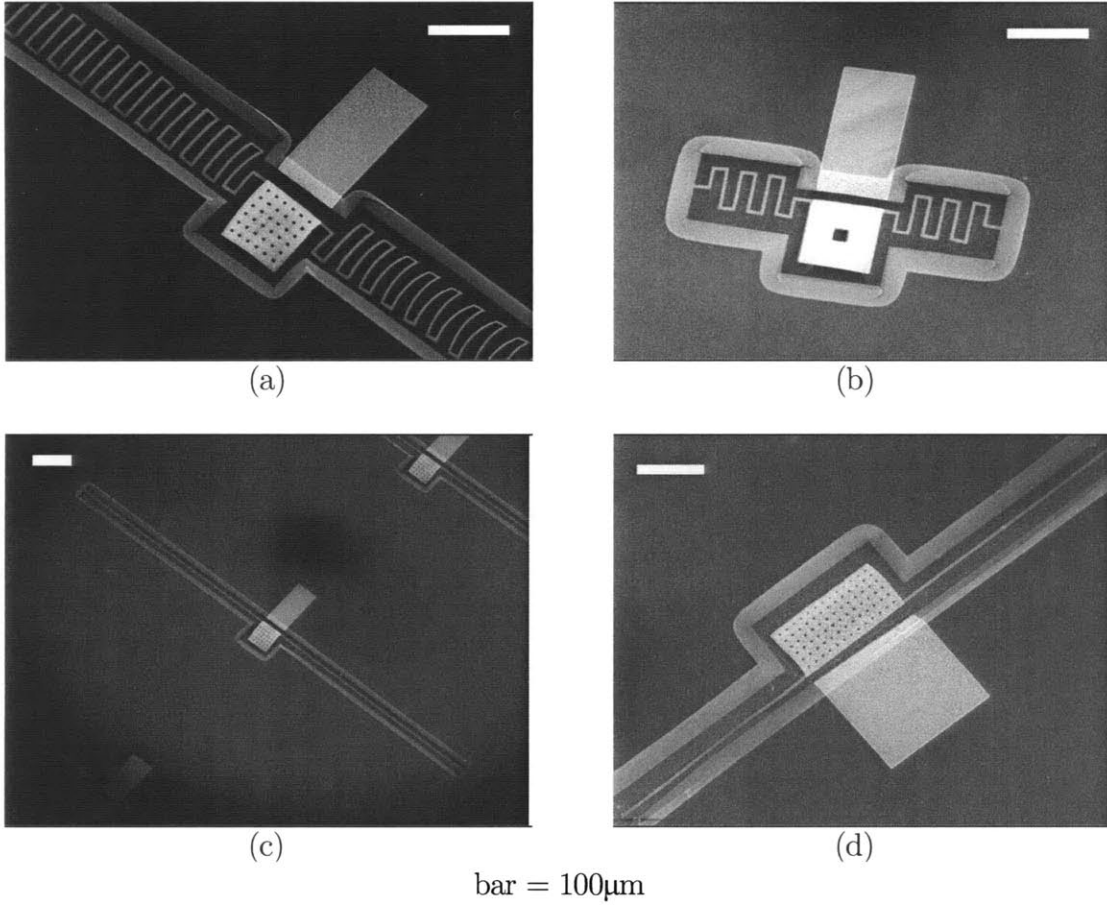
Figure 4-9: (a-d) various designs considered for magnetic testing. The design shown in (d) was chosen and used throughout all magnetic actuation tests. The long rectangular patch of CNTs on the fixed substrate is for membrane latching tests that will be discussed in Section 4.3.

4.2.2   Theory and simulation

Magnetic torque is generated when, in the presence of an external magnetic field, the magnetization directions of the nanoparticles inside the CNT tips are oriented at an angle Θ with respect to the direction of the external field. The torque generated, T_m, is given by the familiar equation

$$T_m = m \times B, \tag{4.1}$$

91

where m is the magnetic moment associated with the nanoparticle and B is the intensity of the external magnetic field. If the nanoparticles within the CNTs were perfectly spherical, they would magnetize in a direction parallel to the external field; no magnetic torque would be generated and thus the origami membrane will not actuate. However, this is not the case as our encapsulated nanoparticles possess a pointed, elongated shape that results in increased magnetic anisotropy in the axial direction (see Figure 4-5); in other words, they possess an axial magnetization preference and consequently generate varying magnetic torque upon rotation of the external field.

For long slender nanomagnets, like the ones used by Nichol *et al.* [14, 117], magnetic torque generated under a rotating external field could be estimated by replacing the nanomagnet with an ideal magnetic dipole, where the dipole moment of such an arrangement can be expressed as

$$m = pl, \tag{4.2}$$

with p being the strength of the magnetic poles separated by a distance l. By combining Equation 4.1 with Equation 4.2 and using the relationship $p = \pm \mu_o^{-1} M_s A$, where A is the cross sectional area of the nanomagnet and μ_o is the magnetic permeability of free space, the magnetic torque per nanomagnet can be written as

$$T_m = \frac{BM_sV}{\mu_0}\sin(\theta), \tag{4.3}$$

where V is the volume of each nanomagnet. This generalization is possible for the most part because the long and thin shape of the nanomagnets forces them to maintain a perfect axial magnetization regardless of the external field angle.

While the dipole approximation works relatively well in circumstances just described, the complex teardrop shape of the CNT-encapsulated nanoparticles requires a different approach. This is due to the fact that most of the encapsulated nanoparticle is comprised of spherical "nonmagnetic" volume that contributes little to the overall magnetic torque. In order to obtain a more accurate angular dependence of T_m for the teardrop

shaped nanoparticles, Object-Oriented Micromagnetic Framework (OOMMF) [119]
software was used to simulate the effects of a rotating magnetic field.

For the OOMMF simulations, a fully three-dimensional model of the teardrop shape
was built in AutoCAD and converted into compilable format by dividing into 35 two-
dimensional slices stacked on top of one another as shown in Figure 4-10. In the simula-
tions, a magnetic field rotating from 0° to 180° (around the torsional hinge axis shown
in Figure 4-8) and ranging in intensity from 0.1 T to 0.22 T was applied to the tear-
drop-shaped nanoparticle, which were modeled as either solid Ni or Co.

Figure 4-10: Two-dimensional slices of the 3-D teardrop model used in OOMMF
simulations.

Figure 4-11 shows the OOMMF simulation results for magnetic torque generated per
nanotube as a function of the external field angle (intensity set at 0.2 T). The red
(circle) dots correspond to the Ni nanoparticles while the black (square) dots correspond
to the Co nanoparticles. Since magnetic torque is proportional to the saturation mag-
netization of the material as indicated by Equation 4.3, the torque values for Co
nanoparticles are shown to be approximately three times greater than those of the Ni
nanoparticles as expected ($M_{s\_Ni} = 0.48 \times 10^6$ A m^{-1} compared to $M_{s\_Co} = 1.42 \times 10^6$ A
m^{-1}). Total magnetic torque generated by all the CNTs on the origami membrane is
shown in Figure 4-12 where the horizontal blue line indicates the maximum torque
required to completely flip over the stage (i.e. rotate 180°). With the given stage/hinge
dimensions and CNT size/density, the figure indicates that only membranes covered
with Co-filled CNTs, and not Ni-filled CNTs, will be able to rotate all the way to 180°.
Figure 4-13 shows the OOMMF results for a full 180° field rotation at varying intensi-
ties (0.1 T to 0.22T) for the Ni nanoparticle. The plots show an almost linear relation-
ship between torque and angle of applied magnetic field at all intensities up to about
65ŋ, after which the generated torque starts to decrease sharply and eventually reverses

directions at 90°. This means that maximum magnetic torque will be obtained when the external magnetic field is rotated approximately 65° with respect to the nanotube axis.

For comparison purposes, the green (triangle) dots in Figure 4-11, plotted using Equation 4.3, show what the magnetic torque would be if the Ni nanoparticles were replaced with equivalent magnetic dipoles. The results could also be interpreted as what would happen if the nanoparticles maintained their initial magnetization in the axial direction regardless of the external field angle. Compared to the OOMMF results for Ni, the dipole approximation model results in magnetic torque that is approximately an order of magnitude higher. This, again, can be explained by the "nonmagnetic" volume of the spherical section of the teardrop. A slice of the OOMMF-simulated teardrop is shown in Figure 4-14 for the instance when a external magnetic field B of 0.2 T is applied at an angle Θ of 45°. The region to the left, which corresponds to the spherical section of the teardrop, shows uniform magnetization in the direction of the external field; thus no torque is generated in this region. The pointed region to the right, however, remains magnetized mostly in the axial direction due to shape anisotropy; the generated magnetic torque comes only from this region.
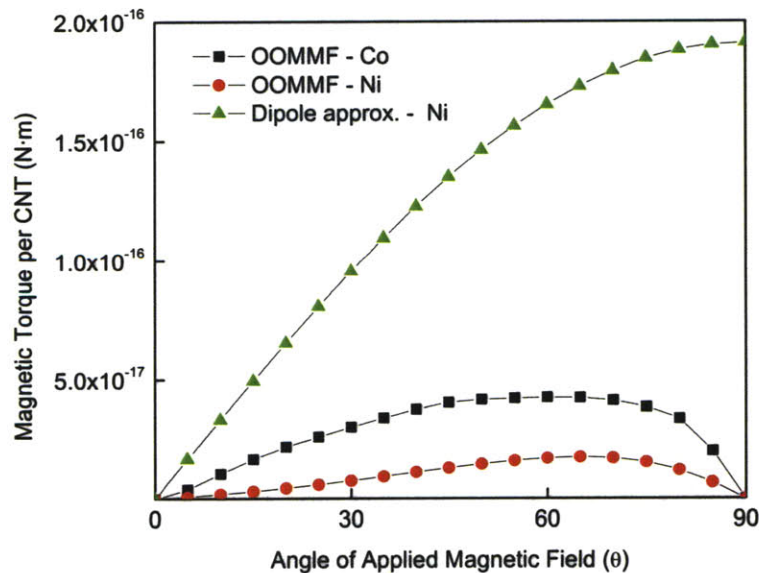
Figure 4-11: Simulation and dipole approximation results of magnetic torque generated in one CNT as a function of magnetic field angle.
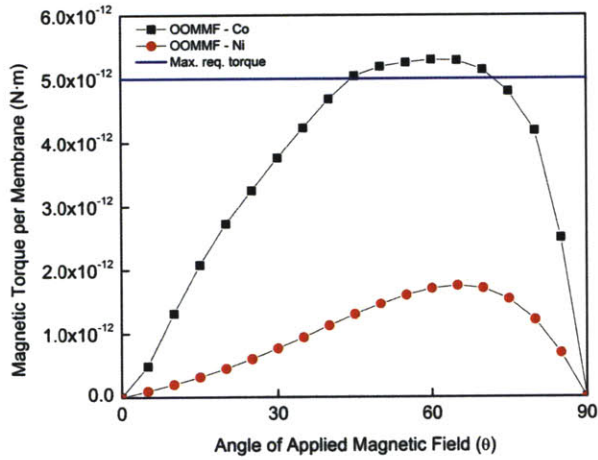
Figure 4-12: Simulation results of magnetic torque generated by the entire CNT-covered membrane as a function of field angle in comparison to the maximum torque required to fully rotate the stage by 180°.
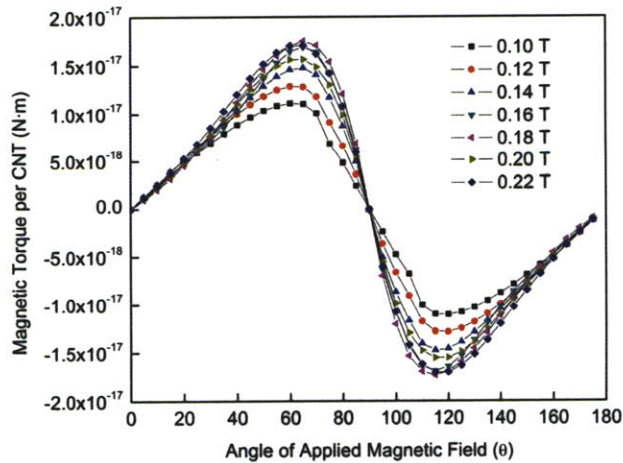
Figure 4-13: Simulation results of magnetic torque generated per CNT as a function of field angle of varying intensities.
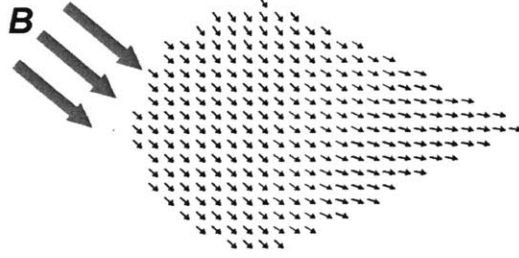
Figure 4-14: Slice of the OOMMF-generated teardrop model showing internal magnetization when an external field of B = 0.2T is applied at 45° with respect to the CNT axis.

4.2.3 Experimental results

A simple test setup was created to verify the OOMMF findings. First, a released magnetic CNT test device was placed horizontally under a microscope equipped with a high-resolution digital camera. Next, a SmCo cube magnet (2cm × 2cm × 2cm) was attached to a rotating shaft and placed next to the CNT sample. The shaft's axis was in-line with the torsional hinge axis, and the two poles of the magnet were initially parallel with the nanotube axis. At the external magnetic field angle of $\Theta_B = 0°$, in other words when the magnetic field lines going through the sample were parallel to the CNTs, the magnetic field intensity at the center of the CNT device was measured with a handheld magnetometer to be around 0.2 T ± 10%. At this point, the magnet was slowly rotated in 10° increments, and a top-down image of the device was taken at each interval. From such images, the rotation angle Θ_C of the CNT stage could be easily estimated through simple trigonometry. The angle of applied magnetic field, Θ_B, and the CNT state rotation angle, Θ_C, are shown in Figure 4-15. A more precise angle measurement system based on laser beam deflection may be used in the future, but the current design in which the entire surface of the rotating stage is completely covered by the CNT array, known to have an extremely high optical absorption [120], made such a setup impractical. Figure 4-16 shows three images of the device taken at $\Theta_B = 10°$, 90°, and 130°, respectively. As seen in the images, the CNT stage rotation angle Θ_C lags behind the magnet rotation angle Θ_B, and this difference continues to increase as the external magnet is rotated further.

96

In Figure 4-17, the stage rotation angle is plotted as a function of the applied magnetic field angle for both OOMMF (red line) and experimental (black line) results. As expected for the Ni-filled CNTs based on Figure 4-13, the OOMMF-projected stage rotation angle reaches the maximum of around 55° when Θ_B - Θ_C, or the angle of the external magnetic field with respect to the nanotube axis, is approximately 65°. While the experimental results are quite similar to the simulation results, the maximum stage rotation angle of 65° is instead achieved when Θ_B - Θ_C is around 75°. This small discrepancy, however, is sufficiently accounted for by uncertainties in the estimation of CNT size, number, and uniformity as well as variations in CNT orientation.

Upon further magnetic rotation beyond this angle, the stage quickly snapped back to its original state, as expected, since the nanoparticle magnetization is reversed. Similar testing was performed for the Co-filled CNTs as well, but the results were significantly less consistent and could not easily be matched to simulation results. We strongly believe this to be mostly the result of the aforementioned considerable lack of consistency and uniformity with the Co-filled CNTs. However, all of the Co-filled CNT samples consistently achieved full 180° stage rotations as predicted. Our ongoing work regarding the uniform growth of Co-filled CNTs should resolve this discrepancy in the future.
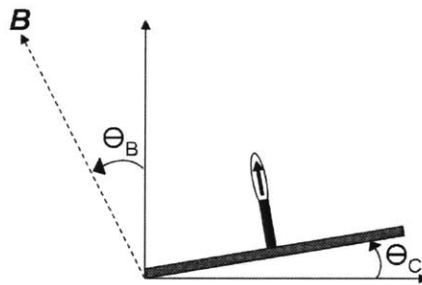
Figure 4-15: Definitions of Θ_B and Θ_C.
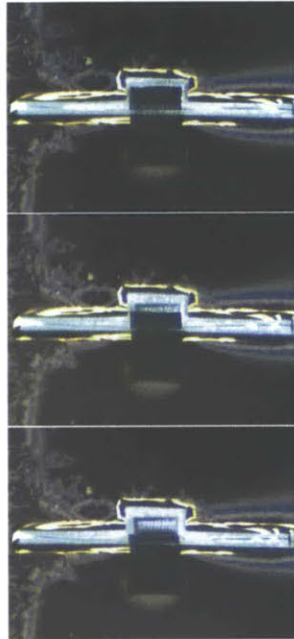
Figure 4-16: Top-down images of the magnetic test device at $\Theta_B = 10°$, $90°$, and $130°$, respectively.
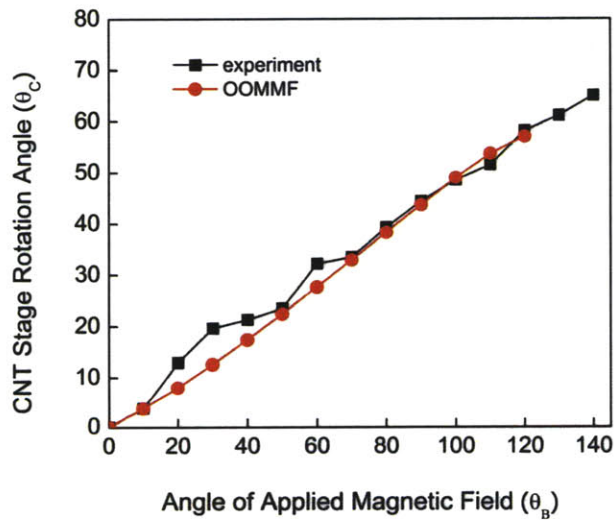
Figure 4-17: Experimental and simulation results of stage rotation angle vs. magnetic field angle.

While magnetic simulations based on OOMMF are highly effective, as just shown, in predicting magnetic rotation behavior of our CNT-covered membranes, the entire process can be time consuming and computationally intensive. One alternative is to use

information gathered from the OOMMF simulations to modify the dipole approximation model from Equation 4.3.

For instance, Figure 4-18 gives the OOMMF-generated overall magnetization angle Θ_M of the teardrop-shaped nanoparticle as a function of the external magnetization angle Θ_B. Whereas Θ_M should remain at 0° in ideal dipole approximations, Figure 4-18 shows that it increases almost linearly with the external field angle while trailing only slightly behind it, a manifestation of the torque-neutral spherical region of the nanoparticles mentioned earlier. Based on this information, Equation 4.3 can now be rewritten as Equation 4.4. Furthermore, this behavior can be easily converted into a dipole approximation correction factor α that can be used in conjunction with Equation 4.4 to quickly help determine the rotation behavior of CNT-encapsulated nanoparticles under various conditions. Figure 4-19 indicates how this correction factor scales, based on further OOMMF simulations, in relation to the intensity of the externally applied magnetic field while Equation 4.5 represents shows the new magnetic torque equation based on this correction factor α.
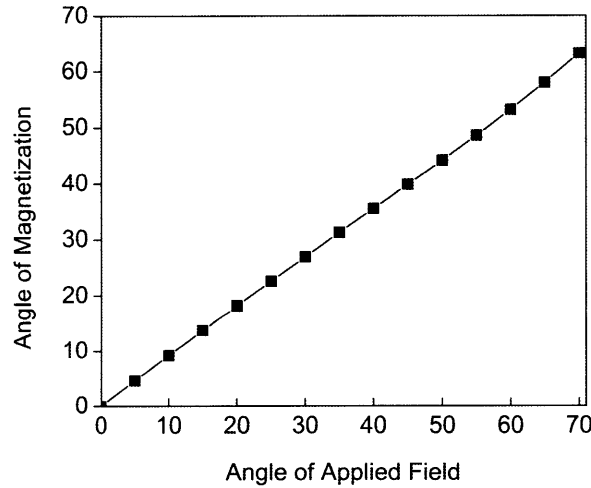
Figure 4-18: Average angle of magnetization inside the teardrop-shaped nanoparticle as a function of external field angle for B = 0.2 T and $\Theta = 45°$.

$$T_m = \frac{BM_sV}{\mu_0}(\theta_B - \theta_M)$$ (4.4)
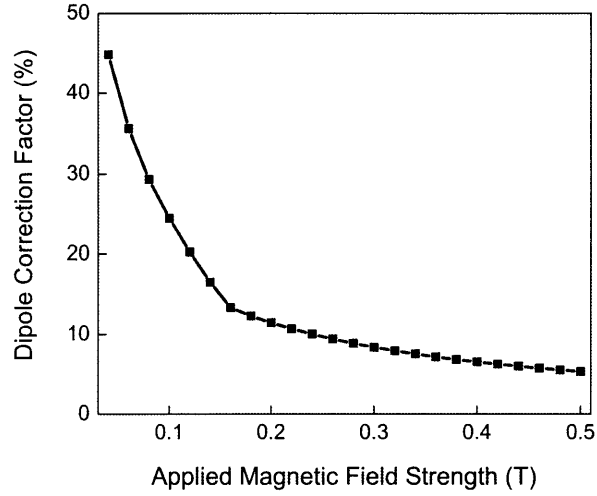
Figure 4-19: Dipole approximation correction factor α as a function of external field strength.

$$T_m = \frac{\alpha BM_sV\theta_B}{\mu_0}$$ (4.5)

Based on Figure 4-19 and Equation 4.5, quick approximations can be made of magnetic rotation behaviors of teardrop-shaped nanoparticles inside CNTs. Figure 4-20 compares this newly acquired approximation value to previous simulation and experimental results for membrane rotation. While the approximation breaks down at extreme field angles not shown in the graph, it nevertheless matches experimental data quite well.
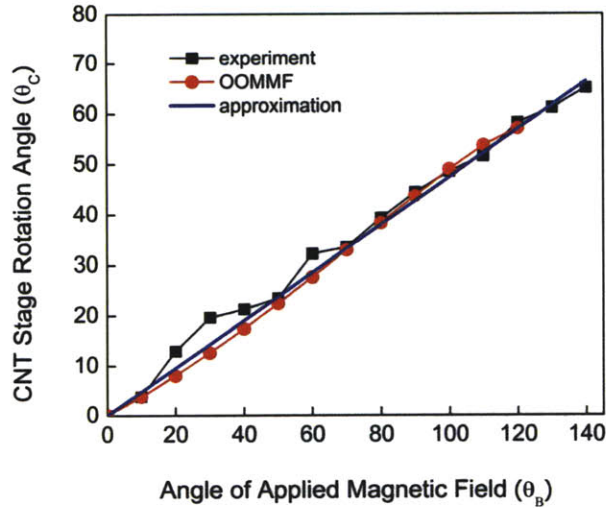
Figure 4-20: Experimental, simulation, and corrected approximation results for stage rotation angle vs. magnetic field angle.

4.3 Membrane latching

For most origami device applications, successfully actuated membranes further need to be permanently held in place through reliable latching mechanisms. As mentioned at the beginning of the chapter, magnetic attraction forces arising between nearby CNT tips could possibly enable magnetic latching between folded origami membranes. While other forms of membrane latching, such as nanomagnet arrays, meltable polymer, and mechanical links, have been successfully demonstrated by our group for origami applications, they typically require large areas of separately patterned structures dedicated for latching. Achieving latching through the use of CNTs that are already present on the membranes for device functionality and, as just described, membrane actuation purposes can significantly reduce the overall complexity of the origami device. This section will report on the initial and ongoing work regarding the use of CNTs for the latching of folded origami membranes.

4.3.1 CNT-enabled latching mechanisms

CNT-enabled latching of origami membranes basically boils down to the massively parallel attachments between CNTs on opposing sides. There are two main ways in which the CNTs on the origami membranes can latch on to each other. First and foremost is the just mentioned magnetic attraction force arising from the CNT-encapsulated nanoparticles. The attraction force F_m between two nearby magnets can be approximated by [117]

$$F_m = \frac{(MA)^2}{4\pi\mu_0 d^2} , \tag{4.6}$$

where M is the magnetization of the material, A is the cross-sectional area, and d is the distance between the two magnets. While the exact equation cannot be directly applied to the particular dimension and geometry of our nanoparticles, it can be used in conjunction with OOMMF simulations to find out approximately how much magnetic attraction force is being generated by our CNT pairs under both saturation and remanent magnetization.

Figure 4-21 shows the OOMMF-generated magnetic attraction forces between arrays of opposing Ni-filled as well as Co-filled CNTs under both saturation and remanent magnetization for the device used in Section 4.2 (reproduced below in Figure 4-22). The magnetic remanence values, which are approximately 32% of the saturation values for both Ni and Co-filled CNTs, have been obtained from the VSM results shown in Figure 4-5. The blue (diamond) line indicates the attraction force required to overcome the springback force of the torsional hinges and keep the two membranes latched. As indicated by Figure 4-21, the magnetic attraction force begins to overcome the mechanical springback force (i.e. latches the membranes) as opposing CNT tips start to get very close to each other ($<$ 400 nm). Although these results assume that the two membranes are perfectly parallel to each other and that all CNTs (~100,000 of them per side in this case) are of the exact same height and perfectly paired to a mate on the opposing side, all factors that would lead to a huge overestimation of the attraction forces, they nevertheless look promising for latching applications since it has already

been established that magnetic rotation forces can achieve full 180° rotation and thus can get the two membranes very close to each other. These results suggest that even after the external magnetic field has been removed, the nanomagnets inside the CNTs can keep the two membranes latched together as long as a large number of CNT pairs are within a few hundred nanometers of each other.
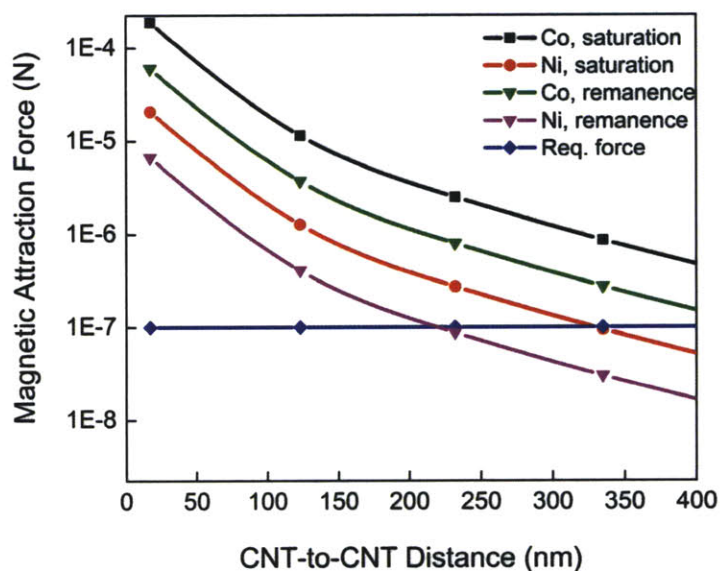
Figure 4-21: Simulation results of magnetic attraction force between two opposing CNT-covered origami membranes as a function of separation distance between CNT tips. The blue (horizontal) line indicates the required latching force based on torsional hinge geometry.
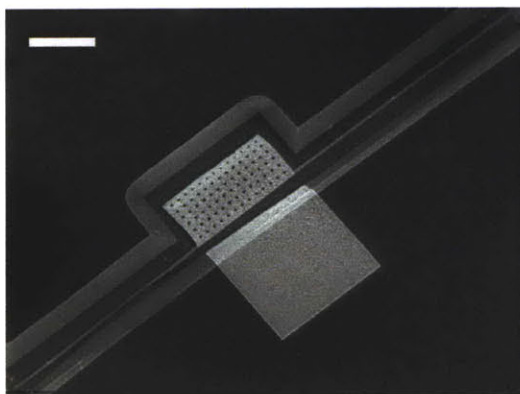
Figure 4-22: Test device used for magnetic latching tests. The bright rectangular regions indicate CNT forests (bar = 100um).

The second way in which the CNTs can become attached to each other is through van der Waals forces. Although these forces will only become significant when the CNTs are in intimate contact, they can be quite considerable. For example, based on the Derjaguin approximation, the pull-of force between two hemispheres (i.e. two CNT tips) of radius R and two cylinders (i.e. two CNT bodies) of radius R is given, respectively, by the following equations [121]:

$$F = \pi R W_a,$$ (4.7)

$$F = 2\pi R W_a,$$ (4.8)

where the work of adhesion W_a at intimate contact is approximated by

$$W_a \approx 2\gamma_g,$$ (4.9)

and the surface energy of graphite γ_g is ~165 mJ/m^2 [122]. For our given nanotube geometry, this means that the theoretical pull-off force between one pair of attached CNTs is ~100 nN! This alone is equal to the total force required to keep the membranes latched together. The commonly used Johnson-Kendall-Roberts (JKR) theory also gives similar results [122]. Although such approximation methods are known to be extremely ideal upper limits, up to around 10% of such values (approximately 1~15 nN) has been reported in literature for CNT-to-glass adhesions [122, 123] and can be anticipated for CNT-CNT interactions. In addition to magnetic attraction forces, the possible presence of strong van der Waals interaction forces between CNT-covered membranes further support the possibility of membrane latching via CNTs.

4.3.2 Initial results

The latching abilities of two CNT-covered membranes were clearly evident from the membrane rotation experiments mentioned in Section 4.2. Once the released membrane was folded over 180° and came in contact with the opposing CNT forest, there was clear latching between the two surfaces as evidenced by a very faint "snapping" action that

104

occurred when the two sides came became magnetically attracted to each other. This snapping action was nowhere as clear as the similar phenomenon demonstrated by Nichol *et al.* [14], but the slight warping of the folded membrane as well as the significant height nonuniformity of the Co-filled CNTs fully account for this discrepancy. Ni-filled CNTs, although exhibiting much greater uniformity, could not be used in this case since full 180° membrane rotations could not be performed as mentioned previously.

While the latching action between opposing CNT arrays occurred consistently in the presence of an external magnetic field, clearly indicating the large attraction forces between magnetically saturated nanoparticles in the CNT tips, sustained latching upon removal of the external field only occurred around 25% of the time. In such cases, there was clear membrane movement and partial detachment upon field removal indicating a significant decrease of attraction forces. However, it was not apparent as to which of the aforementioned CNT-enabled latching mechanisms were responsible, namely magnetic attraction under remanent magnetization or van der Waals forces between touching nanotubes, for the continued attachment. A clear SEM image of the latched membranes, although potentially helpful, was difficult to obtain since a long tumultuous journey through the MIT campus separated the SEM facility from the magnetic testing facility; many latched samples became unlatched by the time they reached the SEM. Figure 4-23 shows one of the few samples that survived the trip. In such images, however, the CNT-CNT interaction region is not clearly visible due to the large size and slight curvature of the latched membrane.
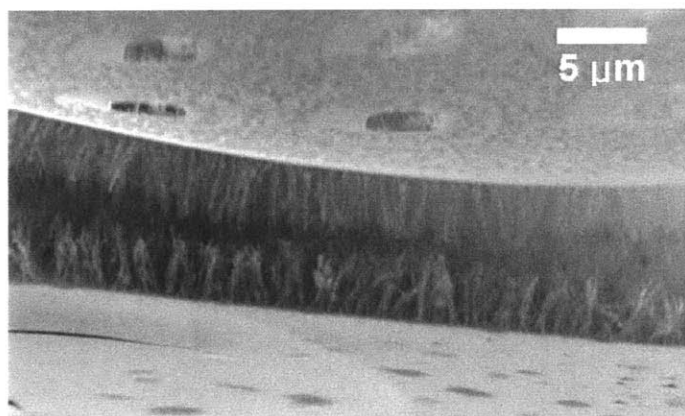
Figure 4-23: Side SEM view of a folded and semi-permanently latched CNT membrane.

By chance, the image shown in Figure 4-24 was taken where a significantly warped top membrane had become attached to the CNT forest on the bottom through the same attachment process described above. However, the highly curved shape of the top membrane allowed us to take a very good look at the small region where the CNT interactions were taking place. Surprisingly, very few CNTs from both sides were actually attached to each other and keeping the top membrane from popping back. In fact, a careful examination of the CNT interaction region (Figure 4-24(b) and inset in Figure 4-24(a)) revealed that only about 30 or so CNT pairs were in contact with each other while the rest of the unlatched CNTs were located far beyond the required separation distance for significant attraction under remanent magnetization. Assuming that van der Waals forces were solely responsible for keeping this membrane latched, this translates into around 3 nN of adhesion force per CNT, which is well inline with the values of between 1~15nN reported by other groups [122, 123]. While magnetic attraction under remanent magnetization still cannot be eliminated as a source of prolonged membrane attachment, van der Waals attraction between attached CNTs presents itself as a very strong primary factor.
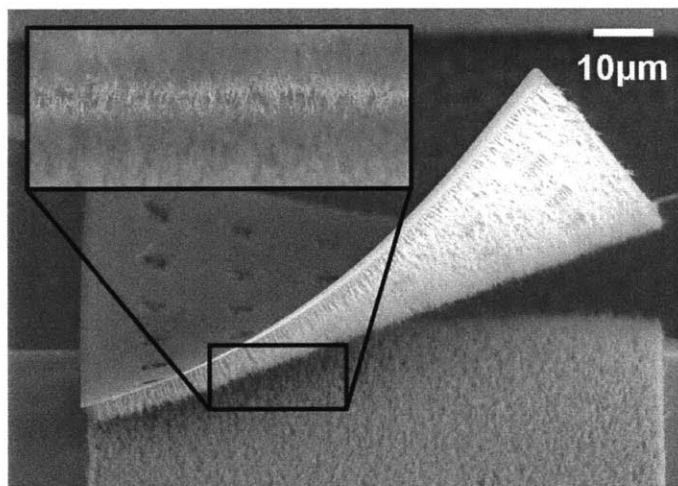
(a)
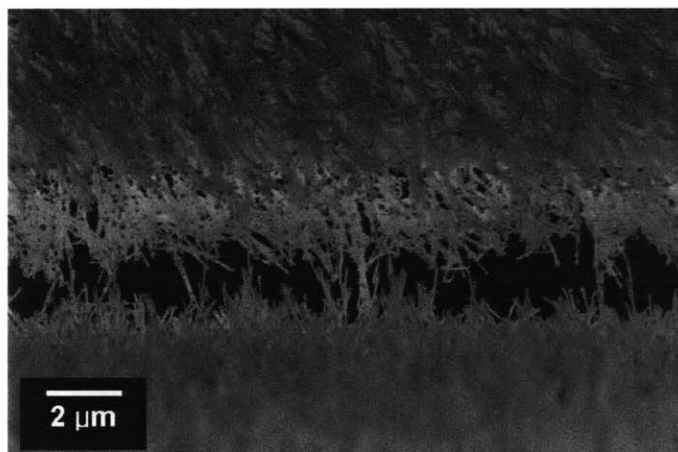
(b)

Figure 4-24: (a) Isometric and (b) closeup SEM images of the CNT interaction region in a highly warped device.

Figure 4-24(b) reveals another interesting point about CNT latching. While there is generally a pretty significant variation in CNT lengths, there are occasional pairings between CNTs that appear to be significantly taller than their neighbors. Additionally, the overwhelming majority of such pairings take the form shown in Figure 4-25. Such occurrences are reflective not of unusually long CNTs but actually of CNT pairs where one or both of the nanotubes have been detached from the substrate, as is often the case for MWCNTs [122]. The plot of magnetic attraction force versus distance between the

pointed ends of the encapsulated nanoparticles, shown in Figure 4-26, indicates that the particular pairing geometry shown in Figure 4-25 is a result of magnetic force equilibrium. Furthermore, the tiny magnetic attraction forces involved in such pairings suggest that at least one of the CNTs in the pair are completely detached and free-floating. This information can be useful in analyzing images such as the one shown in Figure 4-24(b) and determining which CNTs are contributing to the overall latching of the membranes (and which are just loose, detached CNTs).
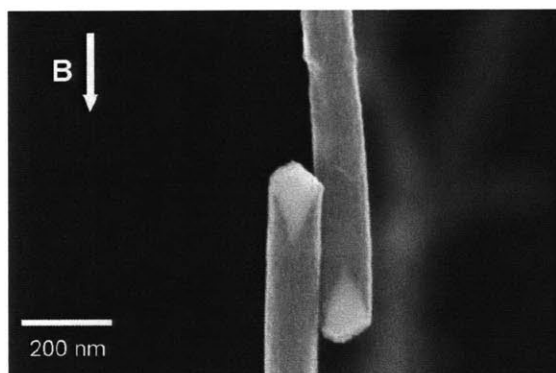
Figure 4-25: Two CNTs attached to each other in a magnetically stable arrangement.
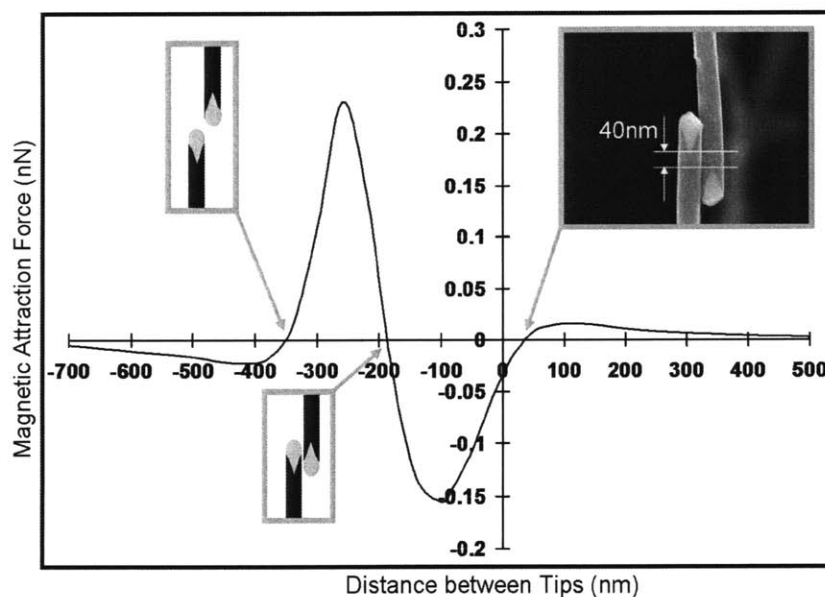
Figure 4-26: Simulation results showing magnetic attraction force as a function of distance between nanoparticle tips. The arrangement shown in Figure 4-25 is the only stable configuration.

108

One final note of interest is the CNT's ability to bend laterally under an external magnetic field. For instance, when two CNT tips are close to each other in the lateral direction, a vertical external field creates attraction forces between the two tips as shown in Figure 4-27. If the two tips are sufficiently close, the magnetic attraction force between them can actually cause the CNTs to bend towards each other. For CNTs that are 6 μm long and 100 nm wide with a typical MWCNT Young's modulus of ~100 GPa [124], this occurs when the two tips are approximately ~85 nm from each other as indicated by Figure 4-27. Since significantly defect-laden CNTs can actually exhibit Young's modulus that are orders of magnitude less [124], it is possible that the type of behavior shown in Figure 4-28 between CNTs that are actually around 500 nm apart ($>>$ 85 nm) could be a result of magnetic attraction between the CNT tips. If properly designed, van der Waals attraction between CNT-covered membranes could potentially be significantly enhanced by magnetically bending individual CNTs to increase the number of CNT pairs that come into contact.
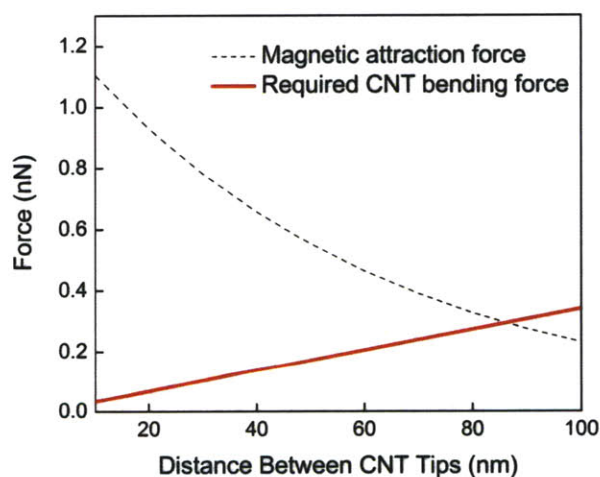
Figure 4-27: Lateral magnetic attraction force and required CNT bending force as a function of lateral distance between CNTs.

Figure 4-28: A CNT possibly bent due to magnetic attraction force from adjacent CNT.

4.4 Summary of magnetic behavior

In conclusion, we have grown arrays of Ni and Co-filled CNTs on floating TiN stages and shown that a rotating external magnetic field generates a magnetic torque on the encapsulated nanoparticles which in turn rotates the entire stage on which the CNTs are grown. Through 3-D magnetic simulations, we have also demonstrated that this stage rotation behavior can be accurately modeled based on magnetic properties as well as size and shape of the encapsulated nanoparticle. Consequently, we can now predict how an individual or an array of nanomagnet-filled CNTs will behave under a given external magnetic field. Alternatively, magnetic rotation of CNTs can be used to collect information about the CNTs themselves or even their surrounding environment. Additionally, initial work involving the magnetic attraction and latching of CNT tips was also presented.

Chapter 5

Conclusion

Without a doubt, the past decade has experienced tremendous progress in the areas of micro- and nanoscale fabrication. Furthermore, such advancements in fabrication technologies have spawned and continue to spawn truly novel device applications in far-reaching areas of science and engineering. Of the many different types of nanoscale fabrication/engineering/structuring techniques that are currently available, the growth of carbon nanotubes, the now ubiquitous rolled-up graphene sheets, were of particular interest. While significant strides have been made in the characterization, growth, filtering, and even applications of CNTs in certain research and commercial settings, the use of CNTs in more traditional micro- and nanofabrication platforms is still exceedingly rare due to inherent difficulties that exist with conventional CNT integration techniques.

In this thesis, a membrane folding approach to 3-D micro- and nanofabrication, namely the Nanostructured Origami™ process, was combined with *in situ*, PECVD-based growth of vertically aligned CNTs. The significance of integration with the origami process is twofold. First, standardized micro/nanofabrication and CNT integration, a previously exotic and relatively difficult nanomanufacturing feat, are combined into a single, fab-friendly platform. In effect, the CNT becomes just another element in the ever-expanding micro/nanofabrication arsenal and simply an additional processing step in the origami process. For many, this will open up new possibilities for taking advantage of the many unique and valuable attributes of CNTs. Second, the usefulness of integrated CNTs are vastly increased by placing them in a 3-D device environment

provided by the origami process. As the supercapacitor application in Chapter 3 demonstrated, the newly gained dimensional freedom will allow the CNTs to be used in ways never before imagined in conventional micro/nanofabrication settings. Another example of increased CNT utility, enabled by the 3-D origami process, is the magnetic membrane manipulation technique shown in Chapter 4 whereby external magnetic field manipulation resulted in the rotation and latching of single strands and large arrays of CNTs.

5.1   Summary

The following achievements were made and discussed throughout the course of this thesis:

- The PECVD-based CNT growth step was integrated into the origami fabrication scheme. This was accomplished by using a new membrane material, TiN, which allowed excellent and uniform growth of CNTs on its surface while maintaining electrical conductivity into the CNTs. The high temperature growth process as well as the subsequent presence of CNTs on the origami membranes were accommodated for by introducing a new post-CNT-growth metallization method as well as making appropriate modifications to the XeF_2-based membrane release process.

- A fully-functioning microscale supercapacitor with vertically aligned CNT electrodes was fabricated using the CNT-origami process and electrochemically tested. The device was created from start to finish using standard fabrication equipment found in the MTL and is designed to allow large-scale batch fabrication. The CNT-origami supercapacitor's favorable electrochemical performance and largely MEMS-compatible processing steps make it an excellent choice for serving as an integrated power supply in self-powered, autonomous microsystem applications.

- Magnetic properties of CNT tip-encapsulated catalyst particles were studied through theory, magnetic simulation, and experiment. Accordingly, the precise magnetic rotation behavior of CNT-covered membranes was predicted and verified through purpose-built CNT-origami magnetic test structures. Membrane latching behavior, enabled through the magnetic attraction between opposing CNT tips, was also explored, and preliminary results were shown.

5.2 Future works

While the research presented in this thesis makes unique and varied contributions to the field of CNT-based nanomanufacturing, further related works, some of which are listed below, will be highly beneficial:

- In-depth investigation of CNT-to-CNT magnetic and van der Waals interactions. This can be achieved, for example, by creating folding membranes patterned with single strands of equally spaced and sized CNTs to better isolate and identify CNT behavior.

- Further study and demonstration of controllable CNT-to-CNT latching and unlatching under external magnetic field manipulation. For example, a CNT-array-based gecko foot with variable attachment and detachment force arising from CNT-to-CNT magnetic interactions can be built and tested.

- Actual implementation of CNT supercapacitor as a power source in self-sufficient MEMS device, likely in conjunction with an energy harvesting device fabricated concurrently on the same chip. Power output and management of the origami power source will also need to be addressed.

- Demonstration of a biological, chemical, acoustic, and/or magnetic sensing device based on *in situ* CNTs on an origami platform.

Appendix A

Detailed fabrication process

A.1 Lift-off process for post-CNT metallization

A modified lift-off process can be used to pattern many different types of materials, especially metals, after the *in situ* growth of carbon nanotubes and is thus ideal for post-CNT metallization in various origami-based devices. The detailed processing steps, as performed in the Technology Research Laboratory (TRL) of MIT's Microsystems Technology Laboratories (MTL), are listed below (laboratory and equipment names are shown in *italics*). The following steps will result in a final photoresist thickness of approximately 6-8 µm and can be used on samples with CNTs that are up to 8 µm in length.

1. Dispense AZ 5214 image reversal photoresist on the sample and spin for 30 seconds at 1300 RPM (*TRL-coater*).

2. Bake for 5 minutes at 88°C (*TRL-varTemp*).

3. Repeat steps 1-2 two more times. During the last cycle, heat for 20 minutes instead of 5 minutes.

4. Expose for 3.0 seconds (*TRL-EV1*).

5. Perform a post-exposure bake (PEB) for 30 minutes at 88°C (*TRL-varTemp*).

6. Flood expose without a mask for 75 seconds. Perform the exposure in 25-second intervals with a 2-minute rest between steps (*TRL-EV1*).

7. Develop in AZ 422 for approximately 9 minutes while maintaining a light agitation (*TRL-photo-wet*).

8. Rinse with DI water and microscope inspect exposed areas.

9. If not properly developed, flood expose for 30 seconds and develop for 2 minutes. Repeat until desired results are obtained.

10. Deposit desired material to be patterned (*TRL-various*).

11. Place in airtight container and soak overnight in acetone (*TRL-photo-wet*).

12. Place container in ultrasonic bath for approximately 3 minutes (*TRL-photo-wet*).

13. Remove the wafer and immediately clean with acetone followed by isopropyl alcohol (*TRL-photo-wet*).

14. Immediately blow dry sample with N_2 gun.

A.2 Process flow for CNT-origami supercapacitor

The detailed processing steps for the CNT-based supercapacitor, as performed in the Integrated Circuits Laboratory (ICL) and the Technology Research Laboratory (TRL) of MIT's Microsystems Technology Laboratories (MTL), are listed below (laboratory and equipment names are shown in *italics*).

1. Begin with newly opened or RCA-cleaned 6-inch silicon wafers (*ICL-RCA*).

2. Deposit 300 nm of silicon nitride (*ICL-VTR*).

3. Deposit 1 μm of titanium nitride (*ICL-endura*).

4. Dispense OCG 825 photoresist on the sample and spin for 30 seconds at 1200 RPM (*TRL-coater*).

5. Bake for 5 minutes at 90°C (*TRL-pre-bake*).

6. Repeat steps 1-2 two more times. During the last cycle, heat for 30 minutes instead of 5 minutes.

7. Expose for 10.0 seconds (*TRL-EV1*).

8. Develop in OCG 934 for approximately 5 minutes or until desired areas are cleared (*TRL-photo-wet*).

9. Spin, rinse, and dry (*TRL-SRD*).

10. Perform a hard bake for 30 minutes at 120°C (*TRL-post-bake*).

11. Etch the titanium nitride layer and the silicon nitride simultaneously using the "TiN 6-inch" recipe. Set endpoint time to approximately 400 seconds (*ICL-rainbow*).

12. Visually inspect sample to make sure that the silicon layer underneath the etched nitride layers is visible. If not, repeat step 5 in 60-second increments.

13. Remove remaining photoresist (*ICL-asherICL*).

14. Soak wafers in Nano-Strip for 10 minutes to further remove any photoresist residue (*TRL-acid-hood*).

15. Spin, rinse, and dry (*TRL-SRD*).

16. Follow standard MTL recipe to pattern approximately 1.5 μm of AZ 5214 image reversal photoresist (*TRL-various*).

17. Deposit 25 nm of nickel (*TRL-e-beamFP*).

18. Follow standard MTL recipe to remove photoresist and unwanted material (*TRL-various*).

19. Grow CNTs using the "Two_Step_AC" recipe. Set "catalyst annealing time" to 30 seconds and "CNT growth time" to 1200 seconds. These times may be adjusted as necessary (*TRL-CCNT*).

20. Deposit 600 nm of gold (*TRL-e-beamFP*) using the modified lift-off process from Appendix A.1 (*TRL-various*).

21. Directly pour SU-8 2015 onto the sample, making sure to cover as much of the exposed surface with SU-8 prior to spinning (*TRL-SU8spinner*).

22. Ramp from 0 to 500 RPM and hold for 30 seconds (*TRL-SU8spinner*).

23. Spin at 3100 RPM for 30 seconds (*TRL-SU8spinner*).

24. Bake at 95°C for 5 minutes (*TRL-hotplate*).

25. Cool at room temperature for approximately 1 hour.

26. Expose for 10.0 seconds. Perform the exposure in two steps with a 1-minute rest between steps (*TRL-EV1*).

27. Perform a two-step post-exposure bake (PEB): 3 minutes at 65°C and 1 minute at 95°C. Immediately switch off hot plate and cool for 1 hour directly on the hot plate (*TRL-hotplate*).

28. Develop in PM acetate for approximately 3 minutes while maintaining a light agitation. Immediately rinse with isopropyl alcohol (*TRL-SU8spinner*).

29. Perform a hard bake for 10 minutes at 150°C (*TRL-hotplate*).

30. Sacrificially etch away silicon and release device in small batches (maximum of 8 dies per run). Run the full automatic etch cycle with one 60-second etching step (*TRL-XeF$_2$*).

31. Visually inspect sample with microscope after each etch cycle and keep repeating step 30 until all the devices are released. This step may need to be repeated up to 20 times depending on various processing conditions and parameters.

A.3 Process flow for magnetic CNT test structure

The detailed processing steps for the magnetic CNT test structures, as performed in the Integrated Circuits Laboratory (ICL) and the Technology Research Laboratory (TRL) of MIT's Microsystems Technology Laboratories (MTL), are listed below (laboratory and equipment names are shown in *italics*).

1. Begin with newly opened or RCA-cleaned 6-inch silicon wafers (*ICL-RCA*).

2. Deposit 100 nm of titanium nitride (*ICL-endura*).

3. Follow standard MTL recipe to pattern approximately 1.0 μm of OCG 825 photoresist (*TRL-various*).

4. Etch the titanium nitride layer and the silicon nitride simultaneously using the "TiN 6-inch" recipe. Set endpoint time to approximately 60 seconds (*ICL-rainbow*).

5. Remove remaining photoresist (*ICL-asherICL*).

6. Soak wafers in Nano-Strip for 10 minutes to further remove any photoresist residue (*TRL-acid-hood*).

7. Spin, rinse, and dry (*TRL-SRD*).

8. Follow standard MTL recipe to pattern approximately 1.5 μm of AZ 5214 image reversal photoresist (*TRL-various*).

9. Deposit 25 nm of nickel (*TRL-e-beamFP*).

10. Follow standard MTL recipe to remove photoresist and unwanted material (*TRL-various*).

11. Grow CNTs using the "Two_Step_AC" recipe. Set "catalyst annealing time" to 30 seconds and "CNT growth time" to 1200 seconds. These times may be adjusted as necessary (*TRL-CCNT*).

12. Sacrificially etch away silicon and release device in small batches (maximum of 8 dies per run). Run the full automatic etch cycle with one 60-second etching step (*TRL-XeF$_2$*).

13. Visually inspect sample with microscope after each etch cycle and keep repeating step 30 until all the devices are released. This step may need to be repeated up to 5 times depending on various processing conditions and parameters.

Bibliography

[1]   G. E. Moore. Cramming more components onto integrated circuits. *Electronics*, 38: 56-59, 1965.

[2]   S. Natarajan *et al.* A 32 nm logic technology featuring 2nd-generation high-k + metal-gate transistors, enhanced channel strain and 0.171 μm^2 SRAM cell size in a 291 Mb array. *IEEE International Electron Devices Meeting*, 1-3, 2008.

[3]   O. Akhavan and M. Abdolahad. Physical bounds of metallic nanofingers obtained by mechano-chemical atomic force microscope nanolithography. *Applied Surface Science*, 255: 3513-3517, 2009.

[4]   Z. L. Wang and J. Song. Piezoelectric nanogenerators based on zinc oxide nanowire arrays. *Science*, 312: 243-246, 2006.

[5]   H. Tanaka, *et al.* Bit cost scalable technology with punch and plug process for ultra high density flash memory. *IEEE Symposium on VLSI Technology*, 14-15, 2007.

[6]   K. W. Guarini *et al.* Electrical integrity of state-of-the-art 0.13 μm SOI CMOS devices and circuits transferred for three-dimensional (3D) integrated circuit (IC) fabrication. *IEEE International Electron Devices Meeting*, 943-945, 2002.

[7]   E. Yablonovitch. Photonic Crystals. *Journal of Modern Optics*, 41: 173-194, 1994.

[8]   E. Leclerc, K. S. Furukawa, F. Miyata, Y. Sakai, T. Ushida, and T. Fujii. Fabrication of microstructures in photosensitive biodegradable polymers for tissue applications. *Biomaterials*, 25: 4683-4690, 2004.

[9]   R. W. Hart, H. S. White, B. Dunn, and D. R. Rolison. 3-D microbatteries. *Electrochemistry Communications*, 5: 120-123, 2003.

[10] H. J. In. Origami nanofabrication of three-dimensional electrochemical energy storage devices. *Master's Thesis*, MIT, 2005.

[11] H. J. In, W. J. Arora, T. Bucher, S. M. Jurga, H. I. Smith, and G. Barbastathis. The Nanostructured Origami™ 3D fabrication and assembly process for nanomanufacturing. *IEEE Conference on Nanotechnology*, 358-360, 2004.

[12] W. J. Arora, A. J. Nichol, H. I. Smith, and G. Barbastathis. Membrane folding to achieve three-dimensional nanostructures: Nanopatterned silicon nitride folded with stressed chromium hinges. *Applied Physics Letters*, 88: 053108, 2006.

[13] H. J. In, S. Kumar, Y. Shao-Horn, and G. Barbastathis. Origami fabrication of nanostructured, three-dimensional devices: Electrochemical capacitors with carbon electrodes. *Applied Physics Letters*, 88: 083104, 2006.

[14] A. J. Nichol, W. J. Arora, and G. Barbastathis. Thin membrane self-alignment using nanomagnets for three-dimensional nanomanufacturing. *Journal of Vacuum Science and Technology B*, 24: 3128-3131, 2006.

[15] S. M. Jurga. 3D micro and nanomanufacturing via folding of 2D membranes. *Master's Thesis*, MIT, 2003.

[16] N. S. Shaar, G. Barbastathis, and C. Livermore. Cascaded mechanical alignment for assembling 3D MEMS. *IEEE International Conference on Micro Electro Mechanical Systems (MEMS)*, 1064-1068, 2008.

[17] H. J. In, H.W. Lee, S.-G. Kim, and G. Barbastathis. Nanomanufacturing of carbon nanotubes on titanium nitride. *International Journal of Nanomanufacturing*, in press.

[18] W. J. Arora, S. Sijbrandij, L. Stern, J. Notte, H. I. Smith, G. Barbastathis. Membrane folding by helium ion implantation for three-dimensional device fabrication. *Journal of Vacuum Science and Technology B*, 25: 2184-2187, 2007.

[19] H. J. In, H. W. Lee, A. J. Nichol, S.-G. Kim, and G. Barbastathis, *Journal of Vacuum Science and Technology B*, 26: 2509-2512, 2008.

[20] S. Iijima. Helical microtubules of graphitic carbon. *Nature*, 354: 56-58, 1991.

[21] M. S. Dresselhaus, G. Dresselhaus, P. Avouris. *Carbon Nanotubes: Advanced Topics in the Synthesis, Structure, Properties, and Applications (Series Topics in Applied Physics)*. Springer Verlag, Berlin, 2001.

[22]   S. Iijima, and T. Ichihashi. Single-shell carbon nanotubes of 1-nm diameter. *Nature*, 363: 603-605, 1993.

[23]   M. Meyyappan, L. Delzeit, A. Cassell, and D. Hash. Carbon nanotube growth by PECVD: A review. *Plasma Sources Science and Technology*, 12: 205-216, 2003.

[24]   T. Guo, P. Nikolev, A. Thess, D. T. Colbert, and R. E. Smalley. *Chemical Physics Letters*, 243: 49-54, 1995.

[25]   C. -H. Kiang, W. A. Goddard, R. Beyers, and D. S. Bethune. Carbon nanotubes with single-layer walls. *Carbon*, 33: 903-914, 1995.

[26]   J. Kong, H. T. Soh, A. M Cassell, C. F. Quate, and H. Dai. Synthesis of individual single-walled carbon nanotubes on patterned silicon wafers. *Nature*, 395: 878-881, 1998.

[27]   G. Eres, C. M. Rouleau, M. Yoon, A. A. Puretzky, J. J. Jackson, and D. B. Geohegan. Model for self-assembly of carbon nanotubes from acetylene based on real-time studies of vertically aligned growth kinetics. *Journal of Physical Chemistry C*, 113: 15484-15491, 2009.

[28]   A. A. Puretzky, D. B. Geohegan, S. Jesse, I. N. Ivanov, and G. Eres. In situ measurements and modeling of carbon nanotube array growth kinetics during chemical vapor deposition. *Applied Physics A*, 81: 223-240, 2005.

[29]   M. Staderman *et al*. Mechanism and kinetics of growth termination in controlled chemical vapor deposition growth of multiwall carbon nanotube arrays. *Nano Letters*, 9: 738-744, 2009.

[30]   Z. F. Ren, Z. P. Huang, J. W. Xu, J. H. Wang, P. Bush, M. P. Siegal, and P. N. Provencio. Synthesis of large arrays of well-aligned carbon nanotubes on glass. *Science*, 282: 1105-1107, 1998.

[31]   Z. P. Huang, J. W. Xu, Z. F. Ren, J. H. Wang, M. P. Siegal, and P. N. Provencio. Growth of highly oriented carbon nanotubes by plasma-enhanced hot filament chemical vapor deposition. *Applied Physics Letters*, 73: 3845-3847, 1998.

[32]   J. G. Wen *et al*. Growth and characterization of aligned carbon nanotubes from patterned nickel nanodots and uniform thin films. *Journal of Materials Research*, 16: 3246-3253, 2001.

[33]   C. Bower, W. Zhu, S. Jin, and O. Zhou. Plasma-induced alignment of carbon nanotubes. *Applied Physics Letters*, 77: 830-832, 2000.

[34] Y. H. Wang, J. Lin, C. H. A. Huan, and G. S. Chen. Synthesis of large area aligned carbon nanotube arrays from C_2H_2-H_2 mixture by rf plasma enhanced chemical vapor deposition. *Applied Physics Letters*, 79: 680-682, 2001.

[35] J. F. AuBuchon, L.-H. Chen, A. I. Gapin, D.-W. Kim, C. Daraio, and S. Jin. Multiple sharp bendings of carbon nanotubes during growth to produce zigzag morphology. *Nano Letters*, 4: 1781-1784, 2004.

[36] S. Fan, M. G. Chapline, N. R. Franklin, T. W. Tombler, A. M. Cassell, and H. Dai. Self-oriented regular arrays of carbon nanotubes and their field emission properties. *Science*, 283: 512-514, 1999.

[37] R. Andrews, D. Jacques, A. M. Rao,, F. Derbyshire, D. Qian, X. Fan, E. C. Dickey, and J. Chen. Continuous production of aligned carbon nanotubes: A step closer to commercial realization. *Chemical Physics Letters*, 303: 467-474, 1999.

[38] S. Hofmann, C. Ducati, J. Robertson, and B. Kleinsorge. Low-temperature growth of carbon nanotubes by plasma-enhanced chemical vapor deposition. *Applied Physics Letters*, 83: 135-137, 2003.

[39] V. I. Merkulov, D. H. Lowndes, Y. Y. Wei, and G. Eres. Patterned growth of individual and multiple vertically aligned carbon nanofibers. *Applied Physics Letters*, 76: 3555-3557, 2000.

[40] A. M. Cassell, J. A. Raymakers, J. Kong, and H. Dai. Large scale CVD synthesis of single-walled carbon nanotubes. *Journal of Physical Chemistry B*, 103: 6484-6492, 1999.

[41] Y. Huang, X. Duan, Q. Wei, C. M. Lieber. Directed assembly of one dimensional nanostructures into functional networks. *Science*, 292: 630-633, 2001.

[42] A. Hall, W. G. Matthews, R. Super.ne, M. R. Falvo, and S. Washburn. Simple and efficient method for carbon nanotube attachment to scanning probes and other substrates. *Applied Physics Letters*, 82: 2506-2508, 2003.

[43] D. P. Long, J. L. Lazorcik, and R. Shashidhar. Magnetically directed self-assembly of carbon nanotube devices. *Advanced Materials*, 16: 814-819, 2004.

[44] R. Krupke, F. Hennrich, H. B. Weber, M. M. Kappes, and H. V. Löhneysen. Simultaneous deposition of metallic bundles of single-walled carbon nanotubes using ac-dielectrophoresis. *Nano Letters*, 3: 1019-1023, 2003.

[45] A. Vijayaraghavan, S. Blatt, D. Weissenberger, M. Oron-Carl, F. Hennrich, D. Gerthsen, H. Hahn, and R. Krupke. Ultra-large-scale directed assembly of single-walled carbon nanotube devices. *Nano Letters*, 7: 1556-1560, 2007.

[46] H. Dai, J. H. Hafner, A. G. Rinzler, D. T. Colbert, and R. E. Smalley. Nanotubes as nanoprobes in scanning probe microscopy. *Nature*, 384: 147-150, 1996.

[47] J. H. Hafner, C.-L. Cheung, T. J. Oosterkamp, and C. M. Lieber. High-yield assembly of individual single-walled carbon nanotube tips for scanning probe microscopies. *Journal of Physical Chemistry B*, 105: 734-736, 2001.

[48] Q. Ye, A. M. Cassell, H. Liu, K.-J. Chao, J. Han, and M Meyyappan. Large scale fabrication of carbon nanotube probe tips for atomic force microscopy critical dimension imaging applications. *Nano Letters*, 4: 1301-1308, 2004.

[49] J. E. Jang *et al.* Nanoelectromechanical switches with vertically aligned carbon nanotubes. *Applied Physics Letters*, 87: 163114, 2005.

[50] T. Kawano, H. C. Chiamori, M. Suter, Q. Zhou, B. D. Sosnowchik, and L. Lin. An electrothermal carbon nanotube gas sensor. *Nano Letters*, 7: 3686-3690, 2007.

[51] S. Kim, H. W. Lee, and S.-G. Kim. Transplanting assembly of carbon nanotube-tipped atomic force microscope probes. *Applied Physics Letters*, 94: 193102, 2009.

[52] T. A. El-Aguizy, J.-H. Jeong, Y.-B. Jeon, W. Z. Li, Z. F. Ren, and S.-G. Kim. Transplanting carbon nanotubes. *Applied Physics Letters*, 85: 5995-5997, 2004.

[53] W. Lu, L. Qu, K. Henry, and L. Dai. High performance electrochemical capacitors from aligned carbon nanotube electrodes and ionic liquid electrolytes. *Journal of Power Sources*, 189: 1270-1277, 2009.

[54] M. A. Guillorn *et al.* Individually addressable vertically aligned carbon nanofiber-based electrochemical probes. *Journal of Applied Physics*, 91: 3824-3828, 2002.

[55] L. Gao *et al.* Growth of aligned carbon nanotube arrays on metallic substrate and its application to supercapacitors. *Solid State Communications*, 146: 380-383, 2008.

[56] Y.-K. Kim *et al.* Electron-emission properties of titanium carbide-coated carbon nanotubes grown on a nano-sized tungsten tip. *Thin Solid Films*, 517: 1156-1160, 2008.

[57]   Y. Q. Jiang, Q. Zhou Q, and L. Lin. Planar MEMS supercapacitor using carbon nanotube forests. *IEEE MEMS*, 587-590, 2009.

[58]   J. Shi, Y. F. Lu, K. J. Yi, Y. S. Lin, S. H. Liou, J. B. Hou, and X. W. Wang. Direct synthesis of single-walled carbon nanotubes bridging metal electrodes by laser-assisted chemical vapor deposition. *Applied Physics Letters*, 89: 083105, 2006.

[59]   A. M. Rao, D. Jacques, R. C. Haddon, W. Zhu, C. Bower, and S. Jin. In situ grown carbon nanotube array with excellent field emission characteristics. *Applied Physics Letters*, 76: 3813-3815, 2000.

[60]   H. F. Winters and J. W. Coburn. The etching of silicon with XeF2 vapor. *Applied Physics Letter*, 34: 70-73, 1979.

[61]   URL: http://mail.mems-exchange.org

[62]   D. Seneviratne, G. N. Nielson, S. Takahashi, G. Barbastathis, and H. L. Tuller. On the use of titanium nitride as structural material for nano-electro-mechanical systems (NEMS). *IEEE Conference on Nanotechnology*, 138-141, 2005.

[63]   I. W. T. Chan, K. B. Brown, R. P. W. Lawson, A. M. Robinson, Y. Ma, and   D. Strembicke. Gas phase pulse etching of silicon for MEMS with xenon difluoride. *IEEE Canadian Conference on Electrical and Computer Engineering*, 1637-1642, 1999.

[64]   D. Wu and E. J. Karwacki Jr., U. S. Patent 20070117396, 2007.

[65]   H.-Y. Chen and F.-H Lu. Oxidation behavior of titanium nitride films. *Journal of Vacuum Science and Technology A*, 23: 1006-1009, 2005.

[66]   B. Ozturk, B. N. Flanders, D. R. Grischkowsky, and T. D. Mishima. Single-step growth and low resistance interconnecting of gold nanowires. *Nanotechnology*, 18: 175707-175714, 2007.

[67]   L.-H. Chang, W. G. Cowden, J. Christiansen, D. Werho, and N. D. Theodore. Is Ti contamination in Si wafer processing an issue? *Journal of the Electrochemical Society*, 143: 2353-2356, 1996.

[68]   J. F. Creemer, D. Briand, H. W. Zandbergen, W. van der Vlist, C. R. de Boer, N. F. de Rooij, and P. M. Sarro. Microhotplates with TiN heaters. *Sensors and Actuators A*, 148: 416-421, 2008.

[69] V. I. Merkulov, M. A. Guillorn, D. H. Lowndes, M. L. Simpson, and E. Voelkl. Shaping carbon nanostructures by controlling the synthesis process. *Applied Physics Letters*, 79: 1178-1180, 2001.

[70] T. de los Arcos *et al.* Influence of iron-silicon interaction on the growth of carbon nanotubes produced by chemical vapor deposition. *Applied Physics Letters*, 80: 2383-2385, 2002.

[71] T. Gabay *et al.* Carbon nanotube micro-electrode array. *International Conference on Solid-State Sensors, Actuators and Microsystems*, 1553-1556, 2007.

[72] Y. T. Cheng, L. Lin, and K. Naja.. Localized silicon fusion and eutectic bonding for MEMS fabrication and packaging. *Journal of Microelectromechanical Systems*, 9: 3-8, 2000.

[73] S. Logothetidis and A. Barborica. In-situ and real time room temperature oxidation studies of fcc TiN thin films. *Microelectronic Engineering*, 33: 309-316, 1997.

[74] B. Bahreyni and C. Shafai. Investigation and simulation of XeF_2 isotropic etching of silicon. *Journal of Vacuum Science and Technology A*, 20: 1850-1854, 2002.

[75] B. E. Conway. *Electrochemical Supercapacitors: Scientific Fundamentals and Technological Applications.* Plenum, New York, 1999.

[76] E. Frackowiak, K. Metenier, V. Bertagna, and F. Béguin. Supercapacitor electrodes from multiwalled carbon nanotubes. *Applied Physics Letters*, 77: 2421-2423, 2000.

[77] E. Frackowiak and F. Béguin. Carbon materials for the electrochemical storage of energy in capacitors.*Carbon*, 39: 937-950, 2001.

[78] H. Zhang, G. Cao G, Y. Yang, and Z. Gu. Comparison between electrochemical properties of aligned carbon nanotube array and entangled carbon nanotube electrodes. *Journal of the Electrochemical Society*, 155: K19-K22, 2008.

[79] K. H. An *et al.* Supercapacitors using single-walled carbon nanotube electrodes. *Advanced Materials*, 13: 497-500, 2001.

[80] R. R. A. Syms, E. M. Yeatman, V. M. Bright V M, and G. M. Whitesides. Surface tension powered self-assembly of microstructures. The state-of-the-art. *Journal of Microelectromechanical Systems*, 12: 387-417, 2003.

[81] S. H. Lu, M. H. N. Tun, Z. J. Mei, G. H. Chia, X. Lim, and C.-H. Sow. Improved hydrophobicity of carbon nanotube arrays with micropatterning. *Langmuir*, 25: 12806-12811, 2009.

[82] K. K. S. Lau *et al.* Superhydrophobic carbon nanotube forests. *Nano Letters*, 3: 1701-1705, 2003.

[83] H. Liu, J. Zhai, and L. Jiang. Wetting and anti-wetting on aligned carbon nanotube films. *Soft Matter*, 2: 811-821, 2006.

[84] L. Li and C. M. Lukehart. Synthesis of hydrophobic and hydrophilic graphitic carbon nanofiber polymer brushes. *Chemistry of Materials*, 18: 94-99, 2006.

[85] Y.-T. Kim, Y. Ito, K. Fadai, T. Mitani, U.-S. Kim, H.-S. Kim, and B.-W. Cho. Drastic change of electric double layer capacitance by surface functionalization of carbon nanotubes. *Applied Physics Letters*, 87: 234106, 2005.

[86] B. Kakade, R. Mehta, A. Durge, S. Kulkami, and V. Pillai. Electric field induced, superhydrophobic to superhydrophlic switching in multiwalled carbon nanotube papers. *Nano Letters*, 8: 2693-2696, 2008.

[87] Y. Wang, Z. Shi, Y. Huang, Y. Ma, C. Wang, M. Chen, and Y. Chen. Supercapacitor devices based on graphene materials. *Journal of Physical Chemistry C*, 113: 13103-13107, 2009.

[88] C. Portet, P. L. Taberna, P. Simon, and C. Laberty-Robert. Modification of Al current collector surface by sol-gel deposit for carbon-carbon supercapacitor applications. *Electrochimica Acta*, 49: 905-912, 2004.

[89] M. D. Stoller, S. Park, Y. Zhu, J. An, and R. S. Ruoff. Graphene-based supercapacitors. Nano Letters, 8: 3498-3502, 2008.

[90] S. Daniel *et al.* A review of DNA functionalized/grafted carbon nanotubes and their characterization. *Sensors and Actuators B*, 122: 672-682, 2006.

[91] A. Kota *et al.* Electrical and rheological percolation in polystyrene/MWCNT nanocomposite. *Macromolecules*, 40: 7400-7406, 2007.

[92] S. Santhanagopalan, F. Teng, and D. D. Meng. IC-compatible deposition of vertically-aligned CNT forests for micro-supercapacitors. *International Workshop on Micro and Nanotechnology for Power Generation and Energy Conversion Applications (PowerMEMS)*, 593-596, 2009.

[93] D. N. Futaba *et al.* Shape-engineerable and highly densely packed single-walled carbon nanotubes and their application as super-capacitor electrodes. *Nature Materials*, 5: 987-984, 2006.

[94] M. Kaempgen, C. K. Chan, J. Ma, Y. Cui, and G. Gruner. Printable thin film supercapacitors using single-walled carbon nanotubes. *Nano Letters*, 9: 1872-1876, 2009.

[95] S. W. Lee, B. –S. Kim, S. Chen, Y. Shao-Horn, and P. T. Hammond. Layer-by-layer assembly of all carbon nanotube ultrathin films for electrochemical applications. *Journal of the American Chemical Society*, 131: 671-679, 2009.

[96] M. Fujiwara, E. Oku, M. Hamada, Y. Tanimoto, I. Mukouda, and Y. Shimomura. Magnetic orientation and magnetic properties of a single carbon nanotube. *Journal of Physical Chemistry A*, 105: 4383-4386, 2001.

[97] J. Shaver *et al.* Alignment dynamics of single-walled carbon nanotubes in pulsed ultrahigh magnetic fields. *ACS Nano*, 3: 131-138, 2009.

[98] S. Niyogi *et al.* Magnetically assembled multiwalled carbon nanotubes on ferromagnetic contacts. *Journal of Physical Chemistry B*, 108: 19818-19824, 2004.

[99] Z. Deng, E. Yenilmez, J. Leu, J. E. Hoffman, E. W. J. Straver, H. Dai, and K. A. Moler. Metal-coated carbon nanotube tips for magnetic force microscopy. *Applied Physics Letters*, 85: 6263-6265, 2004.

[100] A. Winkler *et al.* Magnetic force microscopy sensors using iron-filled carbon nanotubes. *Journal of Applied Physics*, 99: 104905, 2006.

[101] F. Geng and H. Cong. Fe-filled carbon nanotube array with high coercivity. *Physica B*, 382: 300-304, 2006.

[102] T. Fujita, Y. Hayashi, T. Tokunaga, and K. Yamamoto. Cobalt nanorods fully encapsulated in carbon nanotube and magnetization measurements by off-axis electron holography. *Applied Physics Letters*, 88: 243118, 2006.

[103] S. Brahim, S. Colbern, R. Gump, and L. Grigorian. Tailoring gas sensing properties of carbon nanotubes. *Journal of Applied Physics*, 104: 024502, 2008.

[104]   D. Cai *et al*. Highly efficient molecular delivery into mammalian cells using carbon nanotube spearing. *Nature Methods*, 2: 449-454, 2005.

[105]   J. Bao, Q. Zhou, J. Hong, and Z. Xu. Synthesis and magnetic behavior of an array of nickel-filled carbon nanotubes. *Applied Physics Letters*, 81: 4592-4594, 2002.

[106]   P. K. Tyagi *et al*. High-resolution transmission electron microscopy mapping of nickel and cobalt single-crystalline nanorods inside multiwalled carbon nanotubes and chirality calculations. *Applied Physics Letters*, 86: 253110, 2005.

[107]   J. Bao, C. Tie, Z. Xu, Z. Suo, Q. Zhou, and J. Hong. A facile method for creating an array of metal-filled carbon nanotubes. Advanced Materials, 14: 1483-1486, 2002.

[108]   N. Grobert *et al*. Enhanced magnetic coercivities in Fe nanowires. *Applied Physics Letters*, 75: 3363-3365, 1999.

[109]   Y. Fujiwara *et al*. Magnetic properties of carbon nanotubes grown on Fe catalyst layer by microwave plasma enhanced chemical vapor deposition. *Journal of Applied Physics*, 95: 7118-7120, 2004.

[110]   F. Wolny *et al*. Iron-filled carbon nanotubes as probes for magnetic force microscopy. *Journal of Applied Physics*, 104: 064908, 2008.

[111]   S. C. Tsang, Y. K. Chen, P. J. F. Harris, and M. L. H. Green. A simple chemical method of opening and filling carbon nanotubes. *Nature*, 372: 159-162, 1994.

[112]   Y. L. Hsin, K. C. Hwang, F.-R. Chen, and J.-J. Kai. Production and in-situ metal filling of carbon nanotubes in water. *Advanced Materials*, 13: 830-833, 2001.

[113]   S. Esconjauregui, C. M. Whelan, and K. Maex. The reasons why metals catalyze the nucleation and growth of carbon nanotubes and other carbon nanomorphologies. *Carbon*, 47: 659-669, 2009.

[114]   D. Takagi, Y. Homma, H. Hibino, S. Suzuki, and Y. Kobayashi. Single-walled carbon nanotube growth from highly activated metal nanoparticles. *Nano Letters*, 6: 2642-2645, 2006.

[115]   D. Takagi, H. Hibino, S. Suzuki, Y. Kobayashi, and Y. Homma. Carbon nanotube growth from semiconductor nanoparticles. *Nano Letters*, 7: 2272- 2275, 2007.

[116] D. Takagi, Y. Kobayashi, H. Hibino, S. Suzuki, and Y. Homma, Mechanism of gold-catalyzed carbon material growth. *Nano Letters*, 8: 832-835, 2008.

[117] A. J. Nichol, P. S. Stellman, W. J. Arora, and G. Barbastathis. Two-step magnetic self-alignment of folded membrane for 3D nanomanufacturing. *Microelectronic Engineering*, 84: 1168-1171, 2007.

[118] S. Timoshenko. *Strength of Materials*. Robert E. Krieger Publishing, Huntington, 1976.

[119] M. J. Donahue, D. G. Porter, OOMMF User's Guide, Version 1.0, in Interagency Report No. NISTIR 6376, National Institute of Standards and Technology, Gaithersburg, MD, 1999.

[120] Z. -P. Yang, L. Ci, J. A. Bur, S. -Y. Lin, and P. M. Ajayan. Experimental observation of an extremely dark material made by a low-density nanotube array. *Nano Letters*, 8: 446-451, 2008.

[121] P. Somasundaran. *Encyclopedia of Surface and Colloid Science, Volume 3*. CRC Press, Boca Raton, 2006.

[122] Y. Zhao, T. Tong, L. Delzeit, A. Kashani, M. Meyyappan, and A. Majumdar. Interfacial energy and strength of multiwalled-carbon-nanotube-based dry adhesive. *Journal of Vacuum Science and Technology B*, 24: 331-335, 2006.

[123] M. C. Strus, L. Zalamea, A. Raman, R. B. Pipes, C. V. Nguyen, and E. A. Stach. Peeling force spectroscopy: exposing the adhesive nanomechanics of one-dimensional nanostructures. *Nano Letters*, 8: 544-550, 2008.

[124] J. Gaillard, M. Skove, and A. M. Rao. Mechanical properties of chemical vapor deposition-grown multiwalled carbon nanotubes. *Applied Physics Letters*, 86: 233109, 2005.